

# Stochastic in Space and Time: Part 2, Effects of Simulating Orographic Gradients in Daily Runoff Variability on Bedrock River Incision

Adam Matthew Forte<sup>1</sup> and Matthew W. Rossi<sup>2</sup>

<sup>1</sup>Louisiana State University

<sup>2</sup>University of Colorado Boulder

March 13, 2024

## Hosted file

Table\_S2.xlsx available at <https://authorea.com/users/560667/articles/653387-stochastic-in-space-and-time-part-2-effects-of-simulating-orographic-gradients-in-daily-runoff-variability-on-bedrock-river-incision>

1

2 **Stochastic in Space and Time: Part 2, Effects of Simulating Orographic**  
3 **Gradients in Daily Runoff Variability on Bedrock River Incision**

4 **A.M. Forte<sup>1</sup> and M.W. Rossi<sup>2</sup>**

5 <sup>1</sup> Department of Geology and Geophysics, Louisiana State University, Baton Rouge, Louisiana,  
6 USA.

7 <sup>2</sup> Earth Lab, Cooperative Institute for Research in Environmental Sciences (CIRES), University  
8 of Colorado, Boulder, Colorado, USA.

9 Corresponding author: Adam M. Forte (aforte8@lsu.edu)

10 **Key Points:**

- 11 • Relationships among mean runoff and variability with topography in mountainous terrain  
12 can explain pseudo-thresholds in channel steepness
- 13 • Spatial asynchronicity of similar exceedance frequency runoff events is an unrecognized  
14 control on landscape evolution
- 15 • Orographic patterns in variability, snowmelt, and the characteristic size of runoff events  
16 alter predictions of climate-tectonic coupling

17 **Abstract**

18 The extent to which climate and tectonics can be coupled rests on the degree to which  
19 topography and erosion rates scales linearly. The stream power incision model (SPIM) is  
20 commonly used to interpret such relationships, but is limited in probing mechanisms. A  
21 promising modification to stream power models are stochastic-threshold incision models (STIM)  
22 which incorporate both variability in discharge and a threshold to erosion. In this family of  
23 models, the form of the topography erosion rate relationship is largely controlled by runoff  
24 variability. Applications of STIM typically assume temporally variable, but spatially uniform  
25 and synchronous runoff generating events, an assumption that is likely broken in regions with  
26 complicated orography. To address this limitation, we develop a new 1D STIM model, which we  
27 refer to as spatial-STIM. This modified version of STIM allows for stochasticity in both time and  
28 space and is driven by empirical relationships between topography and runoff statistics.  
29 Coupling between mean runoff and runoff variability via topography in spatial-STIM generates  
30 highly nonlinear relationships between steady-state topography and erosion rates. We find that  
31 whether the daily statistics of runoff are spatially linked or unlinked, which sets whether there is  
32 spatial synchronicity in the recurrence interval of runoff generating events, is a fundamental  
33 control on landscape evolution. Many empirical topography – erosion rate datasets are based on  
34 data that span across the endmember scenarios of linked versus unlinked behavior. It is thus  
35 questionable whether singular SPIM relationships fit to those data can be meaningfully related to  
36 their associated hydroclimatic conditions.

37

38 **Plain Language Summary**

39 Tectonic activity has long been known to modify climate by constructing mountain topography.  
40 Perhaps less obvious is the question of whether climatically driven erosion can also modify  
41 tectonic activity. This latter causal chain is premised on the notion that higher uplift rates can  
42 lead to steeper topography, higher precipitation rates, and thus more vigorous erosion. However,  
43 many erosion rate studies suggest that topography is only weakly sensitive to changes in rock  
44 uplift rates, thereby posing an important challenge to the climate-tectonic coupling hypothesis.  
45 Prior studies suggests that variability in daily runoff may be central to understanding this  
46 sensitivity, though historically have focused on how runoff is variable in time and not in space.  
47 As such, we developed a new numerical model of river erosion that simulates spatial patterns in  
48 runoff generation. We ran a suite of numerical experiments based on observed relationships  
49 among runoff, runoff variability, and topography to better understand how new model elements  
50 affect model sensitivity. We found that our crude representation of the size of runoff events is  
51 fundamental to model behavior. Given that event size is rarely considered in studies of climate-  
52 tectonic coupling, we argue that this property of runoff events requires more careful  
53 consideration.

## 54 **1 Introduction**

### 55 1.1. Motivation

56 The potential for two-way coupling between climate and tectonics is premised on how  
57 climate, erosion, and topography are related. Stream power provides an effective way to model  
58 the role of climate on erosion via a single parameter, the erodibility coefficient (Howard, 1994;  
59 Whipple & Tucker, 1999). When stream power is used as the principal erosion law, landscape  
60 evolution studies predict that climate should strongly influence the pattern and style of

61 deformation in mountain belts (Beaumont et al., 1992; Whipple & Meade, 2006; Willett, 1999).  
62 These numerical models show how prevailing wind direction, along with an orographic  
63 enhancement of precipitation, leads to across-strike asymmetry in the efficiency of erosion of the  
64 landscape. However, field verification of such dynamics has been elusive, with ambiguous  
65 evidence both for and against coupling between mean precipitation and tectonics (see discussion  
66 in Whipple, 2009). One barrier to field verification is uncertainty in how well suited stream  
67 power predictions are for isolating relationships among climate, erosion, and bedrock river  
68 morphology. Given the proliferation of carefully curated datasets attempting to constrain how  
69 climate is embedded in the erodibility coefficient (e.g., Adams et al., 2020; Ferrier et al., 2013;  
70 Forte et al., 2022; Leonard et al., 2023b), the time is ripe to re-visit assumptions implied by  
71 conventional applications of stream power to landscape evolution studies, especially in the  
72 context of the complexities that result from spatial gradients in orographic precipitation (e.g.,  
73 Anders et al., 2006, 2007; Bookhagen & Burbank, 2006; Bookhagen & Strecker, 2008; Roe,  
74 2005; Roe et al., 2003).

75         Since development of these early landscape evolution models, a large body of work has  
76 refined our understanding of the strengths and limitations of stream power (see summary in  
77 Lague, 2014). We highlight three sets of insights: (1) Probabilistic assessment of floods are  
78 needed when erosional thresholds matter (Lague et al., 2005; Snyder et al., 2003; Tucker, 2004);  
79 (2) Orographic gradients in mean precipitation lead to spatially non-uniform patterns in runoff  
80 generation (Bookhagen & Strecker, 2008; Roe et al., 2002, 2003); and (3) Precipitation phase  
81 (i.e., rain versus snow) mediates spatio-temporal patterns in runoff generation (Anders et al.,  
82 2008; Bookhagen & Burbank, 2010; Rossi et al., 2020). While there are a number of important  
83 limitations to using stream power (e.g., channel width scaling, tools-cover effects), we focus here

84 on those related to the characteristic discharge assumption typically used in stream power,  
85 specifically that the mean or bankfull discharge can be used to explain the long-term evolution or  
86 river morphology (e.g., see Wolman & Miller, 1960 for arguments based on alluvial rivers).  
87 Under this view, the characteristic discharge is generated from a characteristic runoff along  
88 hillslopes as it accumulates downstream. If runoff generation is uniform within a watershed, then  
89 the characteristic discharge is simply the product of the characteristic runoff and drainage area.  
90 In simple stream power, this set of assumptions entails that nonlinear relationships between  
91 channel steepness and long-term erosion rates will reflect differences in the incision process  
92 setting the slope exponent,  $n$  (Whipple and Tucker, 1999).

93         However, if erosional thresholds matter, nonlinearity is also linked to the temporal  
94 variability of streamflow (Tucker, 2004; Lague et al., 2005; Lague 2014). As such, there has  
95 been increasing interest in examining how such stochastic-threshold models (STIM) of river  
96 incision can be applied to empirical relationships between equilibrium channel steepness and  
97 long term erosion rates (Campforts et al., 2020; Desormeaux et al., 2022; DiBiase et al., 2010;  
98 Forte et al., 2022; Marder & Gallen, 2023; Scherler et al., 2017). Yet there has been less  
99 attention given to how orographic gradients in temporal dynamics may similarly alter predictions  
100 from simple stream power. Given the wide range of empirical estimates for  $n$  reported in the  
101 literature (Harel et al., 2016), we argue that river incision models likely require more hydrologic  
102 realism (e.g., Deal et al., 2018) to explain observed nonlinearities between channel steepness and  
103 erosion rate. In particular, we expand on STIM by: (1) allowing for orographic gradients in the  
104 magnitude-frequency relationships that describe runoff to evolve with growing topography, and  
105 (2) probing the influence of enforcing that magnitude-frequency relationships in runoff be

106 spatially synchronous, thereby altering the resultant probability distributions of streamflow. We  
107 refer to this new 1D model of river profile evolution as spatial-STIM.

## 108 1.2. Approach and Scope

109 The basis for our work is the stochastic-threshold incision model (STIM) proposed by  
110 Lague et al. (2005), which itself drew heavily from prior modeling efforts (Tucker & Bras, 2000;  
111 Tucker, 2004). We consider a modified version of STIM whereby daily discharge distributions  
112 are treated as Weibull distributions instead of exponential or inverse gamma distributions  
113 (following Forte et al., 2022). As originally conceived, this river incision model uses the shear  
114 stress formulation of stream power as the instantaneous incision law. The equilibrium steepness  
115 of a longitudinal profile for a given rate of base level fall is then derived by integrating the  
116 product of the instantaneous incision law and the probability distribution of flows, with a lower  
117 bound of integration set by the erosion threshold. The original form of the Lague et al. (2005)  
118 model was zero-dimensional such that the scaling relationship between discharge and drainage  
119 area was fixed. When applied to a 1D river profile or a 2D drainage basin, this formulation  
120 applies (1) to bedrock rivers at equilibrium and (2) where STIM parameters are spatially  
121 invariant within the watershed. While there are many hard-to-constrain parameters in STIM, this  
122 model improves on the stream power incision model (SPIM) by explicitly showing how two  
123 hydro-climatic parameters, the mean runoff and a shape parameter describing the distribution of  
124 streamflow events, alter the form of the relationship between long-term denudation rates and  
125 channel steepness (DiBiase & Whipple, 2011; Lague et al., 2005). While interpreting mean  
126 runoff is intuitive, the shape parameter is less so. In short, the shape parameter describes the  
127 variability of streamflow. While we describe this parameter more fully below, we highlight here  
128 that a key simplifying assumption in STIM is that runoff generating events are stochastic in time

129 but not in space. For small catchments with relatively uniform surface properties, this is a  
130 reasonable assumption. As the size of watersheds increases and as surface properties become  
131 more heterogeneous, the potential importance of partial source areas for runoff generation during  
132 events are expected to become more important (Dunne & Black, 1970). This is likely  
133 exacerbated in high-relief landscapes where orographic effects lead to significant spatial and  
134 temporal variation in precipitation events (e.g., Anders et al., 2006, 2007; Barros et al., 2000;  
135 Campbell & Steenburgh, 2014; Frei & Schär, 1998; Minder et al., 2008). It is not our intention to  
136 embed a full hydrological model of event-scale runoff generation into a 1D profile model of river  
137 incision. Instead, we seek to add flexibility to STIM such that we can explore how runoff  
138 statistics that vary in *both* space and time alter model predictions.

139         There are four key novelties to our new 1D model of bedrock river incision, which we  
140 refer to as spatial-STIM. First, the simulated longitudinal profile is subdivided into uniform bins  
141 of stream distance that allow us to evolve orographic gradients in runoff statistics as the river  
142 profile changes. Second, both mean runoff and daily runoff variability are dictated by their  
143 relationship to topography, specifically in response to local relief and elevation. Third, these  
144 topography-hydrology relationships are based on relationships observed in modern mountain  
145 ranges, which are described in our companion manuscript to this one (Forte & Rossi, 2024b),  
146 thus explicitly considering the role of snowmelt in modulating runoff variability. Fourth, the  
147 temporal stochasticity of each bin can either be linked or unlinked spatially. In other words, the  
148 recurrence probabilities of daily events within bins are either synchronous (linked) or  
149 asynchronous (unlinked) along the river profile. Asynchronous runoff generation will lead to  
150 much different streamflow distributions as upstream stochasticity modifies the downstream

151 accumulation of daily runoff. This last modification allows for examination into how the  
152 characteristic spatial scale of runoff events impacts model predictions.

153         We focus our analysis of model sensitivity to the new model elements introduced in  
154 spatial-STIM, the orographic rules used to set streamflow parameters, and changes in rock uplift  
155 rates. Our results are not intended to provide formal model calibration and validation using  
156 erosion rate data. Instead, our goal is to show how spatial-STIM might alter interpretations of the  
157 numerous channel steepness-erosion rate relationships reported in the literature and to develop  
158 heuristics for how such relationships might evolve as a mountain range grows (Figure 1). The  
159 conceptual framework builds on the findings from the companion manuscript to this one (Forte  
160 & Rossi, 2024b). That analysis revealed that both mean runoff and snowmelt fraction are  
161 functionally related to topography at the mountain range scale (Figure 1A). Increases in both are  
162 tied to a decreasing variability in daily runoff (Figure 1B), which itself is expected to cause  
163 increasingly nonlinear relationships between channel steepness and erosion rates (Figure 1C). As  
164 suggested by Forte et al., (2022), this set of expected relationships predicts an orographic  
165 feedback in which the continued topographic growth of a mountain range may be limited by the  
166 decreasing variability of streamflow and increasing nonlinearity in topography and channel  
167 steepness relationships (Figure 1). Consequently, we first ask what these dynamics entail for  
168 realistic gradients in mean runoff, runoff variability, and snowmelt. We then ask how the  
169 assumption of spatially synchronous runoff events (i.e., linked or unlinked per our definition  
170 above) may alter interpretations of river profile morphology. Questions are addressed by  
171 conducting a suite of numerical experiments using spatial-STIM.

172 **2. Background**

## 173 2.1. Channel Steepness and Erosion Rate Relationships

174 For river analysis, it is useful to define a channel steepness index ( $k_s$ ) that accounts for the  
 175 expected covariation of slope and drainage area within river systems (Flint, 1974):

$$176 \quad k_s = A^\theta S \quad (1)$$

177 where  $A$  is drainage area [ $L^2$ ],  $S$  is local river slope [ $L/L$ ], and  $\theta$  is a dimensionless constant that  
 178 describes the concavity of the river profile. In order to compare channel steepnesses for rivers  
 179 with different concavities, the steepness index  $k_s$  can be normalized by setting  $\theta$  to a reference  
 180 value,  $\theta_{ref}$ , thereby defining a normalized channel steepness index,  $k_{sn}$  (Wobus et al., 2006).

181 Normalized channel steepness can be determined via regression of the log-transformed, slope-  
 182 area data along river profiles (Kirby & Whipple, 2012). However, it is now more common to use  
 183 the so-called  $\chi$ -transform to calculate  $k_{sn}$  because of the noise inherent in slope-area data  
 184 (Whipple et al., 2022). As defined by Perron & Royden (2013),  $\chi$  is an integral transform of  
 185 distance such that:

$$186 \quad \chi = \int_{x_b}^x (A_0/A(x))^{\theta_{ref}} dx \quad (2)$$

187 where  $A_0$  is a reference drainage area,  $x$  is distance from the catchment outlet, and  $x_b$  is the  
 188 position of the outlet. On a plot of  $\chi$  and elevation, an equilibrium channel with a uniform  $k_{sn}$   
 189 appears as a straight line, assuming an appropriate  $\theta_{ref}$  is used in the calculation of  $\chi$ . When  $A_0$   
 190 is set to one, the slope of the  $\chi$ -elevation line equals  $k_{sn}$ .

191 Relationships between catchment-averaged normalized channel steepness and long-term  
 192 erosion rates,  $E$ , show that: (1)  $k_{sn}$  tends to be positively correlated with average erosion rate, but

193 that (2) the exact form of  $k_{sn}$ - $E$  relationships varies substantially among landscapes (see  
 194 compilations in Harel et al., 2016; Kirby & Whipple, 2012; Lague, 2014; Marder & Gallen,  
 195 2023). The general form of these relationships follow:

$$196 \quad k_{sn} = CE^\Phi \quad (3)$$

197 where  $C$  and  $\Phi$  are constants that vary between locations. To interpret these empirical  
 198 relationships, it is common to recast Equation 3 in terms of the parameters used in the stream  
 199 power incision model (SPIM, Howard, 1994; Whipple & Tucker, 1999). SPIM considers erosion  
 200 in terms of an erosional efficiency parameter ( $K$ ) that encapsulates aspects of both climate and  
 201 lithology, along with  $A$  and  $S$ :

$$202 \quad E = KA^mS^n \quad (4)$$

203 where  $m$  and  $n$  are constants thought to represent details of the hydrological and erosional  
 204 processes, respectively. In Equation 4, drainage area is a proxy for mean discharge  $\bar{Q}$  [ $L^3/t$ ] and  
 205 implicitly assumes a simple relationship between mean discharge, mean runoff  $\bar{R}$  [ $L/t$ ], and  
 206 drainage area such that  $\bar{Q} = \bar{R}A$  and where  $\bar{Q}$  and  $\bar{R}$  are the characteristic discharge and  
 207 characteristic runoff, respectively. The erosional efficiency parameter,  $K$ , embeds  $\bar{R}^m$  thereby  
 208 directly relating  $K$  to the hydro-climatology. By combining Equations 1, 3, and 4 in SPIM, it can  
 209 be readily shown that:

$$210 \quad \theta_{ref} = \frac{m}{n}, \quad (5)$$

$$211 \quad C = K^{-1/n}, \quad (6)$$

$$212 \quad \Phi = \frac{1}{n}, \quad (7)$$

213 and thus,

$$214 \quad k_{sn} = K^{-1/n} E^{1/n} \text{ or } E = K k_{sn}^n \quad (8)$$

215 Equation 8 predicts that the form of the  $k_{sn}$ - $E$  relationship can be cast in terms of variations in  
 216 climate and lithology (represented by  $K$ ) and erosional process (represented by  $n$ ). Implicit in this  
 217 relationship are the assumptions that the basin-averaged value of  $k_{sn}$  and  $E$  are steady state  
 218 values where the erosion rate approximately equals the long-term rock uplift rate and that the  $k_{sn}$   
 219 within the watershed in question is spatially uniform and free of transients (i.e., no prominent  
 220 knickpoints).

221 Recently, it has been shown that relationships between channel steepness and erosion  
 222 rates can be further interrogated by disentangling the climatic and lithologic components of the  
 223 erosional efficiency parameter,  $K$ , by defining an alternate form of  $k_{sn}$  that includes a proxy for  
 224 discharge. This new index,  $k_{snQ}$ , was defined by Adams et al., (2020):

$$225 \quad k_{snQ} = \bar{Q}^{\theta_{ref}} S. \quad (9)$$

226 Calculations of  $k_{snQ}$  typically use mean precipitation as a proxy for mean runoff to calculate  
 227 discharge, embedding the notion that mean runoff linearly scales with mean precipitation. Using  
 228 the same assumption in Equation 3 that  $\bar{Q} = \bar{R}A$ , it is then possible to recast  $K$  as:

$$229 \quad K = K_{lp} \bar{R}^m \quad (10)$$

230 where  $K_{lp}$  is the component of the erosional efficiency related to lithology and other factors such  
 231 as sediment flux dynamics and erosion thresholds. The relationship between  $k_{sn}$ - $E$  in Equation 8  
 232 can then be reformulated as:

$$233 \quad k_{snQ} = K_{lp}^{-1/n} E^{1/n} \text{ or } E = K_{lp} k_{snQ}^n \quad (11)$$

234 This alternative formulation of channel steepness acknowledges spatially varying precipitation  
235 and runoff and thus should help reduce the role of climate in the steepness – erosion rate  
236 relationship, allowing both more accurate use of topography to estimate erosion rates (Adams et  
237 al., 2020) and isolation of lithologic controls on erosion rate (Leonard et al., 2023b, 2023a).

238 Interpretation of either  $k_{sn}-E$  and  $k_{snQ}-E$  relationships within a SPIM framework relies on  
239 a similar set of simplifying assumptions that have been articulated in more detail elsewhere (e.g.,  
240 Harel et al., 2016; Kirby & Whipple, 2012; Lague, 2014). However, we highlight one important  
241 implication of SPIM to how the slope exponent in stream power,  $n$ , and the empirical exponent,  
242  $\Phi$ , are interpreted. Considering a steady state system where erosion rates balance uplift rates, the  
243 value of  $n$  controls the degree of nonlinearity,  $\Phi$  (Eq. 7). When  $n \approx 1$ , the linear relationship  
244 between topography and erosion rate implies that rivers maintain a uniform sensitivity to  
245 changes in rock uplift rate as they steepen. In contrast, when  $n \gg 1$ , and  $E$  is plotted on the  
246 abscissa, the strongly sublinear relationship (i.e., very small values of  $\Phi$ ) between topography  
247 and erosion rate implies that channel steepness reaches a pseudo-threshold as uplift rates  
248 continue to increase. Consequently, higher values of  $n$  lead to a reduced potential for two-way  
249 coupling between climate and tectonics as topography is no longer able to adjust to increases in  
250 rock uplift rates (Whipple & Meade, 2004). Global compilations of  $k_{sn}-E$  suggest that  $n \approx 2$   
251 (e.g., Harel et al., 2016; Lague, 2014), implying a sublinear response, but not one where  
252 significant pseudo-thresholds in  $k_{sn}$  limits the relief of mountain landscapes (Hilley et al., 2019).  
253 However, at the individual landscape scale, substantial differences in the values of  $n$  are  
254 observed, with some locations suggesting more linear relationships (e.g., Ferrier et al., 2013;  
255 Safran et al., 2005; Wobus et al., 2006) while others exhibit strongly sublinear relationships (e.g.,

256 Cyr et al., 2010; Forte et al., 2022; Hilley et al., 2019). Diagnosing the underlying mechanisms  
 257 for these large differences across landscapes is thus limited by relying on stream power alone.

## 258 2.2. Stochastic-Threshold Incision Model (STIM)

259 To probe controls on the nonlinear  $k_{sn}$ - $E$  relationships described above, it is useful to  
 260 consider an alternative fluvial incision model, specifically the stochastic-threshold incision  
 261 model (STIM). STIM shares some similarities with SPIM, but adds two important modifications:  
 262 (1) discharge magnitudes vary in time and (2) not all discharges are able to erode bedrock. While  
 263 different variants of stochastic-threshold incision models have been presented (e.g., Snyder et al.,  
 264 2003; Tucker, 2004), we focus on the version presented by Lague et al., (2005). The details of  
 265 this model have been discussed in depth previously (e.g., Campforts et al., 2020; DiBiase &  
 266 Whipple, 2011; Lague et al., 2005; Scherler et al., 2017), to which we refer interested readers.  
 267 Nevertheless, we briefly present the governing equations here, focusing on differences from the  
 268 original formulation of Lague et al., (2005).

269 STIM uses a stream power equation for instantaneous (e.g., daily) incision rates and then  
 270 integrates the incision law over a probability distribution of daily discharges to calculate an  
 271 average erosion rate. In the original formulation by Lague et al., (2005), both the instantaneous  
 272 incision and average erosion rates were cast in terms of dimensionless discharge. For our  
 273 application, it is more useful to define the instantaneous law in terms of a dimensional version of  
 274 daily discharge ( $Q$ ):

$$275 \quad I = K k_{sn}^n \bar{Q}^{m-\gamma} Q^\gamma - \Psi_c \quad (12)$$

276 where  $\gamma$  is an exponent describing local discharge and  $\Psi_c$  is the threshold parameter.  $K$ ,  $m$ , and  $n$   
 277 are similar to their counterparts in Equation 3, but have more formal definitions such that

$$278 \quad K = k_e k_t^a k_w^{-a\alpha} \quad (13)$$

$$279 \quad m = a\alpha(1 - \omega_a) \quad (14)$$

$$280 \quad n = a\beta \quad (15)$$

$$281 \quad \gamma = a\alpha(1 - \omega_s) \quad (16)$$

282 where  $k_e$  is a rock erodibility coefficient,  $k_t$ ,  $\alpha$ , and  $\beta$  are hydraulic and frictional constants,  $k_w$ ,  
 283  $\omega_a$ , and  $\omega_s$  are constants related to channel width scaling with discharge, and  $a$  is an constant  
 284 related to incisional process. The threshold parameter  $\Psi_c$  is related to both the rock erodibility  
 285 and incisional process such that

$$286 \quad \Psi_c = k_e \tau_c^a \quad (17)$$

287 where  $\tau_c$  is the critical shear stress for initiating incision. To calculate an average, steady state  
 288 erosion rate,  $E$ , Equation 12 must be integrated across a distribution of discharges

$$289 \quad E = \int_{Q_c(k_{sn})}^{Q_m} I(Q, k_{sn}) pdf(Q) dQ \quad (18)$$

290 where  $Q_c$  is the critical discharge above the incision threshold,  $Q_m$  is an arbitrarily high upper  
 291 bound on discharge assuming that the integral is convergent, and the  $pdf(Q)$  is the probability  
 292 distribution of daily discharge. In the original formulation of Lague et al., (2005), the inverse  
 293 gamma distribution of normalized discharge was used, thus fixing the scale parameter to 1. Here,  
 294 we follow recent work (Forte et al., 2022; Rossi et al., 2016) by using a two parameter Weibull  
 295 distribution to describe daily statistics. Because we allow runoff to vary as a function of profile  
 296 position which then accumulates downstream, our model simulates daily runoff distributions  
 297 instead of streamflow ones:

$$298 \quad pdf(R; R_0, c_R) = \frac{c_R}{R_0} \left(\frac{R}{R_0}\right)^{c_R-1} \exp^{-1(R/R_0)^{c_R}} \quad (19)$$

299 where  $R_0$  is a scale parameter, related to the mean of the distribution, and  $c_R$  is a shape parameter,  
300 describing the variability of daily runoff generation. Higher values of  $c_R$  imply lower variability.  
301 Because the original formulation was a zero-dimensional model, runoff variability and  
302 streamflow variability were equivalent, an important distinction that differs in our numerical  
303 model. The rationale for explicitly considering orographic gradients in runoff statistics is  
304 explained more fully in section 4.

305         Prior studies using STIM highlight that the degree of linearity between channel steepness  
306 and erosion rate is strongly mediated by the discharge variability (Lague et al., 2005; Tucker,  
307 2004; DiBiase & Whipple, 2011). Specifically, the value of  $\Phi$  (eq. 7) is a function of the shape  
308 parameter of the daily discharge distribution when erosion thresholds are large with respect to  
309 erosion rates (Regime III in Lague et al., 2005). As such, one explanation of the wide range of  
310 empirical values for  $n$  and  $\Phi$  might be due to regional differences in daily discharge variability  
311 (Marder & Gallen, 2023). Given that the shape parameters of inverse gamma and Weibull  
312 distributions are linearly related (Rossi et al., 2016), we are confident that the Weibull  
313 distribution can be reliably used in Equations 18-19. However, by using this alternative  
314 distribution, our modified version of STIM moderates the impact of heavy tailed distributions,  
315 allows discharge distributions to emerge from spatially variable runoff ones, and requires  
316 numerical simulation (i.e., there is no analytical solution).

### 317 **3 Orographic Relationships Between Hydroclimatology and Topography**

318         In our companion manuscript to this one (Forte & Rossi, 2024b), we used a 20-year  
319 global, daily time series of hydroclimate from the Water Global Assessment and Prognosis  
320 (WaterGAP3 - Alcamo et al., 2003; Döll et al., 2003) along with the HydroSheds v1, 15  
321 arcsecond digital elevation model (Lehner et al., 2008) and SRTM-90 data (Farr et al., 2007) to

322 develop empirical relationships between hydro-climatological and topographic variables. We  
 323 refer interested readers to Forte & Rossi (2024b) for more details, but summarize the primary  
 324 results of that analysis here (Figure 2). Specifically, Forte & Rossi (2024b) found a similar  
 325 inverse correlation between  $\bar{R}$  and variability (Figure 2A) as identified in smaller datasets from  
 326 gauged watersheds (e.g., Molnar et al., 2006; Rossi et al., 2016). The form of the relationship  
 327 between  $\bar{R}$  and variability is mediated by the relative contribution of snowmelt to total runoff  
 328 (Rossi et al., 2016). The snowmelt fraction,  $SF$ , is the total amount of runoff from snowmelt  
 329 divided by the total runoff. A distinct change in the functional form of this relationship occurs at  
 330 a  $SF$  of  $\sim 0.35$ . When  $SF$  is relatively low, the relationship between  $\bar{R}$  and  $c_R$  is more linear than  
 331 when  $SF$  is high (Figure 2A).

332 Because the shape ( $c_R$ ) and scale ( $R_0$ ) parameters shown in Figure 2 were determined by  
 333 fitting the right tail of runoff distributions above a 1% threshold, these fit parameters are no  
 334 longer related to the mean of the distribution in a simple way (Forte & Rossi, 2024b). The scale  
 335 parameter from the fits of daily data ( $R_0$ ) is linearly related to the scale estimated from the mean  
 336 runoff ( $R_0^*$ ) using the general equation for a Weibull distribution:

337

$$338 \quad R_0^* = \frac{\bar{R}}{\Gamma(1+1/c_R)} \quad (20)$$

339 But deviates substantially from the 1:1 line, especially in snowmelt influenced settings (Figure  
 340 2B). To account for this in our numerical model, we use the relationship between  $R_0$  and  $R_0^*$   
 341 (Figure 2B) to estimate the appropriate  $R_0$  from the calculated  $R_0^*$  based on the appropriate mean  
 342 runoff and  $c_R$  for a given bin.

343 Our main aim in the numerical modeling is to evolve stochastic runoff parameters as a  
344 mountain topography grows. In order to uniquely prescribe the distribution of flows (e.g.,  
345 Equation 19) within a part of a river profile, we need to know both  $\bar{R}$  and  $SF$  so that we can  
346 modify  $R_0^*$  and  $c_R$ . As described in Forte & Rossi (2024b), identifying singular, global  
347 relationships between either  $\bar{R}$  or  $SF$  and topographic metrics is challenging. As such, we use the  
348 three regional relationships between mean local relief and  $\bar{R}$  and maximum elevation and  $SF$  in  
349 the Greater Caucasus, European Alps, and northern British Columbia (Figure 2C-D). It is worth  
350 emphasizing that the lack of global relationships between either  $\bar{R}$  or  $SF$  and topography implies  
351 that rules for how runoff statistics coevolve with mountain growth needs regional constraints.  
352 However, the similar forms of these relationships is not surprising given prior work showing  
353 how local relief sets orographic precipitation (e.g., Bookhagen & Burbank, 2006; Bookhagen &  
354 Strecker, 2008). Furthermore, the increasing importance of snowmelt as mountain ranges grow is  
355 grounded in physical theory (i.e., typical temperature lapse rates imply decreasing temperatures  
356 with elevation and thus a potential for increasing snow fraction with elevation).

357 The two topographic metrics we focus on are local relief and local maximum elevation  
358 (e.g., within a WaterGAP3 pixel). While these topographic metrics are thought to be linked to  
359 river morphology at certain spatial scales (e.g., Ahnert, 1970), how to best use them to drive  
360 rules in a 1D river incision model is not obvious. Given our discretization of river profiles into  
361 bins, we argue there is a sensible way to honor the empirical relationships we show in Figure 2  
362 into a 1D river incision model. For example, it has been shown that local relief at the 2 to 2.5 km  
363 radius scale is linearly correlated with channel steepness (e.g., DiBiase et al., 2010). Channel  
364 steepness is a property of the river profile that can be readily calculated (Equation 1) and updated  
365 as the river profile evolves through time. How local relief is related to channel steepness for our

366 three selected regions is developed using the methods described in Forte et al., (2016), which  
367 itself uses a combination of TopoToolbox (Schwanghart & Scherler, 2014) and the Topographic  
368 Analysis Kit (Forte & Whipple, 2019). First, we extract all watersheds with a drainage area  $>50$   
369  $\text{km}^2$  and an outlet elevation above 300 m. Any watershed from this initial extraction with a  
370 drainage area  $>250 \text{ km}^2$  was then subdivided into tributary watersheds that connect to the trunk  
371 channel using drainage areas  $>50 \text{ km}^2$  as a threshold. For each catchment, mean channel  
372 steepness and local relief (2500 m radius) was calculated along with the  $R^2$  value for a linear fit  
373 between  $\chi$  (Equation 2) and elevation. Values of  $R^2$  close to 1 imply that a river profile is largely  
374 free of major knickpoints. The  $R^2$  values were thus used to screen for reaches in quasi-  
375 equilibrium such that only reaches above a high threshold ( $>0.90$ ; Figure S1) were used to  
376 develop regionally based relationships between channel steepness and local relief. By  
377 establishing the channel steepness to local relief relationship for each site, we can then apply  
378 these rulesets based on local relief into our river incision model. It is worth noting that, in this  
379 transformation, we used a relationship between  $k_{sn}$  and 2.5-km relief (as described above) using  
380 SRTM-90 data. In contrast, the relationship between mean runoff and 2.5-km relief used the  
381 HydroSheds 15-second data (Figure 2C). For our regions of interest, the distributions of these  
382 two local relief datasets do not suggest meaningful differences (Figure S1). As channel steepness  
383 evolves in the numerical model, it is directly tied to local relief and indirectly tied to maximum  
384 elevation, the latter of which is calculated by adding the local relief to the minimum elevation of  
385 the profile for a given bin. The choice of using the lowest maximum elevation is a conservative  
386 one because it produces the smallest possible snowmelt fraction for a given value of local relief.

## 387 **4 River Incision Model**

388           There are now many studies testing the utility of the Stochastic-Threshold Incision  
389 Models (STIM) (e.g., Campforts et al., 2020; Desormeaux et al., 2022; DiBiase & Whipple,  
390 2011; Forte et al., 2022; Marder & Gallen, 2023; Scherler et al., 2017). However, we believe this  
391 paper is the first attempt to modify a longitudinal profile version of STIM to allow for stochastic  
392 events in space as well as time, which we refer to as spatial-STIM. Our modelling strategy shares  
393 some similarity with recent 2D efforts that consider the role of spatial variability in precipitation  
394 events (e.g., Coulthard & Skinner, 2016; Peleg et al., 2021), but these efforts considered  
395 landscape evolution at timescales orders of magnitude shorter than we do here. By subdividing  
396 the long profile into bins we coevolve the hydrology with the local channel morphology. Using a  
397 binned approach requires a decision for whether spatial bins should depend on each other (i.e.,  
398 the recurrence interval of runoff events on a given day are synchronous across the profile) or  
399 whether they should be treated independently (e.g., bins experience storm or snowmelt events of  
400 different recurrence intervals at a given time). We refer to the former as linked cases and the  
401 latter as unlinked ones, referring to whether the recurrence intervals between bins are linked to  
402 each other or unlinked. In both linked and unlinked cases, the profiles experience orographic  
403 gradients in mean daily runoff and daily runoff variability. We further describe the nuances of  
404 linked versus unlinked cases in section 4.2.

### 405           4.1. Spatial-STIM

406           Our new 1D river profile bedrock incision model was developed in Python 3.10 by  
407 implementing an explicit upwind finite difference solution of Equation (12) for daily incision  
408 along the profile. The model itself is available from Forte (2024). The starting condition for each

409 model run uses a drainage area distribution based on the relationship between profile length ( $L$ )  
 410 [ $L$ ] and drainage area ( $A$ ) [ $L^2$ ] from Sassolas-Serrayet (2018):

$$411 \quad L = cG_c A^{n_A} \quad (21)$$

$$412 \quad c = 0.5G_c\sqrt{\pi} + 0.25\sqrt{G_c^2\pi - 4} \quad (22)$$

413 where  $G_c$ , or the Gravelius coefficient, is set to 1.5 and the exponent  $n_A$  is set to 0.54. This form  
 414 of the relationship between drainage area and stream distance is useful because it allows for  
 415 direct consideration of the shape of the drainage basin using a single parameter. A watershed  
 416 with a  $G_c$  of 1 has a perfectly circular boundary and a watershed with a  $G_c$  of 2 is an narrow,  
 417 elongated watershed. Because we are only simulating the river profile, we use a threshold  
 418 drainage area,  $A_c$ , of 1 km<sup>2</sup>. Using the specified  $G_c$  and  $n_A$  from above, this is equivalent to the  
 419 Hack (1957) relationship:

$$420 \quad A = k_a L^h + A_c \quad (23)$$

421 where  $k_a = 0.969$  and  $h = 1.851$ . For all runs, we set the spacing between nodes at 100 meters and  
 422 the time step to one day, with saved outputs every 5000 years. All runs are initialized using a  
 423 profile with a low and constant  $k_{sn}$  of 25 m.

424 Spatial variations in both mean runoff and runoff variability are handled by adopting  
 425 uniform river length bins along the longitudinal profile. This implies that the proportion of total  
 426 drainage area represented by each bin varies along the profile. We test the sensitivity of the  
 427 model to this style of discretization in section 5.4. Each bin has a single scale and shape  
 428 parameter describing the runoff distribution that is used for all the nodes within the bin. At each  
 429 time step, these parameters are recalculated based on the current topography. Figure 3 shows an  
 430 example of how the mean runoff and shape parameter vary as a function of bin location at one

431 time step during a transient. The location and dimensions of bins are fixed for each model run to  
432 maintain computational efficiency. However, our analysis of model sensitivity includes varying  
433 the bin size and number of bins within a profile to test the sensitivity of results to these choices  
434 (see section 5.4). The key property of our model that allows hydro-climatology to coevolve with  
435 the topography occurs in the method we use to the recalculate the shape and scale parameters at  
436 every time step.

437         As described in section 3, we used both global (Figure 2A-B) and regional relationships  
438 (Figure 2C-D) to define the mean runoff, scale parameter, and shape parameter within each bin.  
439 For a given time step and bin, the chain of action is: (1) Use the channel steepness from the  
440 previous step to calculate local relief using the linear relationships developed from the SRTM-90  
441 elevation data (e.g., Figure S1); (2) Use the local relief to calculate mean runoff using the power  
442 law relationships developed from the regional WaterGAP3 analysis (Figure 2C); (3) Also use the  
443 local relief to determine the maximum elevation by adding it to the minimum elevation within  
444 the bin; (4) Use the maximum elevation to calculate the snowmelt fraction using the power law  
445 relationships developed from the regional WaterGAP3 analysis (Figure 2D); and finally (5) Use  
446 the snowmelt fraction to choose an appropriate mean runoff and shape parameter (Figure 2A)  
447 and do the scale parameter adjustment (Figure 2B) based on the global WaterGAP3 analysis. In  
448 this way, the mean runoff, scale, and shape parameters are updated from channel topography  
449 alone and follow data driven rules.

450         To ensure that the model does not extrapolate into an unreasonable part of parameter  
451 space, we impose a maximum relief that any bin can achieve. We set this to 2500 m for most  
452 runs based on a conservative estimate of what is observed in modern landscapes (e.g., Figure  
453 S1), though we also test the sensitivity of model results to this choice in Section 5.4. The

454 imposition of a maximum relief is broadly motivated by limits to local relief set by hillslope  
455 strength (e.g., Montgomery & Brandon, 2002; Schmidt & Montgomery, 1995). Embedded in the  
456 assumption of a maximum local relief is the expectation that this should be controlled by  
457 processes not considered in our model (e.g., hillslope creep or mass wasting). While we do not  
458 impose a limit on maximum elevation, it has an implicit limit set by the local relief maximum.  
459 We also make sure that the snowmelt fraction cannot exceed 1. After meeting all these  
460 constraints, each bin has a scale and shape parameter describing the probability distribution of  
461 runoffs expected for each bin at a given time step (e.g., Figure 3). To simulate the stochasticity  
462 implied by these derived parameters, we use the *SciPy weibull\_min* and appropriate sub-  
463 functions to randomly extract a runoff magnitude from the relevant probability distribution for  
464 that bin. In detail, for every 100 years of model run time, the model generates a 100 year daily  
465 time series (i.e., 36,500 days) of runoffs within each bin. This is done for efficiency because the  
466 random selection of numbers from a distribution is one of the more computationally time  
467 intensive steps. The compute time required to generate one random number is comparable to  
468 generating a large quantity of random numbers from a given distribution. The impact of this  
469 decision means that mean runoff and variability are only updated every 100 years. However,  
470 even for the maximum 8 mm/yr rock uplift rate we impose, the amount of profile change - and  
471 thus change in either relief or maximum elevation - in 100 years is sufficiently small as to not  
472 significantly influence results. At each 100-year increment where the runoff time series is  
473 generated, the current iteration number is used as the starting seed for the generation of  
474 subsequent random numbers. This ensures that the random numbers (i.e., runoff magnitudes)  
475 change through the model run.

476 For each day, runoff within each bin is first routed along the profile before calculating  
477 fluvial incision. Specifically, on a given day and within each bin along the stream profile, a  
478 random magnitude of runoff is drawn from the runoff distribution for that bin. Any stream nodes  
479 within that bin are assigned that runoff magnitude. This is done for all bins. Then, at each node,  
480 the daily runoff [L/T] is converted into a volume by multiplying by the drainage area (A)  
481 contributed by that node (i.e.,  $dA/dx$ ). The volumes within each node are cumulatively summed  
482 downstream to convert to daily discharge ( $Q$ ) for use in the finite difference solution of equation  
483 12. An identical procedure is performed using the mean runoff in each bin (base on the relevant  
484 regional relationship between mean runoff and mean local relief) to generate a mean discharge  
485 ( $\bar{Q}$ ) for use within equation 12.

#### 486 4.2. Linked versus Unlinked Cases

487 Whether neighboring bins are correlated or independent in time depends on how runoff  
488 events are generated in the landscape. The spatially correlated case mimics scenarios where  
489 storm or snowmelt runoff events vary in magnitude along the profile but represent the same  
490 recurrence interval (linked). The spatially independent case mimics scenarios where storm or  
491 snowmelt runoff events also vary in magnitude along the profile but where the runoff magnitudes  
492 are randomly drawn from the probability distributions for each bin independent of each other  
493 (unlinked). It is critical to clarify that both the linked and unlinked cases produce along-profile  
494 gradients in runoff magnitudes that coevolve with growing topography (e.g., see example  
495 probability distributions in Figure 3F). Linking the probability of events within bins along the  
496 profile enforces that runoff is spatially autocorrelated and is analogous to asserting a nonlinear  
497 scaling between streamflow and drainage area in prior treatments of STIM. In contrast, the  
498 unlinked case allows for crude assessment of the relative scales between runoff source areas and

499 the size of basin. By specifically considering the two endmember scenarios where exceedance  
500 probabilities are either uniform (linked) or independent (unlinked) across the basin, we are able  
501 to evaluate the potential importance of spatial autocorrelation in daily runoff on the efficiency of  
502 erosion. We consider how to physically interpret linked and unlinked cases in section 6.2.2, but it  
503 is important to emphasize that with respect to the model setup, we are largely agnostic as to  
504 possible physical or hydroclimatological processes these two endmembers represent. This  
505 agnosticism includes the somewhat generic terminology we adopt for these two scenarios, i.e.  
506 linked vs unlinked, to avoid association of them with any specific process as we expect that there  
507 are non-unique sets of process interactions that can lead to these behaviors. Finally, we  
508 emphasize that these two behaviors are extreme endmembers, and we would fully expect most  
509 real landscapes to behave as a mixture of these two endmembers.

510         Implementation of the unlinked versus linked scenarios is set by changing the  
511 pseudorandom seed number. For a given seed number, the pseudorandom number generator will  
512 produce a reproducible sequence of numbers. In the linked scenarios, the seed for the 100-year  
513 time series is set by the iteration number for all bins. In the unlinked case, the seed number for  
514 bins are incremented by 1, such that for bin 1, the seed is  $i$ , for bin 2, the seed is  $i+1$ , and so on.  
515 For the linked cases, this forces the exceedance frequency of events in all bins to be identical at a  
516 given timestep (e.g., Figure 3F). For the unlinked cases, this allows the exceedance frequency of  
517 events in bins to vary at a given timestep (e.g., Figure 3E). In the unlinked case, the size of the  
518 bins crudely represents an assumed characteristic size of runoff events. Real landscapes likely  
519 experience a mixture of small footprint, convective rain events, large footprint, synoptic-scale  
520 rain events, temperature-induced snowmelt events, and rain-on-snow events. For example, in our  
521 companion manuscript (Forte & Rossi, 2024b), we showed how the largest area runoff events

522 above a given magnitude tend to be increasingly produced by snowmelt. We anticipate that  
523 mixtures of event sizes, like those suggested by the WaterGAP3 data, will produce intermediate  
524 behaviors and response times, which is why we consider both the linked and unlinked  
525 endmember scenarios for all parameter sets. The question of whether landscapes are better  
526 represented by unlinked versus linked scenarios is revisited in the discussion.

#### 527 4.3 Model parameterization

528 Our main objectives in this study are to extend the zero-dimensional stochastic-threshold  
529 incision model (STIM) of Lague et al. (2005) to a 1D profile model that includes spatially  
530 varying daily runoff variability (spatial-STIM). The purpose of this new model is to see how  
531 coupling orographic patterns in runoff variability can alter predictions in the steady state and  
532 transient evolution of river longitudinal profiles using stream power. It is beyond the scope of  
533 this effort to do a full sensitivity analysis on all the STIM parameters, which have already been  
534 explored in great depth (DiBiase & Whipple, 2011; Lague, 2014; Lague et al., 2005). Instead, we  
535 focus on driving our new model using empirical relationships for how mean runoff and daily  
536 runoff variability vary as a function of local relief and testing the sensitivity of our results to the  
537 differences in model structure we have added to spatial-STIM. As such, most STIM parameters  
538 (like thresholds, rock erodibilities, width scaling) are fixed in all model runs, typically to values  
539 that were used in our prior work in the Greater Caucasus (Forte et al., 2022). The values of fixed  
540 parameters are reported in Table S1. Table S2 summarizes the parameters we vary in our  
541 numerical experiments and contains a complete list of model runs. The suite of numerical  
542 experiments we conduct address two central questions: (1) What do orographic relationships  
543 between mean runoff and daily runoff variability entail for STIM-based predictions of the  
544 relationship between channel steepness and rock uplift rates, and (2) How sensitive are spatial-

545 STIM results to the new elements of model structure (i.e., by varying stochastic parameters along  
546 bins in the longitudinal profile)?

## 547 **5 Results**

548 We report results in three parts. The first part provides results for a series of baseline  
549 cases that use a similar model structure (50-km long rivers, 2-km wide bins), albeit for both the  
550 linked and unlinked scenarios. These baseline cases represent how a  $\sim 488 \text{ km}^2$  area watershed  
551 responds to range of uplift rates (0.25 to 8 mm/yr) under modern hydro-climatic conditions of the  
552 mountainous regions of the Greater Caucasus, European Alps, and British Columbia. The second  
553 part uses the results from the Greater Caucasus runs to interrogate the large differences in  
554 transient and steady state behavior that are observed between linked and unlinked cases.  
555 Specifically, we examine when and where erosional thresholds are exceeded. The third part tests  
556 the sensitivity of our findings to other differences in model structure, specifically to profile  
557 length, bin size, bin number, maximum local relief, and binning criteria. To do this, we use the  
558 linked Greater Caucasus baseline case at rock uplift rates of 1 mm/yr as the starting point for the  
559 majority of sensitivity analyses. Sensitivity experiments vary: (1) stream length and number of  
560 bins using model setups of 10, 20, 30, 40, 50 and 100 km width bins fixed at 2 km wide, (2)  
561 maximum relief within a bin using model setups of 1500, 2000 and 2500 m, and (3) bin size  
562 using model setups of 2, 5, and 10 km wide bins. Because profile length and bin size together  
563 define the number of bins, we also run a sensitivity experiment designed to: (4) test the notion  
564 that number of bins, and thereby the granularity of how we represent the hydroclimate, is  
565 controlling the steady state channel steepness. This latter test compares two profile lengths of 10  
566 and 50 km long using both 5 and 10 bins. Finally, we test the sensitivity of the model results to

567 the binning scheme by: (5) running a full suite of models where we divide the profile into bins of  
568 equal drainage area as opposed to equal stream distance.

569 The dynamics of individual runs are decidedly complex despite them being 1D models.  
570 In the sections below, much of the behavior of individual model runs is not discussed in detail  
571 because we focus on general behavior. Outputs of all models are available in Forte & Rossi  
572 (2024a), along with summary plots of all model runs. Codes to interpret and interrogate the  
573 model results are available in Forte (2024).

#### 574 5.1 Model behavior across regional cases

575 Comparison of the regional cases provides important insights into the behavior of spatial-  
576 STIM. Figure 4 shows the steady state results for three cases inspired by the modern hydro-  
577 climate of the Greater Caucasus, Alps, and British Columbia. Model results are shown for both  
578 linked and unlinked runoff parameters, a bin size of 2 km, a river length of 50 km, and uplift  
579 rates spanning from 0.25 to 8 mm/yr. Note that we refer to these results as reflecting ‘steady  
580 state’, even though the majority of the model runs never truly reach steady state in the sense of  
581 invariant properties along the river profile. In detail, several behaviors can be gleaned from these  
582 comparisons. First, for all unlinked scenarios, there is a distinct upstream decrease in channel  
583 steepness. In contrast, channel steepness occupies a much smaller range of values for linked  
584 scenarios (Figure 4B). As a spatial gradient in  $k_{sn}$  effectively suggests a different true concavity  
585 than the imposed reference concavity, this result implies that, especially for the unlinked  
586 scenarios, the concavity of river profiles can substantially deviate from the 0.5 reference value  
587 used to calculate  $k_{sn}$ , a point we return to in the discussion. Second, upstream decreases in  
588 channel steepness (and thus local relief) are associated with decreases in mean runoff in those  
589 high elevation bins (Figure 4D) as should be expected from the imposed empirical relationships

590 (e.g., Figure 2). Daily runoff variability also decreases upstream in line with increases in  
591 snowmelt fraction, though most of the longitudinal profiles generally remain below the  
592 snowmelt-dominated regime (Figure 4C). Third, Figure 4 reveals important differences between  
593 regional cases as a function of uplift rate. For example, despite the highest uplift rate being 32X  
594 the lowest uplift rate, the steady state river profiles for the unlinked British Columbia region are  
595 remarkably similar across the full range of rock uplift rates (Figure 4A), likely related to the  
596 higher snowmelt fraction (Figure 4C), mean runoff (4D), and lower variability (4E) of these  
597 model runs.

598         One main hypothesis of this study (Figure 1B) envisioned periods of time or locations in  
599 which the snowmelt-dominated regime (i.e., high mean runoff and low runoff variability) can  
600 substantially modify the sensitivity of channel steepness to increases in rock uplift rates. While  
601 motivated by three landscapes (and hydro-climatic rulesets) that might sample across this  
602 transition, only British Columbia achieves enough total relief to even begin to sample this part of  
603 parameter space (Figure 4C). For the other two rulesets, model runs rarely exceed the snowmelt  
604 fraction of 0.35 (Figure 4C), consistent with the empirical data from WaterGAP3 (Figure 2D).  
605 As a test of internal consistency, we also checked the mean runoffs and shape parameters for  
606 each bin across the full range of uplifts at all timesteps for the Greater Caucasus unlinked model  
607 run. The majority of bins stay within empirical ranges without any formal restriction to this  
608 range (Figure S2). This suggests that our new model is not extrapolating to unrealistic portions of  
609 parameter space during the transient evolution of these river longitudinal profiles.

610         When generalizing across all model runs in Figure 4, two main results emerge: (1)  
611 Differences in the steady state form of river profiles induced by different hydro-climatic forcings  
612 are relatively modest for a given rock uplift rate (Figure 4A); (2) Whether the recurrence interval

613 of runoff events in spatial bins are linked or unlinked is more significant, especially when rock  
614 uplift rates are low (Figure 4A-B). Examining the mean values of metrics (far right column in  
615 Figure 4) highlights that differences among regional rulesets for a given set of model parameters  
616 (i.e., linked versus unlinked, rock uplift rate) generally span a smaller range within a given  
617 region than the larger contrast between linked and unlinked scenarios. Because of this, we focus  
618 our initial analysis of transient model dynamics on the assumption of linked versus unlinked  
619 runoff events.

## 620 5.2 Explaining differences between unlinked versus linked scenarios

621 We use the contrast between the Greater Caucasus unlinked recurrence interval of runoff  
622 events scenario with a 1 mm/yr uplift rate (GC1U) and its linked equivalent (GC1L) to help  
623 unpack model dynamics. As the longitudinal profile evolves towards steady state, a transient  
624 slope-break knickpoint migrates upstream (e.g., Figure 3), much like in other stream-power  
625 based models of river incision (e.g., Crosby & Whipple, 2006; Rosenbloom & Anderson, 1994).  
626 However, the key novelty to our model is that runoff statistics vary both in space and in time. For  
627 both the unlinked and linked scenarios, we identified a time when the knickpoint had obtained a  
628 similar relative upstream position (Figure 3A-B; 1 Ma for unlinked; 0.63 Ma for linked). Figures  
629 3C-F show the runoff parameters for every bin in the profile at that time. On these plots, we  
630 show the spatially averaged values for the shape parameter and mean runoff. We also show the  
631 median values of those parameters for a Monte Carlo simulation (500 trials) of randomly  
632 sampled, 100-year long discharge records using the orographic rules for this timestep. Both the  
633 unlinked and linked scenarios show that mean runoff is similar whether averaging across bins or  
634 routing runoff down the profile (i.e., the Monte Carlo estimates). In contrast, a persistent feature  
635 of unlinked scenarios is that the variability of routed discharge is significantly lower (i.e., larger

636 shape parameter) than the corresponding averages of bins would suggest (Figure 3C & 3E), a  
637 behavior not observed in the linked scenarios (Figure 3D & 3F).

638 To expand beyond one moment in time, Figure 5 shows the contrast in model runs as a  
639 function of  $\chi$  and stream distance for the Greater Caucasus hydro-climatic ruleset (e.g., Figure  
640 2C & D). The temporal evolution of  $\chi$ -elevation plots (Figure 5A-B) and longitudinal profiles  
641 (Figure 5C-D) reiterate that unlinking the runoff statistics as a function of profile position  
642 reduces the efficiency of erosion (i.e., generates steeper steady profiles). However, while the  
643 overall erosional efficiency is lower, the unlinked hydroclimatic parameters actually produce  
644 more significant (and temporally isolated) pulses in erosion during the transient evolution of the  
645 profile (contrast stripes in Figure 5E with 5F) and greater mean runoffs (more blue in Figure 5G  
646 than 5H). Unlinked cases also generally take longer to reach a quasi-steady state (Figure 5). Here  
647 specifically we consider these profiles to be in a quasi-steady state in the sense that the elevations  
648 (and associated parameters, e.g., relief, etc.) never reach a truly static value, but effectively  
649 oscillate around an average value. We briefly offer our explanation for this apparent disconnect  
650 between long-term model behavior and what would be observed during a single snapshot of  
651 erosion along the river profile.

652 Interpreting the dynamics in spatial-STIM requires understanding the frequency of  
653 exceedance of erosional thresholds in the model (Figure 6). In our numerical experiments this  
654 threshold is held constant for all model runs. For both the linked and unlinked scenarios, areas  
655 above knickpoints rarely exceed the threshold for erosion and are thus passively uplifted until a  
656 knickpoint passes. The knickpoint itself focuses threshold exceedances to an area just below  
657 where channels are steepest (red areas along profile in Figure 6A-B). This hotspot in threshold  
658 exceedance is localized near the knickpoint for the linked case and persists in downstream

659 reaches for the unlinked case. Because the knickpoint is migrating upstream, cumulative  
660 threshold exceedances as a function of stream position are relatively smooth when averaged over  
661 the long-term (Figure 6C-D) with an average that stabilizes to a single value (Figure 6E-F).  
662 Threshold exceedance frequencies are generally higher in the unlinked case (Figure 6E-H). In  
663 addition, local erosion rates can get much higher in the unlinked case (e.g., Figure 5E-F, 6G-H).  
664 Taken alone, these observations might suggest a more efficient hydroclimate in the unlinked  
665 case. However, both river profiles are approaching a quasi-steady state suggesting that river  
666 profiles needed to adjust to more frequent temporal exceedances to overcome the spatial  
667 heterogeneity in runoff generation. Specifically, the unlinked case inhibits the “benefit” of water  
668 flowing from upstream. Higher probabilities of exceedance are needed in upstream reaches to  
669 balance rock uplift, which are accommodated by steepening, because rare runoff events are not  
670 synchronous along the river profile. These dynamics result in a negative upstream trend in  
671 cumulative exceedance (Figure 6C) that is not observed in the linked case (Figure 6D). The  
672 linked scenarios are thus able to maintain lower relief at lower mean discharges because of the  
673 spatial autocorrelation of events in a river basin. The assumption for how runoff events  
674 accumulate downstream appears to be an under-appreciated governor of model dynamics, that is  
675 perhaps more important than the orographic rules for hydro-climate we use.

676       Finally, an additional difference between unlinked and linked cases is the perpetuation of  
677 some amount of dynamic instability in the unlinked models. This can be seen in comparisons of  
678 temporal and spatial variations in erosion rate (contrast Figure 5E with 5F) and the frequency of  
679 exceedance of erosion thresholds (contrast Figure 6A with 6B) between the unlinked and linked  
680 models. Even after the main transient knickpoint has propagated completely through the  
681 landscape, there are quasi-periodic erosional “events” that continue to impact the unlinked

682 models, which lead to small-scale variations in profile topography. To understand this behavior,  
683 it is worth considering the dynamics at play after the profile reaches its quasi-steady form. In  
684 both cases, not every daily event will erode. In the linked cases, whether a given event will erode  
685 (i.e., whether it exceeds the erosion threshold) will tend to be spatially uniform as the whole  
686 profile has nearly adjusted to the same threshold condition. In contrast, for unlinked cases, events  
687 that exceed the erosion threshold will occur only in a portion of the profile (i.e., the bin where  
688 the event occurs and possibly in bins downstream). This effectively generates small knickpoints  
689 in the profile that subsequently propagate upstream. The local change in steepness will similarly  
690 modify the critical discharge necessary to exceed the erosion threshold, further accentuating this  
691 new perturbation. Because there is no damping mechanism for these small perturbations in the  
692 unlinked scenarios, the river profile is inherently less stable.

### 693 5.3 Sensitivity of spatial-STIM to other elements of model structure

694 While the most significant difference between model outcomes is tied to whether the  
695 runoff distributions are linked or unlinked along the river profile, other structural elements of the  
696 model are also important to model dynamics. Specifically, we interrogate how the three new  
697 model parameters added to spatial-STIM (bin size, maximum local relief, profile length) and one  
698 derived parameter (number of bins) influence model behavior (Figure 7). This latter parameter  
699 encodes the ratio between the size of the system (profile length) and the scale over which  
700 changes in hydro-climatic parameters are represented (bin size). We also test the importance of  
701 how the profile is binned, namely when uniformly subdivided by river length versus contributing  
702 drainage area.

703 For all sensitivity experiments, we use the Greater Caucasus hydroclimatic parameters  
704 and generally use rock uplift rates of 1 mm/yr, except for experiments testing the way the profile

705 was discretized (Figure 7E). In all cases, the steady-state channel steepness is what is being  
706 compared. Reference conditions (black squares and circles) assume 50-km river lengths, bin  
707 sizes of 2 km, and a maximum imposed relief of 2.5 km. For unlinked scenarios, the sensitivity  
708 of  $k_{sn}$  to bin size is substantial (Figure 7A, S3). A 5X increase in bin size corresponds to ~33%  
709 reduction in  $k_{sn}$ . Increasing the size of bins both decreases the granularity with which orographic  
710 gradients in hydro-climatic parameters are represented as well as increases the degree of spatial  
711 autocorrelation. To the latter point, we also plot the linked case to show that the effect of  
712 increasing bin size is approaching the  $k_{sn}$  values observed when the events are linked over the  
713 entire river profile. For the majority of model runs, we consider bins of equal river distance.  
714 Because of the power-law scaling between distance and drainage area, this implies that the  
715 contributing area of each bin is not the same. As such, we test a set of both linked and unlinked  
716 model runs that use bins of equal drainage area (Figure 7E). When the number of bins are the  
717 same, the results for linked models are identical to the distance bin models. For unlinked cases,  
718 the area and distance bin results are different, but overlap within uncertainty. The sensitivity of  
719  $k_{sn}$  to maximum local relief is near zero (Figure 7B, S3). It is worth noting that this threshold in  
720 maximum local relief was set to prevent extrapolating our runoff parameter relationships to  
721 unrealistic values. The insensitivity of channel steepness to this maximum local relief gives us  
722 confidence our model interpretations are not unduly sensitive to this threshold parameter. We  
723 suspect that if the maximum relief was set unrealistically low or high values, it would begin to  
724 influence model results. For unlinked scenarios, the sensitivity of  $k_{sn}$  to profile length, and thus  
725 system scale, is substantial (Figure 7C, S3). A 10X increase in profile length corresponds to  
726 ~50% increase in  $k_{sn}$ . Increasing the length of profiles, while holding bin size constant, increases  
727 the granularity with which orographic gradients in hydroclimatic parameters are represented by

728 creating more bins for a given elevation gradient. Because both bin size and profile length impact  
729 the granularity of orographic gradients in runoff parameters, we also did a test where we changed  
730 the length of the profiles (10- and 50-km) for different bin numbers (Figure 7D). Systems of  
731 different lengths had similar values for  $k_{sn}$  as long the number of bins was the same. More bins,  
732 and thus finer resolving power of gradients in runoff parameters, led to slight increases in steady  
733  $k_{sn}$ . For example, a 2X increase in bin number led to ~15% increase in  $k_{sn}$ , albeit within  
734 uncertainty of estimated values.

## 735 **6 Discussion**

736 Adding complexity to geomorphic transport laws like stream power is only useful to the  
737 degree that a new model is able to: (1) Be implemented over the spatiotemporal scales of  
738 interest; (2) Capture dynamics that cannot otherwise be simulated; and (3) Improve the ability to  
739 calibrate models and test hypotheses with empirical data. Given that stream power is one of the  
740 most widely used erosion laws in landscape evolution studies, we critically evaluate the results  
741 from our model analysis using spatial-STIM. First, we first compare spatial-STIM model results  
742 to its stream-power based predecessors. Second, we articulate the scenarios where and when  
743 spatial-STIM has the potential to provide more physically based and empirically constrained  
744 predictions. Third, we discuss the limitations of this new 1-D model, along with ideas for future  
745 research directions.

### 746 **6.1 Spatial-STIM and its predecessors**

747 One useful lens through which to consider model results is in how spatial-STIM  
748 predictions compare to other 1D models built on stream power (Howard, 1994; Whipple &  
749 Tucker, 1999). We focus on three important metrics to evaluate how our new model compares to

750 its predecessors—namely the steady state channel steepness, the steady state concavity, and the  
751 response times to steady state.

### 752 6.1.1 Steady state channel steepness

753 Figure 8 shows the steady state relationships between channel steepness and erosion rates  
754 for our regional cases using both linked and unlinked parameters. We plot results both in terms  
755 of  $k_{sn}$  and  $k_{snQ}$  using a reference channel concavity of 0.5 (see section 6.1.2 for discussion on  
756 patterns in concavity). For any given scenario, all model results are well approximated by a  
757 power law, similar to predictions from simple stream power (e.g., Equation 8). In general, power  
758 law fits of channel steepness show strongly sublinear behavior and imply stream power values of  
759  $n$  of 4.5-5.5 for linked scenarios and 6.1-16.6 for unlinked scenarios (Figure 8A). That individual  
760 scenarios imply different values for  $K$  and  $n$  should be expected because these stream power  
761 parameters encode details of both climate and rock properties (e.g., Kirby & Whipple, 2012;  
762 Whipple et al., 2022), the former of which we are explicitly varying in each different scenario.  
763 However, the wide range and large magnitudes of  $n$  are a bit more surprising and could be  
764 interpreted in empirical datasets as channel steepness thresholds (Hilley et al., 2019). Consistent  
765 with other stochastic-threshold models of river incision (see Lague, 2014), effective values of  $n$   
766 are expected to correlate with the shape parameter of the runoff distribution (Figure 9A), though  
767 our results are not entirely analogous. The relationship between the shape parameter of the runoff  
768 distribution and  $n$  largely emerges from the unlinked cases in our model results. For the linked  
769 cases, which are more analogous to the Lague et al. (2005) model, similar runoff variabilities  
770 produce a more modest range of values for  $n$ . Our data does largely overlap with the predicted  
771 relationship between the shape parameter and  $1/n$  from Lague et al., (2005) assuming a case  
772 where erosion thresholds are large with respect to erosion rates (Figure 9A), but is slightly better

773 explained by a simple linear relationship. Intriguingly, a negative correlation between  $K$  and  
774 mean runoff emerges from the spatially varying hydroclimatic rules used to evolve the profiles  
775 (Figure 9C).

776 We also present the corresponding topography - erosion rate relationships using an  
777 alternative calculation of channel steepness,  $k_{snQ}$ . We do this to explore whether normalizing our  
778 calculations by spatial gradients in runoff can help collapse model results onto a single functional  
779 form, thus following up on the recent empirical successes of using  $k_{snQ}$  (Adams et al., 2020;  
780 Leonard et al., 2023b, 2023a). Using  $k_{snQ}$  instead of  $k_{sn}$  does reduce the overall range of stream  
781 power values of  $n$  to  $\sim 3.3 - 3.6$  for linked cases and  $\sim 3.8 - 10.3$  for unlinked cases (Figure 8B).  
782 Within either linked or unlinked models, this also collapses the range for individual regions,  
783 though much more so for the linked than unlinked scenarios. Despite these modest improvements  
784 in using  $k_{snQ}$ , this modified form of channel steepness does not collapse model results onto a  
785 single relationship as might otherwise be expected for model runs with the same underlying rock  
786 properties (i.e., same values for  $k_e$ ,  $\tau_c$ , and  $k_w$ ). The point is emphasized further in the persistence  
787 of trends between shape parameter and  $n$  (Figure 9B) and runoff and  $K_{lp}$  (Figure 9D) for values  
788 from the  $k_{snQ}$ - $E$  relationships (Figure 8B). The overall relationships between stream power  
789 parameters and the two different calculations of channel steepness are quite similar, though they  
790 differ in detail as the rank order of values change between  $k_{sn}$  (Figure 9A; 9C) and  $k_{snQ}$  (Figure  
791 9B; 9D).

### 792 6.1.2 Steady state concavity

793 Other 1D river incision models show that steady state concavity is differentially sensitive  
794 to orographic gradients in precipitation as a function of rock uplift rate (Roe et al., 2003), though  
795 they typically fall within the range of expected values between 0.4 and 0.6 (Whipple et al.,

796 2022). As such, we consider best-fit concavities both using drainage area (Figure 8C) and  
797 precipitation-weighted drainage area (Figure 8D). For each model run, we determine the best-fit  
798 concavity by using the linear relationship between  $\chi$ -elevation or  $\chi_Q$ -elevation (sensu Leonard et  
799 al., 2023b). All model runs use a ratio of the area exponent,  $m$ , to the slope exponent,  $n$ , of 0.5.  
800 Deviations from this value thus indicate concavity anomalies induced by differences in how  
801 runoff is generated in the model. The range of concavities spans from  $\sim 0.3$  to 0.5. Importantly,  
802 unlinked scenarios consistently develop profiles with concavities  $< 0.5$ , consistent with the  
803 spatial pattern of  $k_{sn}$  observed in the steady state profiles of those models (e.g., Figure 4B). In  
804 contrast, linked scenarios consistently develop profiles with concavities  $\sim 0.5$ . For linked  
805 scenarios, the largest negative anomalies (i.e., negative deviations from 0.5) occur at the lowest  
806 uplift rates, which then approach the expected concavity of 0.5 at higher rock uplift rates.  
807 However, examination of along profile patterns in  $k_{sn}$  for these high uplift rate, linked models  
808 (e.g., Figure 4B) suggest that the apparent match of concavities masks persistent deviations in  $k_{sn}$   
809 in the upper reaches of the profile. Because there is a tradeoff between the relative roles of mean  
810 runoff and daily runoff variability on erodibility, numerical models like spatial-STIM are needed  
811 to identify how sensitive concavity is to rock uplift rates. For a given set of hydroclimatic  
812 parameters, concavity can vary by  $\sim 0.1$ . We also note that precipitation-weighted concavity for  
813 unlinked models (Figure 8D) shows more sensitivity to rock uplift rates than conventional  
814 calculations of concavity. This is the opposite of the effect described in Leonard et al. (2023b)  
815 where these authors showed that precipitation-weighted concavity reduces the dynamic range of  
816 values observed in central Andean drainages. Based on this, we suggest that systematic changes  
817 in channel concavity with rock uplift rates may provide important insights into the importance of  
818 orographic effects on runoff parameters. In particular, we hypothesize that the relative scale of

819 runoff generating events to the size of a watershed may be imprinted in the concavity. We return  
820 to this idea in section 6.2.

### 821 6.1.3 Transient response timescales

822 Stream power predictions of steady state morphology are non-unique (Gasparini &  
823 Brandon, 2011). By instead targeting the functional relationship between channel steepness and  
824 erosion rate for a given set of environmental conditions (e.g., rock properties, climatic setting),  
825 stream power predictions are more discriminating, but are still non-unique. For example, there is  
826 always a  $K$  and  $n$  - or  $K_{lp}$  and  $n$  - pair that can describe the expected steady state topography  
827 produced by our model outputs in each of the simulated scenarios (Figures 8-9). As such, we  
828 consider here whether differences in model dynamics are observed in the transient response of  
829 the 1D river profiles. To assess this, we compared the response times to steady state for both  
830 spatial-STIM and simple stream power. We calculated the analytical solution to stream power  
831 using the equations in Whipple (2001). Using the Hack parameters from model initialization (Eq.  
832 21), we can derive the analytical solution for response times using the fit values for  $K$  and  $n$  in  
833 each model scenario. To do this, we first back-calculate the initial rock uplift rates that  
834 correspond to the initial  $k_{sn}$  of 25 m used in all model runs. We then calculate the fractional  
835 change in rock uplift rates and apply the equations in Whipple (2001) to calculate a response  
836 time. For comparison to spatial-STIM, we have to also define steady state in our numerical runs.  
837 We define the time to steady state as the time it takes for the absolute value of the difference  
838 between maximum elevations of the profiles to fall below 10% of the amount of uplift per  
839 timestep. This was used to account for the continual time variation in profiles for unlinked cases.  
840 Figure 10 summarizes these calculations and includes direct comparison between spatial-STIM  
841 and the analytical solutions for stream power (Figure 10C). Response times for spatial-STIM plot

842 very close to the 1:1 line, suggesting broad agreement. Importantly, while simple stream power  
843 model can reproduce the transient dynamics of spatial-STIM, the values of  $K$  and  $n$  cannot be  
844 derived from first principles. In other words, the values for these parameters are not readily  
845 inferred from known differences in modern estimates of mean runoff and daily runoff variability  
846 used in our three regional scenarios.

#### 847 6.1.4 Comparison of spatial-STIM and STIM

848 Some of the behavior we observe in our results are expected from prior applications of  
849 STIM (DiBiase & Whipple, 2011; Lague, 2014; Lague et al., 2005), namely that  $\Phi$  is directly  
850 related to the shape parameter of the streamflow distribution (Figure 9A). Furthermore, the  
851 general expectation that increasing relief and elevation leads to commensurate increases in mean  
852 runoff, snowmelt fraction, and the shape parameter of runoff distributions can be partially  
853 represented in zero-dimensional versions of STIM by altering the scaling exponent that relates  
854 drainage area to discharge. In fact, one key advantage of prior applications of STIM is that  
855 streamflow distributions can be linked to ecohydrological models driven by rainfall (e.g., Botter  
856 et al., 2009) or snowmelt (e.g., Schaefli et al., 2013). Under this theoretical framing, streamflow  
857 variability can then be derived from the characteristic timescale of runoff generating events, the  
858 hydrological response timescale, and the shape of the recession limb of the hydrograph (Deal et  
859 al., 2018). This physically based theory allows for the coupling of hydrology to bedrock river  
860 incision with a minimal set of parameters. However, at the mountain range scale, orographic  
861 effects can be substantial and runoff generation heterogeneous, making it difficult to couple  
862 ecohydrological models to bedrock river incision.

863 To begin to address this challenge, we adopted an empirical, rules-based approach to  
864 simulate how stochastic runoff coevolves with topography (Forte & Rossi, 2024b). By

865 incorporating orographic patterns in mean runoff and daily runoff variability that may or may not  
866 be autocorrelated, spatial-STIM can predict profile evolution with upstream variations in  
867 topography (Figure 4A-B) and hydroclimate (Figure 4C-E) that are not possible in spatially  
868 uniform variants of STIM. Importantly, predictions of relationships between  $k_{sn}$  and erosion rate  
869 differ between STIM and spatial-STIM (Figure 11, S5). To aid comparison, we use the mean  $k_{sn}$   
870 of the steady state profile and estimates of mean runoff and daily runoff variability to contrast  
871 spatial-STIM with its zero-dimensional equivalent using equation 18. This is akin to treating the  
872 model results as a natural watershed, with which we might attempt to characterize using STIM.  
873 Such comparisons highlight that erosion rates within spatial-STIM and those predicted by STIM  
874 are different by between 0.5-1.5x (Figure 11A, S6A-B). The differences between STIM and  
875 spatial-STIM are more extreme for the unlinked cases than the linked ones. As catchments  
876 become smaller (and thus the degree of orographic variation within catchments becomes  
877 smaller), predictions of zero-dimensional STIM and spatial-STIM become more similar (e.g.,  
878 note the 10-km long profile runs in Figure 11A). Similarly, if we use the mean runoff and  
879 variability of individual model runs to predict suites of  $k_{sn}$ -erosion rate relationships, we find  
880 relatively large differences in  $n$  between zero-dimensional STIM and spatial-STIM (Figure 11B,  
881 S6C-D). Spatial-STIM tends to be less linear (i.e., higher  $n$ ) for linked models and more linear  
882 (i.e., lower  $n$ ) for unlinked models (Figure 11D). This analysis highlights that when interpreting  
883 empirical  $k_{sn}$ -erosion rate relationships from cosmogenic erosion rates, one should be mindful of  
884 the potential for orographic gradients in relevant STIM parameters (i.e., mean runoff and  
885 variability), but also the spatial scale of runoff events (i.e., whether a linked or unlinked case is  
886 more appropriate). In scenarios where there appear to be orographic gradients within individual  
887 basins and/or that the scale of runoff individual events tend to be smaller than the basin itself,

888 interpreting  $k_{sn}$ -erosion rate data with a zero-dimensional STIM model may be difficult to relate  
889 to empirical constraints on runoff parameters.

## 890 6.2 Why use spatial-STIM?

891 The stream power approximation for each scenario simulated in this study adequately  
892 explains both the steady state and transient response of river profiles. However, there are other  
893 reasons to favor using spatial-STIM for some applications. In particular, it provides insight into  
894 how process representation dictates model dynamics. Tethering process to the stochastic  
895 properties of runoff generation as function of relief development and spatial scale has potentially  
896 important implications on climate tectonic coupling.

### 897 6.2.1 Process representation in spatial-STIM

898 Any attempt to calibrate a 1D model of river incision is going to attempt to constrain free  
899 parameters using observational data. While most of our model parameters are fixed, we were  
900 able to produce a wide range of behaviors in spatial-STIM by simply including empirical  
901 patterns between mean runoff and daily runoff variability for three regional settings.  
902 Surprisingly, the details of hydroclimatic rules were less important than one new structural  
903 element to our model (i.e., the linking or unlinking of the recurrence interval of individual runoff  
904 events across bins) that essentially handles the spatial autocorrelation of runoff events. As an  
905 illustrative example, consider that we have good evidence for mixed populations of runoff  
906 generating events being sourced from snowmelt and rainfall-runoff in the Greater Caucasus  
907 (Forte et al., 2022). Using the same set of hydroclimatic rules, the  $K$  and  $n$  for linked and  
908 unlinked cases are very different. Attempting to fit stream power parameters to explain a mixture  
909 of the two endmembers and would likely produce hybrid values of  $K$  and  $n$  that are not reflective

910 of either runoff source or the expected behavior of the system (e.g., response times or the use of  
911 channel steepness to predict erosion rates). One could imagine that the differences between  
912 linked and unlinked models in terms of  $k_{sn}$ -erosion rate relationships (e.g., Figure 8A) reflect  
913 envelopes on possible  $k_{sn}$ -erosion rate datasets, and thus a wide array of  $K$  and  $n$  values (with  $K$   
914 being in part of a function of  $n$ ) that could be fit to the data. In all circumstances, the fit  $K$  and  $n$   
915 would not be physically meaningful.

916         Because of how runoff processes are represented in spatial-STIM, our model analysis  
917 highlights that unlinked models are quite sensitive to event size (Figure 7A) and watershed size  
918 (Figure 7C). These findings place central importance on understanding the hydroclimatic  
919 controls on the ratio of these two spatial scales (Figure 7D) if we want to understand the  
920 topographic response to base level fall. Empirical studies (e.g., Binnie et al., 2007; Cyr et al.,  
921 2010; DiBiase et al., 2010; Forte et al., 2022; Harkins et al., 2007; Miller et al., 2013; Olivetti et  
922 al., 2012; Ouimet et al., 2009; Rossi et al., 2017; Safran et al., 2005; Scherler et al., 2014)  
923 typically sample across a range of watershed sizes that may be interacting in complex ways with  
924 the characteristic scale of runoff generating events. Given this strong sensitivity to spatial scale,  
925 it is unclear how generalizable empirical estimates of  $K$  and  $n$  are when comparing across  
926 landscapes. While typical uncertainties associated with erosion thresholds (e.g., Shobe et al.,  
927 2018), rock erodibility (e.g., Yanites et al., 2017), channel width scaling (e.g., Gallen &  
928 Fernández-Blanco, 2021), and sediment flux dynamics (e.g., Whipple & Tucker, 2002) still  
929 remain (and were not explored in this analysis), we argue from our simulations that we may not  
930 be accounting even for the most important aspects of climate in current models of bedrock river  
931 incision. As such, there is a need for providing mechanistic explanations of the “linked” versus  
932 “unlinked” scenarios.

## 933 6.2.2 Physical interpretations of unlinked vs linked scenarios

934 Given the central importance of whether the recurrence times of daily runoff are  
935 synchronous along the river profile (i.e., “linked” in the parlance of the model), there is a need to  
936 provide physical interpretations to this new structural element in the model. We argue that  
937 linking or unlinking runoff statistics spatially embeds a variety of physically distinct  
938 mechanisms. The first broad class of interpretations of the linking the recurrence times of daily  
939 runoff is that it, in part, it captures the spatial scale of rainfall events—particularly, the contrast  
940 between synoptic scale rainfall versus convective rainfall. While actual rainfall fields vary  
941 continuously, our bin-based treatment facilitates representing orographic gradients in daily  
942 rainfall that vary in magnitude but where the relative frequency is uniform (or not in the  
943 “unlinked” scenarios). Whether recurrence times are uniform at the event scale is an important  
944 consideration. In some cases, precipitation patterns during individual storms mirror long-term  
945 means (e.g., Garvert et al., 2007; Minder et al., 2008; Roe, 2005). In contrast, there is also deep  
946 literature documenting how event-scale gradients in precipitation properties are more sensitive to  
947 finer-scale topography leading to more complex outcomes (e.g., Cosma et al., 2002; Marra et al.,  
948 2022). To some extent, spatial-STIM can capture some of this nuance. Even the linked scenarios  
949 can develop significant complications in spatial patterns in runoff when lower relief areas persist  
950 upstream, leading to a relatively lower magnitude of runoff events. Nevertheless, the linked and  
951 unlinked scenarios reflect not only the atmospheric forcing but also how the hydrologic response  
952 self-organizes in the landscape as function of topography.

953 The second broad class of mechanistic interpretations of whether runoff events are  
954 spatially linked lies in the assumed hydrology that converts precipitation events into daily runoff  
955 distributions. At even the simplest level, this probabilistic transformation is nontrivial (e.g.,

956 Rossi et al., 2016) such that a naïve correspondence between runoff generating events and the  
957 spatial characteristics of precipitation events becomes problematic. Land surface properties like  
958 vegetation (Deal et al., 2018), soil thickness (Rossi et al., 2020), among others, may plausibly co-  
959 evolve with topography in ways that can partition the landscape into domains with distinctively  
960 different rainfall runoff statistics. Furthermore, we showed in our companion paper (Forte &  
961 Rossi, 2024b) that the spatial extent of snowmelt dominated runoff events tends to dominate the  
962 far right tail of runoff distributions, especially at higher intensity thresholds. While our treatment  
963 only provides a crude representation of the endmember cases of linked versus unlinked  
964 scenarios, it provides a useful baseline for the range of outcomes for a given hydroclimatic  
965 ruleset. From the perspective of steady state relationships between channel steepness and erosion  
966 rates, reality likely lies somewhere in between the linked and unlinked scenarios, producing a  
967 large number of potential  $K - n$  pairs that can be plausibly produced for even a simple  
968 hydroclimatic ruleset. More attention to understanding and characterizing how the statistics of  
969 runoff might be spatially autocorrelated via a variety of physical mechanisms is a potentially  
970 fruitful, and important, future research direction.

### 971 6.2.3 Isolating the effect of snowmelt

972 While the snowmelt transition was in part our initial target of model development, the  
973 model behavior we show in this analysis provides a suite of more general insights. As long as  
974 there is an inverse relationship between mean runoff and daily runoff variability (e.g., Molnar et  
975 al., 2006; Rossi et al., 2016) and erosional thresholds are large relative to characteristic discharge  
976 (e.g., Lague et al., 2005; Tucker, 2004), then the dynamics of our model simulations apply. To  
977 help isolate the role of integrating snowmelt statistics with rainfall runoff ones, we ran an  
978 additional suite of models that removes the chain of reasoning used to account for snowmelt.

979 Specifically, these additional model runs (referred to as Rain Only) use a single relationship  
980 between mean runoff and variability based on the WaterGAP3 analysis but that ignores the role  
981 of snowmelt fraction (Figure S6). For this set of experiments, we still use the regional  
982 relationships between local relief and runoff as baselines cases but ignore relationships between  
983 maximum elevation and snowmelt fraction. We consider both linked and unlinked scenarios  
984 using the Greater Caucasus and British Columbia rulesets. In the earlier runs, the Greater  
985 Caucasus models barely entered into the snowmelt-dominated regime whereas, at high uplift  
986 rates, the British Columbia models were well into the snowmelt dominated regime (e.g., Figure  
987 4C).

988         The suite of Rain Only models highlight again that whether a model is linked or unlinked  
989 dominates the nature of the  $k_{sn}$ -E relationship (Figure 12A). Comparing the original and Rain  
990 Only Greater Caucasus models reveals very minor differences in the nonlinearity of the  $k_{sn}$ -E  
991 relationship. Comparison of the British Columbia original and Rain Only models reveals a more  
992 substantial difference in nonlinearity for the unlinked cases. The original models that included  
993 snowmelt are more nonlinear (i.e., higher  $n$ ) than the Rain Only models. However, the Rain Only  
994 models are still extremely nonlinear (e.g.,  $n = 12$ ). Together, this suite of models strongly  
995 suggests that the dominant controls on the nature of the  $k_{sn}$ -E relationship are: (1) the  
996 development of an orographic gradient in both mean runoff and variability—which may be  
997 influenced by, but does not require, a transition to snowmelt hydrology, and (2) the spatial scale  
998 of runoff events.

999         Finally, it is worth highlighting that because the snowmelt transition is elevation  
1000 dependent and base level is fixed to zero in all runs, our results represent a minimum effect of  
1001 snowmelt for a given stream length. The snowmelt transition would be more dominant if either

1002 stream profiles were longer or if we considered streams that represented catchments in ranges  
1003 that drain to other base levels. We illustrate the importance of this assumption using a limited  
1004 suite of unlinked model runs at 1 mm/yr uplift rates for the Greater Caucasus and British  
1005 Columbia hydroclimatic rulesets, but where we set the local base level to either 1000 or 2000 m  
1006 (Figure 12C-G). For the Greater Caucasus rules, raising the base level to 1 km and 2 km  
1007 decreases the catchment averaged  $k_{sn}$  by 8.8% and 18.6%, respectively, compared to the 0 km  
1008 baselevel. For the British Columbia hydroclimatic rules, raising the base level by 1 km  
1009 decreases  $k_{sn}$  by 14.1%. Because almost of all the profile is in the snowmelt dominated regime at  
1010 1 km (Figure 12E), raising the baselevel to 2 km leads to a similar reduction in  $k_{sn}$  of 14.3%. The  
1011 reduction in  $k_{sn}$  from increasing snowmelt contribution at a constant uplift rate is a direct  
1012 outcome of the increasing value of both the mean runoff and the shape parameter, thus leading to  
1013 a general increase in the sublinearity of the  $k_{sn}$ -erosion rate relationship.

## 1014 6.2. Implications on climate-tectonic coupling

1015 We undertook this analysis to understand how orographic gradients in mean runoff and  
1016 daily runoff variability alter predictions for the topographic evolution of mountain ranges as they  
1017 grow (e.g., Figure 1). Specifically, we focused on the important transition from rainfall-  
1018 dominated probability distributions to snowmelt-dominated ones as topography grows, based on  
1019 our own findings in the Greater Caucasus (Forte et al., 2022). Analysis of WaterGAP3 model  
1020 data revealed that these hydrological transitions may be generally important to mid-latitude  
1021 mountain ranges where glacial erosion is limited (Forte & Rossi, 2024b). Our new 1D model of  
1022 river incision shows that if such orographic gradients are honored, then it is relatively easy to  
1023 generate highly sub-linear ( $5 < n < 16$ ) relationships between channel steepness and erosion  
1024 rates. We also found that this model behavior is generalizable, only requiring that variability is

1025 inversely correlated with mean runoff and that there are orographic gradients in mean runoff.  
1026 Snowmelt can act as an amplifier of this effect but is not required.

1027         Assuming a constant set of hydroclimatic variables as mountain ranges grow is likely  
1028 unrealistic, leading us to argue that increasingly sublinear relationships between topography and  
1029 erosion may be the norm and not the exception. Early hypotheses on climate-tectonic feedbacks  
1030 assumed that the most important orographic effects are in extracting precipitation on the  
1031 windward side and diminishing precipitation on the leeward side of topographic barriers (e.g.,  
1032 Beaumont et al., 1992; Whipple & Meade, 2006; Willett, 1999). Subsequent efforts focused on  
1033 the importance of mountain topography setting the spatial distribution of precipitation (Roe et  
1034 al., 2003) and phase of precipitation in mountain landscapes (Anders et al., 2008). While all  
1035 these orographic effects are undoubtedly important, our model simulations provide a natural  
1036 progression to these insights by also accounting for how stochastic runoff generation (DiBiase &  
1037 Whipple, 2011; Lague et al., 2005; Tucker, 2004) will itself be a function of the relief evolution  
1038 of mountain ranges. Our results highlight that a critical, and largely ignored, set of parameters  
1039 associated with the scale of runoff events with respect to watershed size may be fundamental to  
1040 understanding potential feedbacks between climate and tectonics.

### 1041         6.3 Limitations and Future Directions

1042         While our new model provides important insights into how orographic gradients in runoff  
1043 generation can impact stream-power based predictions for topographic relief, there are several  
1044 important limitations to our model analysis. First, we only use modern relationships between  
1045 local relief, mean runoff, maximum elevation, and snowmelt fraction at select locations to drive  
1046 model scenarios. Related to this assumption is that the observed relationships will persist across  
1047 geologically long periods of time, even though we know that mean precipitation varies across

1048 climate cycles, including glacial-interglacial forcing (e.g., Cruz et al., 2005; Wang et al., 2008).  
1049 As such, we would expect that both mean runoff, runoff variability, and snowmelt fraction  
1050 should all vary across glacial-interglacial cycles or larger climate transitions. The impact of these  
1051 fluctuations will be a function of both the elevation range of the orogen in question, but also its  
1052 latitude. One novelty of our model is that it makes the rules that describe how hydroclimatology  
1053 will coevolve with topographic relief explicit. To take advantage of this model feature in  
1054 simulating glacial-interglacial cycles, we need more detailed accounting for how these cycles  
1055 impact mean runoff and daily runoff variability through time. Second, in some locations, as  
1056 elevations and snow accumulation increases, glaciers will begin to develop. In such settings, we  
1057 would expect a transition from rainfall-dominated fluvial processes to snowmelt-dominated  
1058 fluvial processes to glacial-dominated processes as mountain ranges grow. We similarly expect  
1059 that the relative balance of these processes will fluctuate according to interglacial-glacial cycles  
1060 and/or climate transitions. We do not model the impact of glaciers here, but this would be an  
1061 important extension, especially in higher latitude locations. As such, our results are most relevant  
1062 to orogens that do not fully transition into being dominated by glacial erosion during glacial-  
1063 interglacial cycles. Third, the assumption of static relationships between hydroclimatic and  
1064 topographic variables assumes that these relationships are valid through all parts of a transient  
1065 topographic response. In reality, changing topography could impart more complicated  
1066 relationships. Fully addressing this would require something more akin to a 2D model of  
1067 orographic precipitation and runoff. Fourth, the discrete boundaries imposed by binning the river  
1068 profile is quite imperfect. Not only does it imply a scale beyond which runoff parameters can be  
1069 treated independently, it also fixes the location of these event boundaries in space. The arbitrary  
1070 locations of these bins are likely an unrealistically hard constraint on the event-scale properties

1071 of snowmelt- and rainfall-runoff events. Fifth, we make a simplifying assumption that the  
1072 erosional threshold (Eq. 17) is temporally and spatially fixed in all models. In reality, erosional  
1073 thresholds might be expected to vary in both time and space, e.g., as a function of erosion rate  
1074 and delivery of large blocks to streams from hillslopes (e.g., Shobe et al., 2018). In theory, one  
1075 could attempt to build similar empirical relationships between topographic, tectonic, or  
1076 hydroclimatic parameters in the model to also vary the threshold in a sensible way, making it an  
1077 important future research direction.

1078         Keeping these limitations in mind, we highlight a few promising directions for future  
1079 modeling and data analysis on this topic. As computational power increases, we are seeing more  
1080 realistic simulations of orographic precipitation in bedrock river incision modeling (e.g., Han et  
1081 al., 2015; Shen et al., 2021). Our results suggest that these efforts would benefit from bringing  
1082 commensurate improvement in the land surface models that convert precipitation to runoff. For  
1083 mid-latitude mountain landscapes, it is important to honor the importance of precipitation phase  
1084 on orographic gradients in runoff patterns (e.g., Anders et al., 2008; Forte et al., 2022; Rossi et  
1085 al., 2020). Similarly, prior studies highlight the potential importance of Milankovitch forcings on  
1086 precipitation for landscape evolution (Godard et al., 2013). How these cyclical variations of  
1087 precipitation are then converted to mean runoff, daily runoff variability, and snowmelt fraction is  
1088 thus an important unknown. Our focus on the form of  $k_{sn}$ - $E$  relationships suggests that a natural  
1089 extension of this work should also be to examine how spatial-STIM might alter coupled models  
1090 between climate and tectonics. Relatively simple analytical approaches to this problem (Whipple  
1091 & Meade, 2004, 2006), as well as more complex dynamical models (e.g., Braun & Yamato,  
1092 2010; Roe et al., 2006; Stolar et al., 2007), have yielded important insights into potential  
1093 feedbacks between climate and tectonics. While we can say that the dynamics in our 1D model

1094 will act to dampen such feedbacks, the question of how much is still open and deserves more  
1095 careful study.

1096         Finally, the assumption of spatial autocorrelation of runoff events proved to be the  
1097 strongest regulator of erosional efficiency in our new model structure. Within the context of a 1D  
1098 profile model like ours, having events that are stochastic in space and time is challenging, but not  
1099 insurmountable. As such, we need more hydrological studies that can help us generalize the  
1100 spatial statistics of rainfall- and snowmelt-runoff events. Promising work characterizing  
1101 potentially significant spatial variability in precipitation patterns in high relief landscapes exist  
1102 (e.g., Anders et al., 2006, 2007; Barros et al., 2000; Campbell & Steenburgh, 2014; Frei & Schär,  
1103 1998; Minder et al., 2008), but generalizing these into how this spatial stochasticity is, or is not,  
1104 reflected in runoff at a similar scale remains unclear. Similarly, the analysis of WaterGAP3 data  
1105 by Forte & Rossi (2024b) suggested a fundamental relationship between runoff event size and  
1106 the contribution from snowmelt. Events with larger spatial footprints appear to be dominated by  
1107 snowmelt events, further highlighting the interconnectedness of many of the parameters we  
1108 consider. While fully distributed hydrological models come at a high computational cost for  
1109 landscape evolution studies, statistical descriptions of these dynamics may be tractable over  
1110 landscape evolution timescales. Furthermore, the way space is represented in 1D river profiles  
1111 may not be able to fully mimic the spatial statistics of runoff events, thereby requiring 2D  
1112 landscape evolution modeling. The Landlab modeling library (Barnhart et al., 2020; Hobbey et  
1113 al., 2017) already has many of the process components suited to implementing spatial-STIM in a  
1114 2D framework. Thus, understanding how well we have captured spatiotemporal stochasticity  
1115 using the assumptions of our 1D model is an important open question that should be tested in 2D  
1116 (Tucker, 2004; Tucker & Bras, 2000). Despite the clear needs for refining and understanding the

1117 applicability of spatial-STIM, our findings show that simply accounting for spatial variations in  
1118 daily runoff variability is an important step towards generating testable predictions for the  
1119 erosion laws used by our community.

## 1120 **7 Conclusions**

1121 Results from simulations using our new empirically driven 1D profile model that  
1122 considers both temporal and spatial stochasticity in runoff and snowmelt events highlight that  
1123 generally sublinear relationships between channel steepness and erosion rate are an expected  
1124 outcome of orographic development within mountain ranges. Specifically, because of the linkage  
1125 between mean runoff and runoff variability, the development of orographic gradients in runoff  
1126 statistics should be expected. Such feedbacks may also be strengthened by the tendency for the  
1127 increasing elevation of mountain ranges to preferentially accumulate snow, driving a greater  
1128 component of runoff to be related to snowmelt, and further reducing the variability of runoff.  
1129 Given the expectation that decreasing runoff variability should lead to increasingly sublinear  
1130 channel steepness erosion rate relationships, this implies a potential negative feedback on the  
1131 topographic growth of mountain ranges, providing a process-based explanation for the  
1132 observation of pseudo-thresholds in channel steepness erosion rate relationships. While basic  
1133 aspects of this are expected and predictable from prior analyses using STIM, we show here that  
1134 orographic gradients in mean runoff and variability change fundamental details of model  
1135 predictions.

1136 A critical outcome of our model results is also that a fundamental parameter for  
1137 controlling the nature of channel steepness erosion rate relationships is the extent to which the  
1138 probability of exceedance of runoff events within a given catchment are linked or unlinked.  
1139 These two endmember states roughly correspond to the extent to which runoff generating events

1140 in a given catchment tend to be dominated by spatially restricted convective storm events or  
1141 larger-scale synoptic events. All other things equal, unlinked scenarios predict steeper landscapes  
1142 than the equivalent linked scenarios. This implies a fundamental scale dependence on the nature  
1143 of the relationship between channel steepness and erosion rates. For a given set of  
1144 hydroclimatological parameters the resulting channel steepness erosion rate pattern can be fit by  
1145 a simple stream power relationship. However, the extent to which this is meaningful in real  
1146 datasets, where linked and unlinked dynamics are ignored, is unclear. Ultimately, our results  
1147 have important implications not only for our understanding of expected coupling between  
1148 hydroclimatology, topography, and tectonics as a mountain range grows, but also the type of  
1149 observations we as a community should be considering within our datasets. Future work should  
1150 focus on considering the implications of spatial and temporal stochasticity of runoff and  
1151 snowmelt events. There is also a great need for better empirical quantification of the  
1152 characteristic spatial and temporal scale of runoff events within mountainous catchments and  
1153 how they evolve with time through glacial-interglacial cycles.

1154

## 1155 **Acknowledgments**

1156 Support for M.W. Rossi came from the Geomorphology and Land-use Dynamics (GLD)  
1157 Program (EAR-1822062). Neither AMF or MWR have any real or perceived financial or other  
1158 conflicts with the contents of this work. We thank Mikael Attal for editorial handling. We also  
1159 thank Associate Editor Liran Goren and reviewers Eric Deal, Alison Anders, and an anonymous  
1160 reviewer for probing comments that improved this work.

1161 **Open Research**

1162           Analysis and model codes necessary to reproduce this work are available in Forte (Forte,  
1163 2024). All model results, additional figures summarizing the results of each model run, and  
1164 larger outputs of the processing steps are available in Forte & Rossi (2024a). Portions of these  
1165 analysis codes rely on publicly available datasets that we do not have permission to redistribute,  
1166 but when used, we provide comments in the code referencing where these datasets can be  
1167 downloaded.

1168

1169 **Figures**

1170 **Figure 1.** Conceptual model of how the covariation of topography, mean runoff, snowmelt  
 1171 fraction of runoff, and runoff variability might influence the  $k_{sn}$ -E relationship as topography  
 1172 grows, based on expectations from empirical relationships developed in Forte & Rossi (2024b).  
 1173 A) Relationships between local relief and mean runoff (solid line) and maximum elevation and  
 1174 the fraction of runoff derived from snowmelt (dashed line). Horizontal dotted line indicates  
 1175 snowmelt fraction where runoff-variability relationships transition from a power law to a linear  
 1176 form. Colored dots represent hypothetical states as topography grows. B) Relationship between  
 1177 mean runoff and variability. Solid line is a power law relationship that characterizes conditions  
 1178 when snowmelt contribution is low. Dashed line is a linear relationship that characterizes  
 1179 conditions when the snowmelt contribution is significant. C) Implied  $k_{sn}$ -E relationships for the  
 1180 different mean runoff - variability relationships from B. D) Schematic envisioning how the  
 1181 relationships in A-C might evolve through time and space as a mountain range grows. The color  
 1182 of dots correspond to colors shown in A-C.

1183

1184 **Figure 2.** Summary of empirical results from Forte & Rossi (2024b) relate topography and  
 1185 hydroclimatological variables of interest. A) Relationship between mean daily runoff ( $\bar{R}$ ) and  
 1186 daily runoff variability as parameterized by the Weibull shape parameter ( $c_R$ ). Colored lines  
 1187 indicate individual fits to  $\bar{R}$  and  $c_R$  within bins of snowmelt fraction (SF). Red solid lines are  
 1188 power law fit for bins with  $SF < 0.35$  and blue dashed lines for bins with  $SF > 0.35$ . B)  
 1189 Relationship between the scale parameter implied by the mean runoff and that fit to the runoff  
 1190 distributions above an exceedance threshold. Symbology is similar to A but lines show linear  
 1191 regressions. C) Power law fits between mean local relief and  $\bar{R}$  for three regional examples using  
 1192 WaterGAP3 data. D) Power law fits between maximum elevation and SF for three regional

1193 examples using WaterGAP3 data. In both C and D, the symbols are scaled to the number of  
1194 observations and whiskers show one standard deviation. More details on regressions for each  
1195 panel can be found in Forte & Rossi (2024b, 2024a).

1196

1197 **Figure 3.** A) Longitudinal profile of model GC1U at 1 Myr into the model run (colored line with  
1198 black squares), where colors indicate individual bins and black squares mark bin boundaries.  
1199 Also shown is the mean  $k_{sm}$  for each bin (colored circles) B) Same as in A but for model GC1L at  
1200 0.63 Myr into the model run, which represents a comparable point in the transient response. C)  
1201 Mean runoff and variability for GC1U at 1 Myr. Colored squares are mean runoff and variability  
1202 for the individual bins. White square is runoff and variability from a drainage area weighted  
1203 mean of the bins. The black circle is the median of 500 trials of mean runoff and variability from  
1204 routing 100 years of discharge for each trial, where small gray dots are mean runoff and  
1205 variability for individual trials. This overlain on a histogram of the runoff within bins to  
1206 emphasize that many of the bins have runoffs clustered around the mean. D) Same as in C but for  
1207 model GC1L at 0.6 Myr. E) Exceedance frequency plot for GC1U at 1 Myr, showing the  
1208 probability distributions for individual bins as thin colored lines, the area-weighted mean runoff  
1209 and variability as the black dashed line, and the mean runoff and variability from the median of  
1210 the 500 trials as the black dashed line. The colored squares represent runoff for each individual  
1211 bin on a random day. F) Same as E but for model GC1L at 0.6 Myr. Note that the difference  
1212 between the assortment of frequencies and runoffs on the random days (small squares) between  
1213 E) and F) result from E) being an unlinked model and F) being a linked model. Because F) is  
1214 linked, the runoff magnitude for the random day shown all plot at a single recurrence interval.

1215

1216 **Figure 4.** Steady-state results for both unlinked (solid lines) and linked (dashed lines) models  
 1217 across the full range of uplift rates (0.25 – 8 mm/yr) for three regional cases (left column -  
 1218 Greater Caucasus, middle column – Alps, right column – British Columbia). The fourth column  
 1219 shows mean values of each quantity within the row for all three locations. Lines are colored by  
 1220 uplift rate. Rows show how A) elevation, B) mean  $k_{sn}$  within bins, C) snowmelt within bins, D)  
 1221 mean daily runoff within bins, and E) runoff variability within bins vary as a function of stream  
 1222 distance. Note that these values represent the final 40 timesteps (representing 200,000 years of  
 1223 model time). This time-averaging was done because the individual timesteps show significant  
 1224 variability between output timesteps.

1225

1226 **Figure 5.** Representative stream profile evolution for an unlinked (left column) versus linked  
 1227 model (right column) for the Greater Caucasus uplifting at 1 mm/yr. A)  $\chi$ -elevation for model  
 1228 GC1U through time showing 40 equally spaced time slices. B) Same as in A but for GC1L. C)  
 1229 Stream profile for model GC1U through time for the same 40 equally spaced time slices as in A.  
 1230 D) Same as in C but for GC1L. E) Average erosion rate between outputs along the profile for  
 1231 model GC1U for all output time slices. F) Same as in E but for GC1L. G) Mean runoff within  
 1232 bins for all output time slices for model GC1U. H) Same as in G but for model GC1L.

1233

1234 **Figure 6.** Frequency of exceedance of the erosion threshold between output timesteps in an  
 1235 unlinked (left column) versus linked (right column) scenarios, specifically for the Greater  
 1236 Caucasus uplifting at 1 mm/yr. A) Plot of frequency of exceedance as a function of profile  
 1237 distance (x) and model time (y) for the unlinked GC1U model. The area of consistently higher  
 1238 frequency of exceedance tracks the movement of the knickpoint through the profile. B) Same as

1239 in A but for the linked GC1L model. C) Cumulative frequency of exceedance of the erosion  
1240 threshold across the entire model run as a function of stream distance for unlinked model GC1U.  
1241 D) Same as in C but for linked model GC1L. E) Mean (solid lines) and maximum and minimum  
1242 (dashed lines) frequency of erosion threshold exceedance through time for the GC1U model. F)  
1243 Same as in E, but for the linked model GC1L. G) Individual frequencies of exceedance of  
1244 erosion threshold at a specific node compared to the average erosion rate of that node for all time  
1245 steps for unlinked model GC1U. H) Same as in G, but for linked model GC1L.

1246

1247 **Figure 7.** Summary of sensitivity experiments. Black circles and squares indicate results of  
1248 reference experiments shown previously, and gray symbols indicate results from sensitivity test.  
1249 Triangles are used to show results using area binning. In A-D, uplift rate is 1 mm/yr and the  
1250 Greater Caucasus hydroclimatic ruleset is used. A) Sensitivity to bin size used for runoff  
1251 parameters. See Figure S3 for steady-state output of relevant models. B) Sensitivity to the  
1252 imposed maximum relief. See Figure S3 for steady-state output of relevant models. C)  
1253 Sensitivity to the profile length. See Figure S3 for steady-state output of relevant models. Note  
1254 that for all of these models, the bin size is kept at 2 km, so different profile lengths imply a  
1255 different number of bins. D) Sensitivity to the number of bins, comparing models that are either  
1256 50 km (squares - GC1U-5B, GC1U-10B) or 10 km (circles - GC1U-10L, GC1U-10L-1B) long.  
1257 E) Sensitivity to equal river length binning (black circles and squares) versus equal area binning  
1258 (AB - gray triangles) across the full range of uplift rates used in numerical experiments.

1259

1260 **Figure 8.** A) Mean  $k_{sn}$  and erosion rate at quasi-steady state. Lines are power law fits to model  
1261 results in a stream power context. Equivalent  $n$  values for each stream power relationship are  
1262 shown in the legend. Note each point includes uncertainty as the standard error on the mean, but  
1263 are generally less than the width of the symbols. B) Same as in A but calculating  $k_{snQ}$  sensu  
1264 Adams et al., (2020), which uses precipitation as a proxy for runoff to calculate discharge. To  
1265 accomplish this in our 1D model results (which do not formally calculate precipitation), we use  
1266 empirical relationships between runoff and precipitation from WaterGAP3 for each region to  
1267 estimate precipitation based on the modelled runoff. We compare the results of calculating  $k_{snQ}$   
1268 directly from runoff in Figure S4, but ultimately the differences are subtle. C) Best fit concavity  
1269 ( $\theta$ ) for models using drainage area. Dotted line is the expected concavity of 0.5 given the input  
1270 values in the model D) Best fit concavity for models using precipitation weighted drainage area  
1271 sensu Leonard et al., (2023b).

1272

1273 **Figure 9.** A) Mean shape parameter across models for a given scenario compared to  $1/n$  from fits  
1274 in 8A. Solid line is linear fit through the data. Dashed line is expected relationship from Lague et  
1275 al., (2005) after converting Weibull shape parameters to inverse gamma ones using the  
1276 relationship in Rossi et al., (2016). B) Mean variability across models for a given scenario  
1277 compared to  $1/n$  from fits in 8B, i.e., when fitting a relationship between  $k_{snQ}$  and erosion rate. C)  
1278 Mean runoff across models for a given scenario compared to  $K$  from fits in 8A. D) Mean runoff  
1279 across models for a given scenario compared to  $K_{lp}$  from fit in 8B. Symbol style is shared across  
1280 all plots.

1281

1282 **Figure 10.** Comparison of analytical steady state (SPIM) to empirical steady state (STIM). A)  
1283 Estimated time to steady-state from model initiation using the change in maximum elevation  
1284 between saved timesteps and defining steady-state as when the absolute value of this metric  
1285 drops below 10% of the amount of uplift per timestep. B) Analytical solution for response times  
1286 using estimates of  $K$  and  $n$  from Figure 8. The initial uplift rate for each model uses this  $K$  and  $n$   
1287 and the starting  $k_{sn}$  (25 m) to calculate the appropriate fractional change in uplift rate sensu  
1288 Whipple (Whipple, 2001). C) Comparison of the empirical and analytical response times.

1289

1290 **Figure 11.** Comparison of zero-dimensional STIM predictions and spatial-STIM results. A)  
1291 Ratio of erosion rates from two models as a function of spatial-STIM erosion rates. Direct  
1292 comparison of values with uncertainty shown in Figure S5A. B) Comparison of power law  
1293 exponent  $n$  for zero-dimension STIM and spatial-STIM. Note that for each model suite (i.e., a  
1294 given regional hydroclimatic ruleset where bin are either linked or unlinked), there are 6 possible

1295 values of  $n$  predicted from zero-dimensional STIM. This is because each uplift rate generally  
1296 produces a different catchment averaged runoff and variability and thus predicts a different  $k_{sn}$ -E  
1297 relationship with a corresponding  $n$  value. Error bars represent uncertainty on the exponent from  
1298 the fitting algorithm. Individual zero-dimensional STIM  $k_{sn}$ -E relationships are shown in Figure  
1299 S5C.

1300

1301 **Figure 12.** Comparison of Rain Only models and the influence of base level. A) Erosion rate  
1302 versus  $k_{sn}$  and relevant power law fits for unlinked and linked models for the Greater Caucasus  
1303 and British Columbia compared against similar runs using the Rain Only model. B) Maximum  
1304 snow fraction as a function of erosion rate for scenarios that include snowmelt fraction in ruleset.  
1305 Right column compares along-profile variation in C) Elevation relative to imposed base level  
1306 (BL), D)  $k_{sn}$ , E) Snow fraction, F) Mean runoff, and G) Variability. All models on right column  
1307 were run with a 1 mm/yr uplift rate and are unlinked. This compares the regular models (set to a  
1308 base level of 0), rain only models (set to a base level of 0), and a suite of models with base level  
1309 to set to either 1 or 2 km.

1310

## 1311 **References**

- 1312 Adams, B. A., Whipple, K. X., Forte, A. M., Heimsath, A. M., & Hodges, K. V. (2020). Climate controls on erosion  
1313 in tectonically active landscapes. *Science Advances*, 6(42). <https://doi.org/10.1126/sciadv.aaz3166>
- 1314 Ahnert, F. (1970). Functional relationships between denudation, relief, and uplift in large mid-latitude drainage  
1315 basins. *American Journal of Science*, 268, 243–263.

- 1316 Alcamo, J., Döll, P., Henrichs, T., Kaspar, F., Lehner, B., Rösch, T., & Siebert, S. (2003). Development and testing  
1317 of the WaterGAP 2 global model of water use and availability. *Hydrological Sciences Journal*, 48(3), 317–  
1318 337. <https://doi.org/10.1623/hysj.48.3.317.45290>
- 1319 Anders, A. M., Roe, G. H., Hallet, B., Montgomery, D. R., Finnegan, N. J., & Putkonen, J. (2006). Spatial patterns  
1320 of precipitation and topography in the Himalaya. In S. D. Willett, N. Hovius, M. T. Brandon, & D. M.  
1321 Fisher, *Tectonics, Climate, and Landscape Evolution*. Geological Society of America.  
1322 [https://doi.org/10.1130/2006.2398\(03\)](https://doi.org/10.1130/2006.2398(03))
- 1323 Anders, A. M., Roe, G. H., Durran, D. R., & Minder, J. R. (2007). Small-Scale Spatial Gradients in Climatological  
1324 Precipitation on the Olympic Peninsula. *Journal of Hydrometeorology*, 8(5), 1068–1081.  
1325 <https://doi.org/10.1175/JHM610.1>
- 1326 Anders, A. M., Roe, G. H., Montgomery, D. R., & Hallet, B. (2008). Influence of precipitation phase on the form of  
1327 mountain ranges. *Geology*, 36(6), 479. <https://doi.org/10.1130/G24821A.1>
- 1328 Barnhart, K. R., Hutton, E. W. H., Tucker, G. E., Gasparini, N. M., Istanbuluoglu, E., Hobbey, D. E. J., et al. (2020).  
1329 Short communication: Landlab v2.0: a software package for Earth surface dynamics. *Earth Surface*  
1330 *Dynamics*, 8(2), 379–397. <https://doi.org/10.5194/esurf-8-379-2020>
- 1331 Barros, A. P., Joshi, M., Putkonen, J., & Burbank, D. W. (2000). A study of the 1999 monsoon rainfall in a  
1332 mountainous region in central Nepal using TRMM products and rain gauge observations. *Geophysical*  
1333 *Research Letters*, 27(22), 3683–3686. <https://doi.org/10.1029/2000GL011827>
- 1334 Beaumont, C., Fullsack, P., & Hamilton, J. (1992). Erosional control of active compressional orogens. In K. R.  
1335 McClay (Ed.), *Thrust Tectonics* (pp. 1–18). New York: Chapman Hall.
- 1336 Berghuijs, W. R., Woods, R. A., Hutton, C. J., & Sivapalan, M. (2016). Dominant flood generating mechanisms  
1337 across the United States: Flood Mechanisms Across the U.S. *Geophysical Research Letters*, 43(9), 4382–  
1338 4390. <https://doi.org/10.1002/2016GL068070>
- 1339 Binnie, S. A., Phillips, W. M., Summerfield, M. A., & Fifield, L. K. (2007). Tectonic uplift, threshold hillslopes, and  
1340 denudation rates in a developing mountain range. *Geology*, 35(8), 743–746.  
1341 <https://doi.org/10.1130/G23641A.1>
- 1342 Bookhagen, B., & Burbank, D. (2006). Topography, relief, and TRMM-derived rainfall variations along the  
1343 Himalaya. *Geophysical Research Letters*, 33, L08405–L08405. <https://doi.org/10.1029/2006GL026037>

- 1344 Bookhagen, B., & Burbank, D. (2010). Toward a complete Himalayan hydrological budget: Spatiotemporal  
1345 distribution of snowmelt and rainfall and their impact on river discharge. *Journal of Geophysical Research*,  
1346 *115*(F03019). <https://doi.org/10.01029/02009JF001426>
- 1347 Bookhagen, B., & Strecker, M. R. (2008). Orographic barriers, high-resolution TRMM rainfall, and relief variations  
1348 in the eastern Andes. *Geophysical Research Letters*, *35*(L06403). <https://doi.org/10.1029/2007GL032011>
- 1349 Botter, G., Porporato, A., Rodriguez-Iturbe, I., & Rinaldo, A. (2009). Nonlinear storage-discharge relations and  
1350 catchment streamflow regimes: STREAMFLOW REGIMES OF NONLINEAR CATCHMENT. *Water*  
1351 *Resources Research*, *45*(10). <https://doi.org/10.1029/2008WR007658>
- 1352 Braun, J., & Yamato, P. (2010). Structural evolution of a three-dimensional, finite-width crustal wedge.  
1353 *Tectonophysics*, *484*, 181–192.
- 1354 Campbell, L. S., & Steenburgh, W. J. (2014). Finescale Orographic Precipitation Variability and Gap-Filling Radar  
1355 Potential in Little Cottonwood Canyon, Utah. *Weather and Forecasting*, *29*(4), 912–935.  
1356 <https://doi.org/10.1175/WAF-D-13-00129.1>
- 1357 Campforts, B., Vanacker, V., Herman, F., Vanmaercke, M., Schwanghart, W., Tenorio, G. E., et al. (2020).  
1358 Parameterization of river incision models requires accounting for environmental heterogeneity: insights  
1359 from the tropical Andes. *Earth Surface Dynamics*, *8*(2), 447–470. <https://doi.org/10.5194/esurf-8-447-2020>
- 1360 Cosma, S., Richard, E., & Miniscloux, F. (2002). The role of small-scale orographic features in the spatial  
1361 distribution of precipitation. *Quarterly Journal of the Royal Meteorological Society*, *128*(579), 75–92.  
1362 <https://doi.org/10.1256/00359000260498798>
- 1363 Coulthard, T. J., & Skinner, C. J. (2016). The sensitivity of landscape evolution models to spatial and  
1364 temporalrainfall resolution. *Earth Surface Dynamics*, *4*(3), 757–771. [https://doi.org/10.5194/esurf-4-757-](https://doi.org/10.5194/esurf-4-757-2016)  
1365 [2016](https://doi.org/10.5194/esurf-4-757-2016)
- 1366 Crosby, B. T., & Whipple, K. X. (2006). Knickpoint initiation and distribution within fluvial networks: 236  
1367 waterfalls in the Waipaoa River, North Island, New Zealand. *Geomorphology*, *82*, 16–38.
- 1368 Cruz, F. W., Burns, S. J., Karmann, I., Sharp, W. D., Vuille, M., Cardoso, A. O., et al. (2005). Insolation-driven  
1369 changes in atmospheric circulation over the past 116,000 years in subtropical Brazil. *Nature*, *434*(7029),  
1370 63–66. <https://doi.org/10.1038/nature03365>

- 1371 Cyr, A. J., Granger, D. E., Olivetti, V., & Molin, P. (2010). Quantifying rock uplift rates using channel steepness  
1372 and cosmogenic nuclide-determined erosion rates: Examples from northern and southern Italy. *Lithosphere*,  
1373 2(3), 188–198.
- 1374 Deal, E., Braun, J., & Botter, G. (2018). Understanding the Role of Rainfall and Hydrology in Determining Fluvial  
1375 Erosion Efficiency. *Journal of Geophysical Research: Earth Surface*, 123(4), 744–778.  
1376 <https://doi.org/10.1002/2017JF004393>
- 1377 Desormeaux, C., Godard, V., Lague, D., Duclaux, G., Fleury, J., Benedetti, L., et al. (2022). Investigation of  
1378 stochastic-threshold incision models across a climatic and morphological gradient. *Earth Surface*  
1379 *Dynamics*, 10(3), 473–492. <https://doi.org/10.5194/esurf-10-473-2022>
- 1380 DiBiase, R. A., & Whipple, K. X. (2011). The influence of erosion thresholds and runoff variability on the  
1381 relationships among topography, climate, and erosion rate. *Journal of Geophysical Research*, 116(F04036).  
1382 <https://doi.org/10.1029/2011JF002095>
- 1383 DiBiase, R. A., Whipple, K. X., Heimsath, A. M., & Ouimet, W. B. (2010). Landscape form and millennial erosion  
1384 rates in the San Gabriel Mountains, CA. *Earth and Planetary Science Letters*, 289(1–2), 134–144.
- 1385 Döll, P., Kaspar, F., & Lehner, B. (2003). A global hydrological model for deriving water availability indicators:  
1386 model tuning and validation. *Journal of Hydrology*, 270(1–2), 105–134. [https://doi.org/10.1016/S0022-](https://doi.org/10.1016/S0022-1694(02)00283-4)  
1387 [1694\(02\)00283-4](https://doi.org/10.1016/S0022-1694(02)00283-4)
- 1388 Dunne, T., & Black, R. D. (1970). Partial Area Contributions to Storm Runoff in a Small New England Watershed.  
1389 *Water Resources Research*, 6(5), 1296–1311. <https://doi.org/10.1029/WR006i005p01296>
- 1390 Farr, T. G., Rosen, P. A., Caro, E., Crippen, R., Duren, R., Hensley, S., et al. (2007). The shuttle radar topography  
1391 mission. *Reviews of Geophysics*, 45, 1–33.
- 1392 Ferrier, K. L., Huppert, K. L., & Perron, J. T. (2013). Climatic control of bedrock river incision. *Nature*, 496(7444),  
1393 206–209. <https://doi.org/10.1038/nature11982>
- 1394 Flint, J. J. (1974). Stream gradient as a function of order, magnitude, and discharge. *Water Resources Research*, 10,  
1395 969–973.
- 1396 Forte, A. M. (2024, January). amforte/snowmelt\_orography: Snowmelt Orography (Version v2.0). Zenodo.  
1397 <https://doi.org/10.5281/zenodo.10449397>

- 1398 Forte, A. M., & Rossi, M. W. (2024a). Data and Model Results Associated with Stochastic in Space and Time: Parts  
1399 1 and 2. (Version 2.0) [Data set]. <https://doi.org/10.5281/zenodo.10407347>
- 1400 Forte, A. M., & Rossi, M. W. (2024b). Stochastic in space and time: Part 1, Characterizing Orographic Gradients in  
1401 Mean Runoff and Daily Runoff Variability. *Journal of Geophysical Research F: Earth Surface*.  
1402 <https://doi.org/10.1029/2023JF007326>
- 1403 Forte, A. M., & Whipple, K. X. (2019). Short communication : The Topographic Analysis Kit (TAK) for  
1404 TopoToolbox. *Earth Surface Dynamics*, 7, 87–95. <https://doi.org/10.5194/esurf-7-87-2019>
- 1405 Forte, A. M., Whipple, K. X., Bookhagen, B., & Rossi, M. W. (2016). Decoupling of modern shortening rates,  
1406 climate, and topography in the Caucasus. *Earth and Planetary Science Letters*, 449, 282–294.  
1407 <https://doi.org/10.1016/j.epsl.2016.06.013>
- 1408 Forte, A. M., Leonard, J. S., Rossi, M. W., Whipple, K. X., Heimsath, A. M., Sukhishvili, L., et al. (2022). Low  
1409 variability runoff inhibits coupling of climate, tectonics, and topography in the Greater Caucasus. *Earth  
1410 and Planetary Science Letters*, 584. <https://doi.org/10.1016/j.epsl.2022.117525>
- 1411 Frei, C., & Schär, C. (1998). A precipitation climatology of the Alps from high-resolution rain-gauge observations.  
1412 *International Journal of Climatology*, 18(8), 873–900. [https://doi.org/10.1002/\(SICI\)1097-  
1413 0088\(19980630\)18:8<873::AID-JOC255>3.0.CO;2-9](https://doi.org/10.1002/(SICI)1097-0088(19980630)18:8<873::AID-JOC255>3.0.CO;2-9)
- 1414 Gallen, S. F., & Fernández-Blanco, D. (2021). A New Data-driven Bayesian Inversion of Fluvial Topography  
1415 Clarifies the Tectonic History of the Corinth Rift and Reveals a Channel Steepness Threshold. *Journal of  
1416 Geophysical Research: Earth Surface*. <https://doi.org/10.1029/2020JF005651>
- 1417 Garvert, M. F., Smull, B., & Mass, C. (2007). Multiscale Mountain Waves Influencing a Major Orographic  
1418 Precipitation Event. *Journal of the Atmospheric Sciences*, 64(3), 711–737.  
1419 <https://doi.org/10.1175/JAS3876.1>
- 1420 Gasparini, N. M., & Brandon, M. T. (2011). A generalized power law approximation for fluvial incision of bedrock  
1421 channels. *Journal of Geophysical Research: Earth Surface*, 116(F2). <https://doi.org/10.1029/2009JF001655>
- 1422 Godard, V., Tucker, G. E., Fisher, G. B., Burbank, D. W., & Bookhagen, B. (2013). Frequency-dependent landscape  
1423 response to climatic forcing. *Geophysical Research Letters*, 40, 859–863. <https://doi.org/10.1002/grl.50253>
- 1424 Hack, J. T. (1957). *Studies of longitudinal stream profiles in Virginia and Maryland* (pp. 97–97).

- 1425 Han, J., Gasparini, N. M., & Johnson, J. P. L. (2015). Measuring the imprint of orographic rainfall gradients on the  
1426 morphology of steady-state numerical fluvial landscapes: OROGRAPHIC RAINFALL AND STEADY-  
1427 STATE FLUVIAL LANDSCAPES. *Earth Surface Processes and Landforms*, 40(10), 1334–1350.  
1428 <https://doi.org/10.1002/esp.3723>
- 1429 Harel, M. A., Mudd, S. M., & Attal, M. (2016). Global analysis of the stream power law parameters based on  
1430 worldwide <sup>10</sup>Be denudation rates. *Geomorphology*, 268, 184–196.  
1431 <https://doi.org/10.1016/j.geomorph.2016.05.035>
- 1432 Harkins, N., Kirby, E., Heimsath, A. M., Robinson, R., & Reiser, U. (2007). Transient fluvial incision in the  
1433 headwaters of the Yellow River, northeastern Tibet, China. *Journal of Geophysical Research*, 112,  
1434 F03S04-F03S04.
- 1435 Hilley, G. E., Porder, S., Aron, F., Baden, C. W., Johnstone, S. A., Liu, F., et al. (2019). Earth's topographic relief  
1436 potentially limited by an upper bound on channel steepness. *Nature Geoscience*, 12(10), 828–832.  
1437 <https://doi.org/10.1038/s41561-019-0442-3>
- 1438 Hopley, D. E. J., Adams, J. M., Nudurupati, S. S., Hutton, E. W. H., Gasparini, N. M., Istanbuloglu, E., & Tucker,  
1439 G. E. (2017). Creative computing with Landlab: an open-source toolkit for building, coupling, and  
1440 exploring two-dimensional numerical models of Earth-surface dynamics. *Earth Surface Dynamics*, 5(1),  
1441 21–46. <https://doi.org/10.5194/esurf-5-21-2017>
- 1442 Howard, A. D. (1994). A detachment-limited model of drainage basin evolution. *Water Resources Research*, 30(7),  
1443 2261–2285.
- 1444 Kirby, E., & Whipple, K. X. (2012). Expression of active tectonics in erosional landscapes. *Journal of Structural*  
1445 *Geology*, 44, 54–75.
- 1446 Lague, D. (2014). The stream power river incision model: evidence, theory and beyond. *Earth Surface Processes*  
1447 *and Landforms*, 39(1), 38–61. <https://doi.org/10.1002/esp.3462>
- 1448 Lague, D., Hovius, N., & Davy, P. (2005). Discharge, discharge variability, and the bedrock channel profile. *Journal*  
1449 *of Geophysical Research*, 110, F04006–F04006. <https://doi.org/10.1029/2004JF000259>
- 1450 Lehner, B., Verdin, K., & Jarvis, A. (2008). New Global Hydrography Derived From Spaceborne Elevation Data.  
1451 *Eos, Transactions American Geophysical Union*, 89(10), 93. <https://doi.org/10.1029/2008EO100001>

- 1452 Leonard, J. S., Whipple, K. X., & Heimsath, A. M. (2023a). Controls on topography and erosion of the north-central  
1453 Andes. *Geology*. <https://doi.org/10.1130/G51618.1>
- 1454 Leonard, J. S., Whipple, K. X., & Heimsath, A. M. (2023b). Isolating climatic, tectonic, and lithologic controls on  
1455 mountain landscape evolution. *Science Advances*, *9*(3), eadd8915. <https://doi.org/10.1126/sciadv.add8915>
- 1456 Marder, E., & Gallen, S. F. (2023). Climate control on the relationship between erosion rate and fluvial topography.  
1457 *Geology*. <https://doi.org/10.1130/G50832.1>
- 1458 Marra, F., Armon, M., & Morin, E. (2022). Coastal and orographic effects on extreme precipitation revealed by  
1459 weather radar observations. *Hydrology and Earth System Sciences*, *26*(5), 1439–1458.  
1460 <https://doi.org/10.5194/hess-26-1439-2022>
- 1461 Miller, S. R., Sak, P. B., Kirby, E., & Bierman, P. R. (2013). Neogene rejuvenation of central Appalachian  
1462 topography: Evidence for differential rock uplift from stream profiles and erosion rates. *Earth and*  
1463 *Planetary Science Letters*, *369*, 1–12.
- 1464 Minder, J. R., Durran, D. R., Roe, G. H., & Anders, A. M. (2008). The climatology of small-scale orographic  
1465 precipitation over the Olympic Mountains: Patterns and processes. *Quarterly Journal of the Royal*  
1466 *Meteorological Society*, *134*(633), 817–839. <https://doi.org/10.1002/qj.258>
- 1467 Molnar, P., Anderson, R. S., Kier, G., & Rose, J. (2006). Relationships among probability distributions of stream  
1468 discharges in floods, climate, bed load transport, and river incision. *Journal of Geophysical Research*, *111*,  
1469 F02001–F02001. <https://doi.org/10.1029/2005JF000310>
- 1470 Montgomery, D. R., & Brandon, M. T. (2002). Topographic controls on erosion rates in tectonically active mountain  
1471 ranges. *Earth and Planetary Science Letters*, *201*, 481–489.
- 1472 Olivetti, V., Cyr, A. J., Molin, P., Faccenna, C., & Granger, D. E. (2012). Uplift history of the Sila Massif, southern  
1473 Italy, deciphered from cosmogenic Be-10 erosion rates and river longitudinal profile analysis. *Tectonics*,  
1474 *31*, TC3007–TC3007. <https://doi.org/10.1029/2011TC003037>
- 1475 Ouimet, W. B., Whipple, K. X., & Granger, D. E. (2009). Beyond threshold hillslopes: Channel adjustment to base-  
1476 level fall in tectonically active mountain ranges. *Geology*, *37*(7), 579–582.
- 1477 Peleg, N., Skinner, C., Ramirez, J. A., & Molnar, P. (2021). Rainfall spatial-heterogeneity accelerates landscape  
1478 evolution processes. *Geomorphology*, *390*, 107863. <https://doi.org/10.1016/j.geomorph.2021.107863>

- 1479 Perron, J. T., & Royden, L. H. (2013). An integral approach to bedrock river profile analysis. *Earth Surface*  
1480 *Processes and Landforms*, 38, 570–576. <https://doi.org/10.1002/esp.3302>
- 1481 Pitlick, J. (1994). Relation between peak flows, precipitation, and physiography for five mountain regions in the  
1482 western USA. *Journal of Hydrology*, 158, 219–240.
- 1483 Roe, G. H. (2005). OROGRAPHIC PRECIPITATION. *Annual Review of Earth and Planetary Sciences*, 33(1), 645–  
1484 671. <https://doi.org/10.1146/annurev.earth.33.092203.122541>
- 1485 Roe, G. H., Montgomery, D. R., & Hallet, B. (2002). Effects of orographic precipitation variations on the concavity  
1486 of steady-state river profiles. *Geology*, 30(2), 143–146.
- 1487 Roe, G. H., Montgomery, D. R., & Hallet, B. (2003). Orographic precipitation and the relief of mountain ranges.  
1488 *Journal of Geophysical Research*, 108(B6). <https://doi.org/10.1029/2001JB001521>
- 1489 Roe, G. H., Stolar, D. B., & Willett, S. D. (2006). Response of a steady-state critical wedge orogen to changes in  
1490 climate and tectonic forcing. In S. D. Willett, N. Hovius, M. T. Brandon, & D. Fisher (Eds.), *Tectonics,*  
1491 *climate, and landscape evolution* (Vols. 1–398, pp. 239–272).
- 1492 Rosenbloom, N., & Anderson, R. S. (1994). Hillslope and channel evolution in a marine terraced landscape, Santa  
1493 Cruz, California. *Journal of Geophysical Research*, 99(B7), 14013–14029.
- 1494 Rossi, M. W., Whipple, K. X., & Vivoni, E. R. (2016). Precipitation and evapotranspiration controls on event-scale  
1495 runoff variability in the contiguous United States and Puerto Rico. *Journal of Geophysical Research*, 121.  
1496 <https://doi.org/10.1002/2015JF003446>
- 1497 Rossi, M. W., Quigley, M. C., Fletcher, J. M., Whipple, K. X., Díaz-torres, J. J., Seiler, C., et al. (2017). Along-  
1498 strike variation in catchment morphology and cosmogenic denudation rates reveal the pattern and history of  
1499 footwall uplift , Main Gulf Escarpment , Baja California. *Geological Society of America Bulletin*.  
1500 <https://doi.org/10.1130/B31373.1>
- 1501 Rossi, M. W., Anderson, R. S., Anderson, S. P., & Tucker, G. E. (2020). Orographic Controls on Subdaily Rainfall  
1502 Statistics and Flood Frequency in the Colorado Front Range, USA. *Geophysical Research Letters*, 47(4).  
1503 <https://doi.org/10.1029/2019GL085086>
- 1504 Safran, E. B., Bierman, P. R., Aalto, R., Dunne, T., Whipple, K. X., & Caffee, M. W. (2005). Erosion rates driven  
1505 by channel network incision in the Bolivian Andes. *Earth Surface Processes and Landforms*, 30, 1007–  
1506 1024.

- 1507 Sassolas-Serrayet, T., Cattin, R., & Ferry, M. (2018). The shape of watersheds. *Nature Communications*, 9(1), 1–8.  
1508 <https://doi.org/10.1038/s41467-018-06210-4>
- 1509 Schaefli, B., Rinaldo, A., & Botter, G. (2013). Analytic probability distributions for snow-dominated streamflow:  
1510 Snow-Dominated Streamflow Pdfs. *Water Resources Research*, 49(5), 2701–2713.  
1511 <https://doi.org/10.1002/wrcr.20234>
- 1512 Scherler, D., Bookhagen, B., & Strecker, M. R. (2014). Tectonic control on 10 Be-derived erosion rates in the  
1513 Garhwal. *Journal of Geophysical Research: Earth Surface*, 119(August 2013), 83–105.  
1514 <https://doi.org/10.1002/2013JF002955>
- 1515 Scherler, D., DiBiase, R. A., Fisher, G. B., & Avouac, J.-P. (2017). Testing monsoonal controls on bedrock river  
1516 incision in the Himalaya and Eastern Tibet with a stochastic-threshold stream power model. *Journal of*  
1517 *Geophysical Research: Earth Surface*, 122, 1389–1429. <https://doi.org/10.1002/2016JF004011>
- 1518 Schmidt, K. M., & Montgomery, D. R. (1995). Limits to relief. *Science*, 270(5236), 617–620.
- 1519 Schwanghart, W., & Scherler, D. (2014). Short Communication: TopoToolbox 2 - MATLAB based software for  
1520 topographic analysis and modeling in Earth surface sciences. *Earth Surface Dynamics*, 2, 1–7.  
1521 <https://doi.org/10.5194/esurf-2-1-2014>
- 1522 Shen, H., Lynch, B., Poulsen, C. J., & Yanites, B. J. (2021). A modeling framework (WRF-Landlab) for simulating  
1523 orogen-scale climate-erosion coupling. *Computers & Geosciences*, 146, 104625.  
1524 <https://doi.org/10.1016/j.cageo.2020.104625>
- 1525 Shobe, C. M., Tucker, G. E., & Rossi, M. W. (2018). Variable-Threshold Behavior in Rivers Arising From  
1526 Hillslope-Derived Blocks. *Journal of Geophysical Research: Earth Surface*, 123(8), 1931–1957.  
1527 <https://doi.org/10.1029/2017JF004575>
- 1528 Snyder, N. P., Whipple, K. X., Tucker, G. E., & Merritts, D. J. (2003). Importance of a stochastic distribution of  
1529 floods and erosion thresholds in the bedrock river incision problem. *Journal of Geophysical Research*,  
1530 108(B2). <https://doi.org/10.1029/2001JB001655>
- 1531 Stolar, D. B., Roe, G. H., & Willett, S. D. (2007). Controls on the patterns of topography and erosion rate in a  
1532 critical orogen. *Journal of Geophysical Research*, 112(F04002). <https://doi.org/10.1029/2006JF000713>

- 1533 Tucker, G. E. (2004). Drainage basin sensitivity to tectonic and climatic forcing: Implications of a stochastic model  
1534 for the role of entrainment and erosion thresholds. *Earth Surface Processes and Landforms*, 29, 185–204.  
1535 <https://doi.org/10.1002/esp.1020>
- 1536 Tucker, G. E., & Bras, R. L. (2000). A stochastic approach to modeling the role of rainfall variability in drainage  
1537 basin evolution. *Water Resources Research*, 36(7), 1953–1964.
- 1538 Wang, Y., Cheng, H., Edwards, R. L., Kong, X., Shao, X., Chen, S., et al. (2008). Millennial- and orbital-scale  
1539 changes in the East Asian monsoon over the past 224,000 years. *Nature*, 451(7182), 1090–1093.  
1540 <https://doi.org/10.1038/nature06692>
- 1541 Whipple, K. X. (2001). Fluvial landscape response time: How plausible is steady-state denudation? *American*  
1542 *Journal of Science*, 301, 313–325.
- 1543 Whipple, K. X. (2009). The influence of climate on the tectonic evolution of mountain belts. *Nature Geoscience*, 2,  
1544 97–104.
- 1545 Whipple, K. X., & Meade, B. (2004). Controls on the strength of coupling among climate, erosion, and deformation  
1546 in two-sided, frictional orogenic wedges at steady state. *Journal of Geophysical Research*, 109, F01011–  
1547 F01011. <https://doi.org/10.1029/2003JF000019>
- 1548 Whipple, K. X., & Meade, B. (2006). Orogen response to changes in climatic and tectonic forcing. *Earth and*  
1549 *Planetary Science Letters*, 243, 218–228.
- 1550 Whipple, K. X., & Tucker, G. E. (1999). Dynamics of the stream-power river incision model: Implications for  
1551 height limits of mountain ranges, landscape response timescales, and research needs. *Journal of*  
1552 *Geophysical Research*, 104(B8), 17661–17674.
- 1553 Whipple, K. X., & Tucker, G. E. (2002). Implications of sediment-flux-dependent river incision models for  
1554 landscape evolution. *Journal of Geophysical Research*, 107(B2). <https://doi.org/10.1029/2000JB000044>
- 1555 Whipple, K. X., DiBiase, R. A., Crosby, B., & Johnson, J. P. L. (2022). Bedrock Rivers. In J. (Jack) F. Shroder  
1556 (Ed.), *Treatise on Geomorphology (Second Edition)* (pp. 865–903). Oxford: Academic Press.  
1557 <https://doi.org/10.1016/B978-0-12-818234-5.00101-2>
- 1558 Willett, S. D. (1999). Orogeny and orography: The effects of erosion on the structure of mountain belts. *Journal of*  
1559 *Geophysical Research*, 104(B12), 28,957-28,981.

- 1560 Wobus, C. W., Whipple, K. X., Kirby, E., Snyder, N. P., Johnson, J., Spyropolou, K., et al. (2006). Tectonics from  
1561 topography: Procedures, promise, and pitfalls. In S. D. Willett, N. Hovius, M. T. Brandon, & D. Fisher  
1562 (Eds.), *Tectonics, climate, and landscape evolution* (Vols. 1–398, pp. 55–74). Boulder, CO: The Geological  
1563 Society of America.
- 1564 Wolman, M. G., & Miller, J. P. (1960). Magnitude and frequency of forces in geomorphic processes. *Journal of*  
1565 *Geology*, 68, 54–74.
- 1566 Yanites, B. J., Becker, J. K., Madritsch, H., Schnellmann, M., & Ehlers, T. A. (2017). Lithologic Effects on  
1567 Landscape Response to Base Level Changes: A Modeling Study in the Context of the Eastern Jura  
1568 Mountains, Switzerland. *Journal of Geophysical Research: Earth Surface*, 122(11), 2196–2222.  
1569 <https://doi.org/10.1002/2016JF004101>
- 1570

Figure 1.

— Local Relief to Runoff  
- - - Maximum Elevation to Snowmelt Fraction

— Low Snowmelt Contribution  
- - - High Snowmelt Contribution

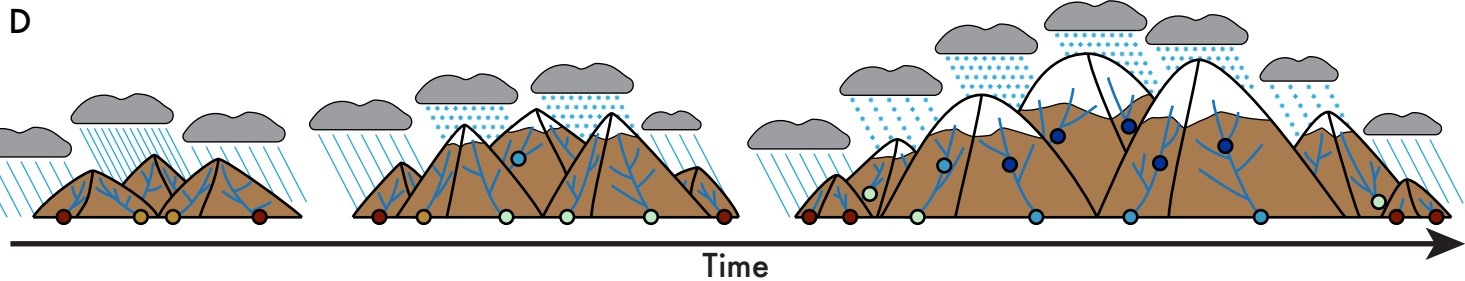
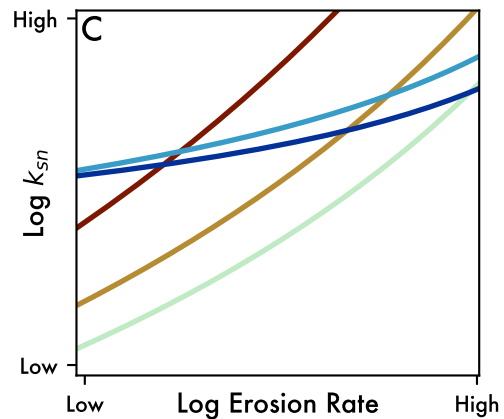
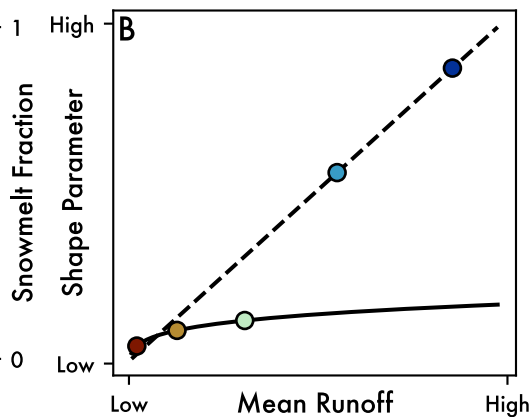
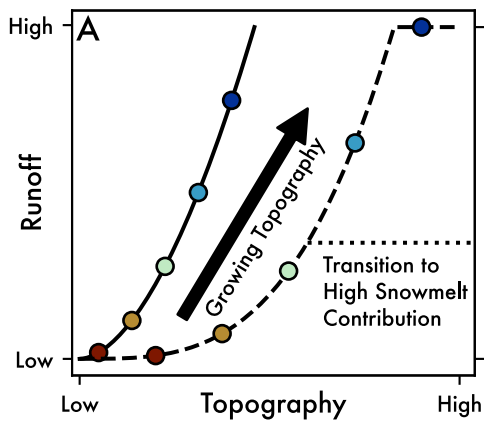


Figure 2.

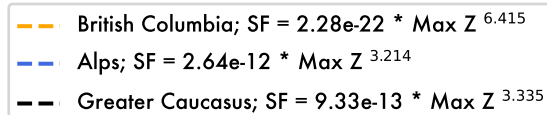
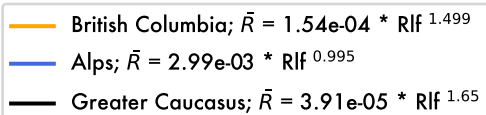
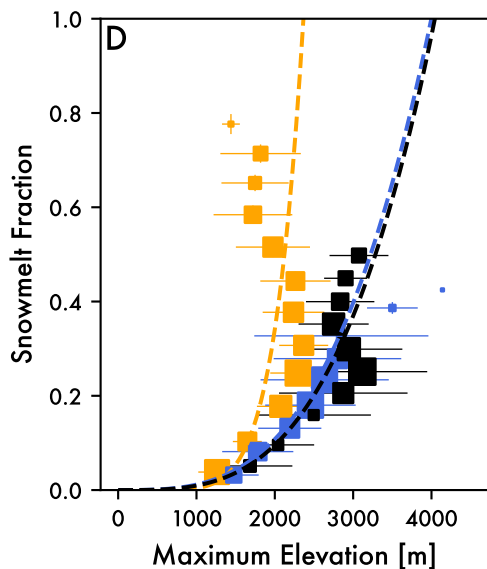
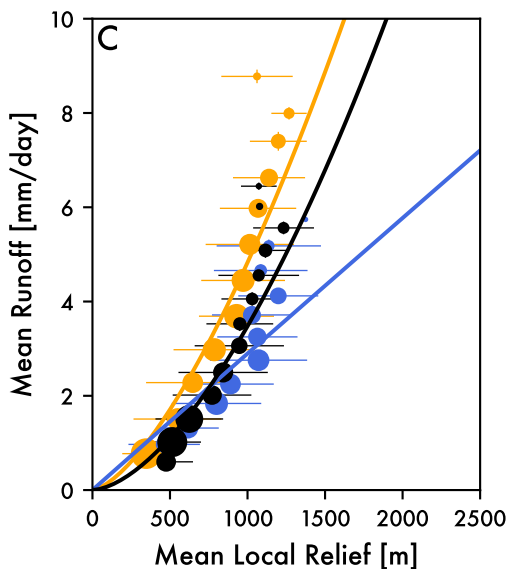
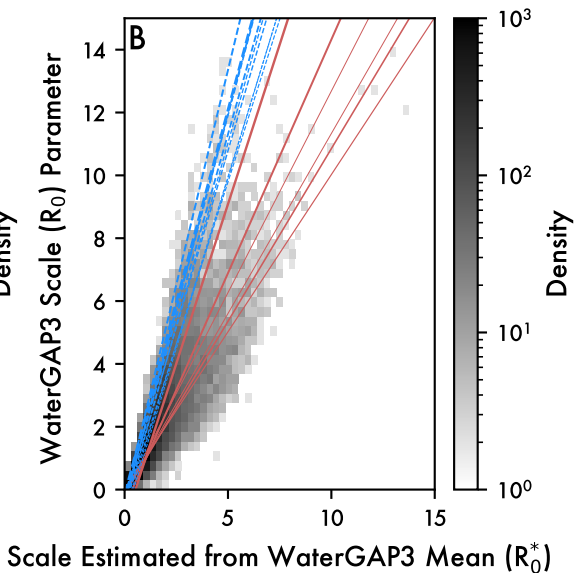
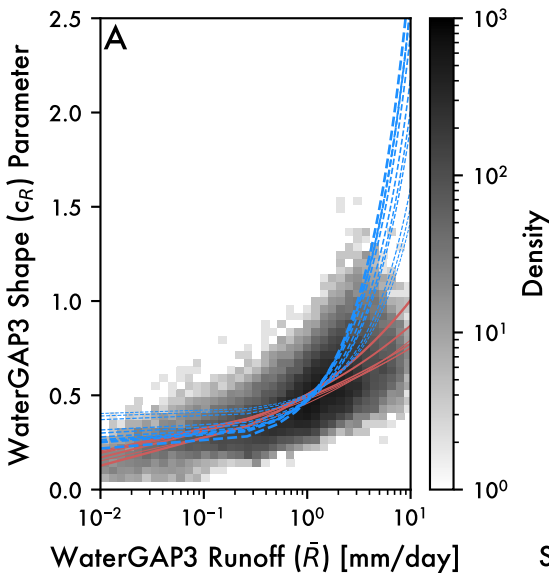
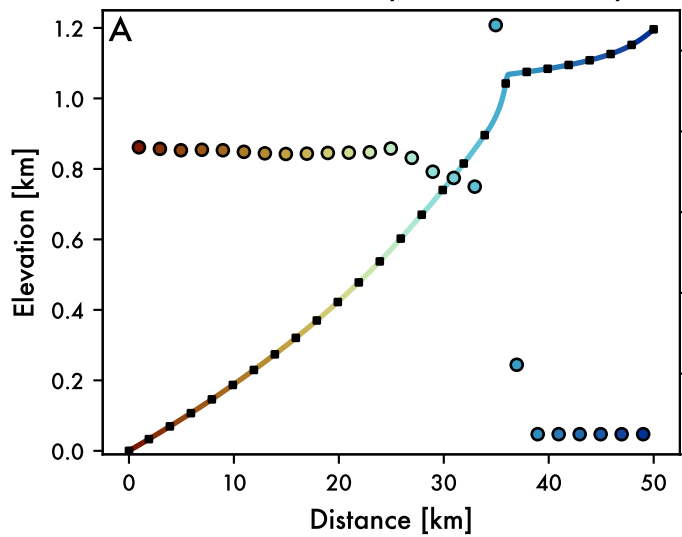


Figure 3.

GC1U : GC - 1 mm/yr - Unlinked - 1 Myr



GC1L : GC - 1 mm/yr - Linked - 0.63 Myr

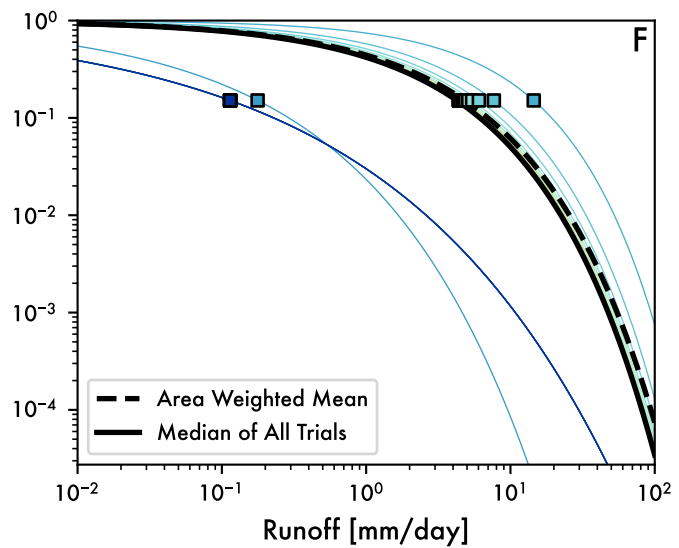
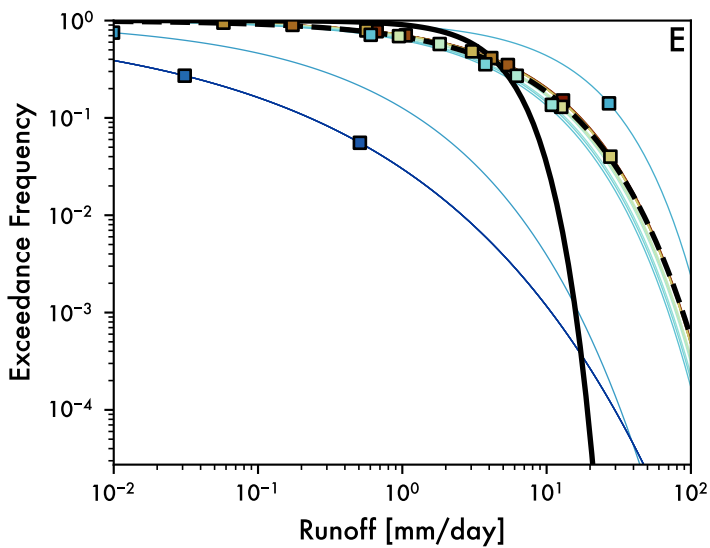
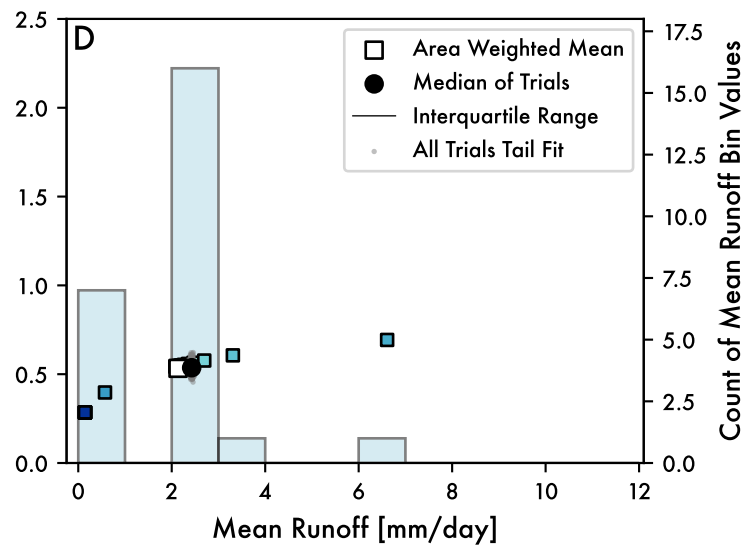
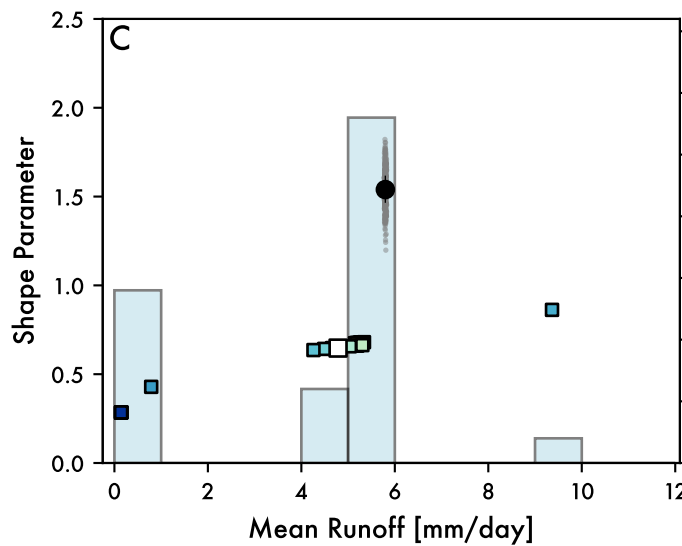
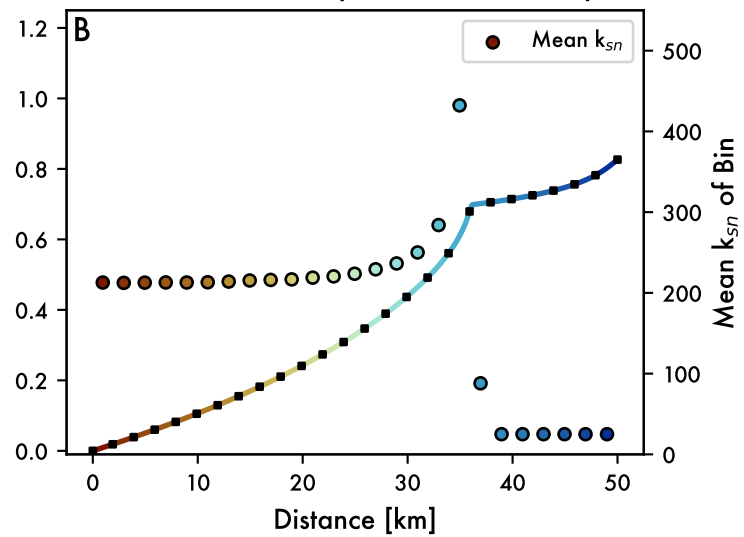


Figure 4.



Figure 5.

GC1U : GC - 1 mm/yr - Unlinked

GC1L : GC - 1 mm/yr - Linked

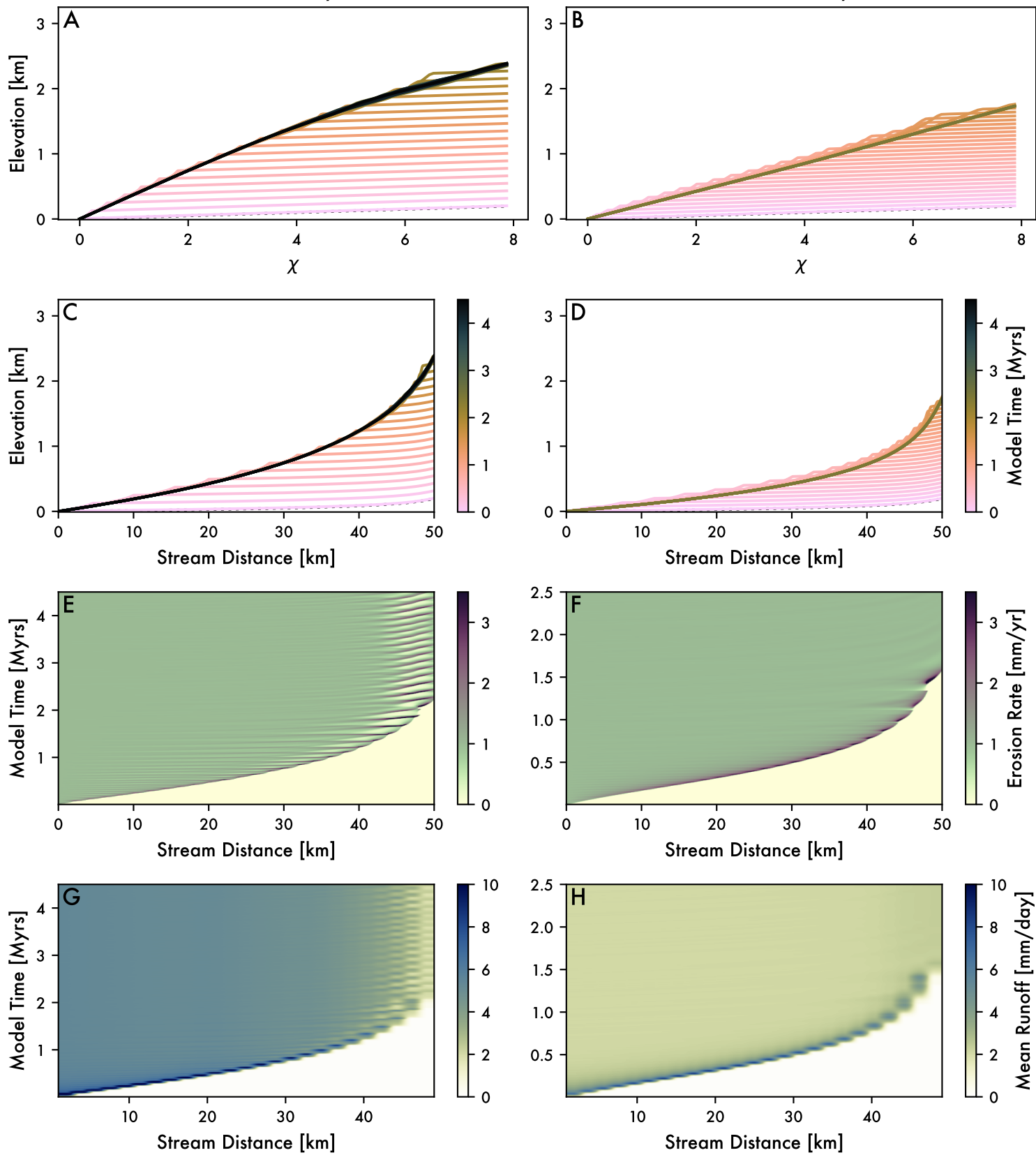
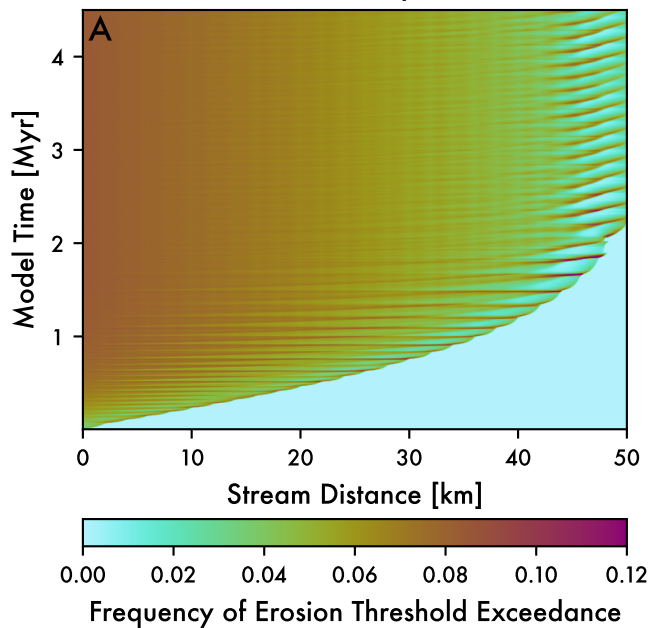


Figure 6.

GC1U : GC - 1 mm/yr - Unlinked



GC1L : GC - 1 mm/yr - Linked

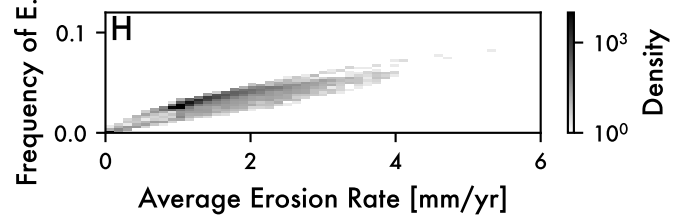
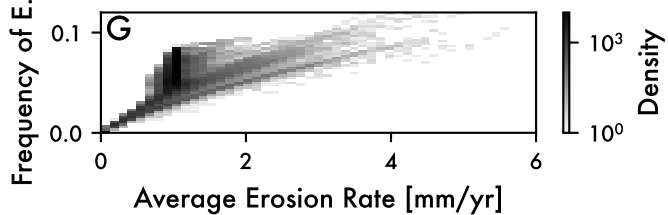
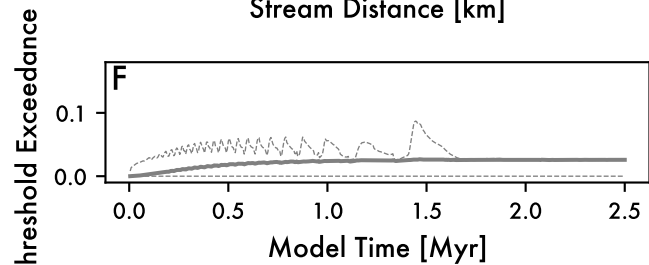
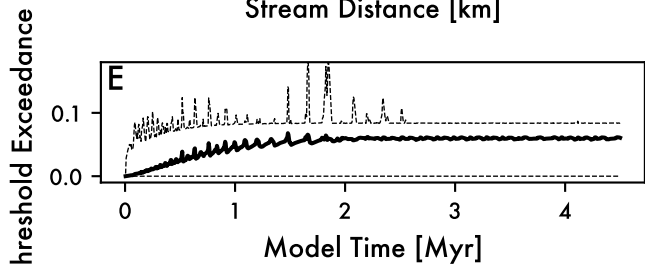
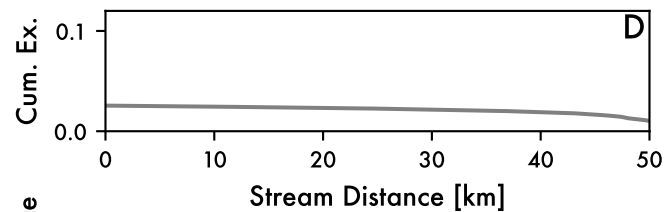
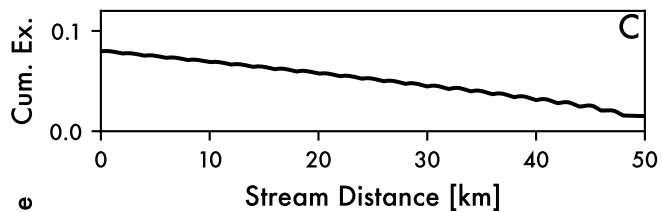
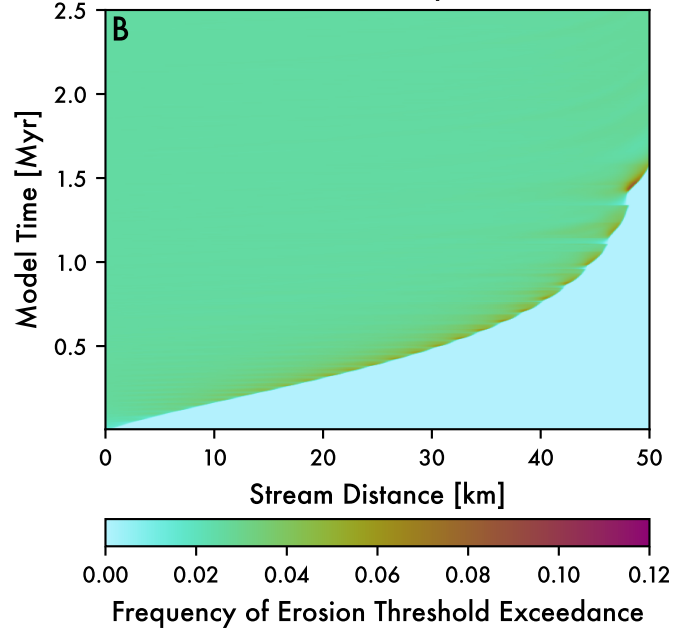
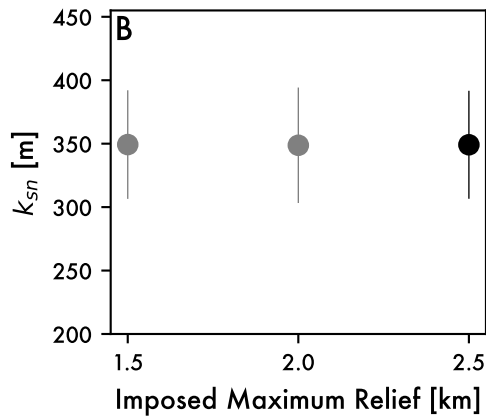
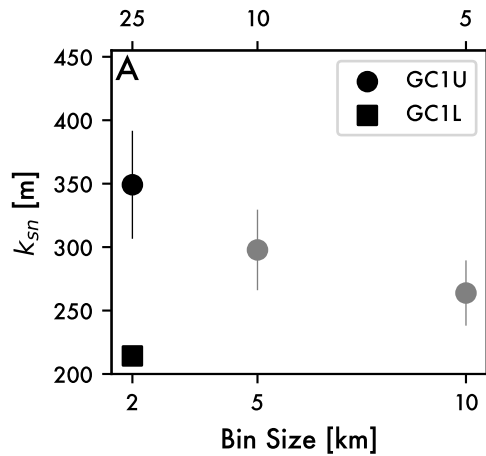


Figure 7.

Number of Bins



Number of Bins

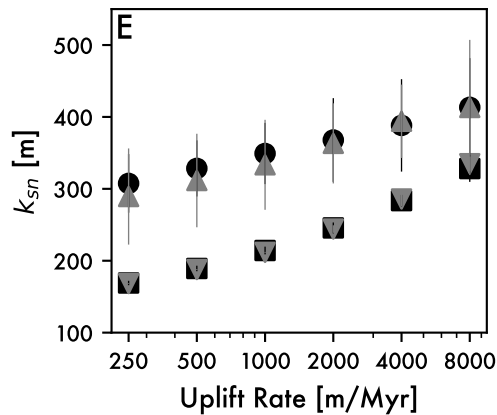
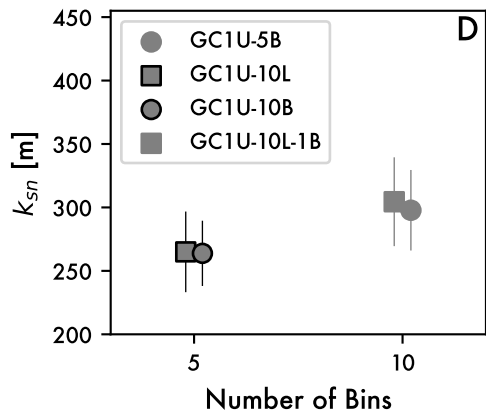
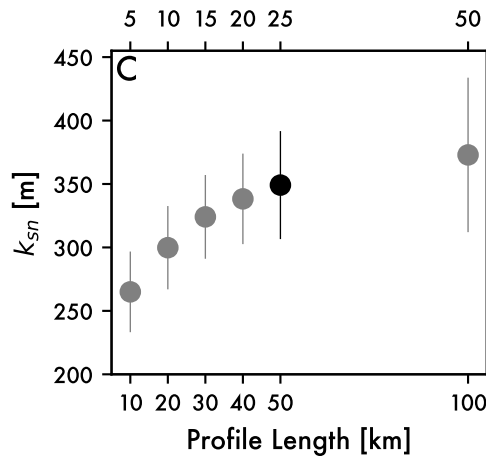


Figure 8.

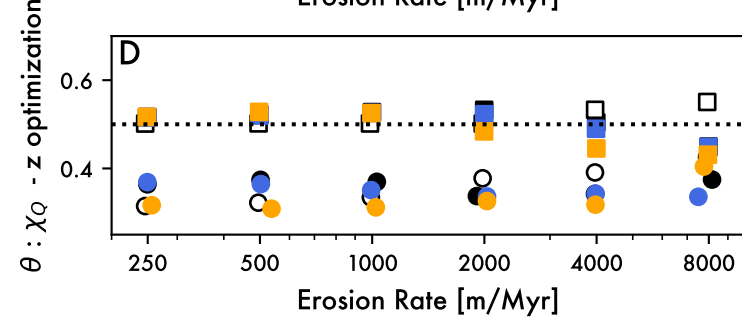
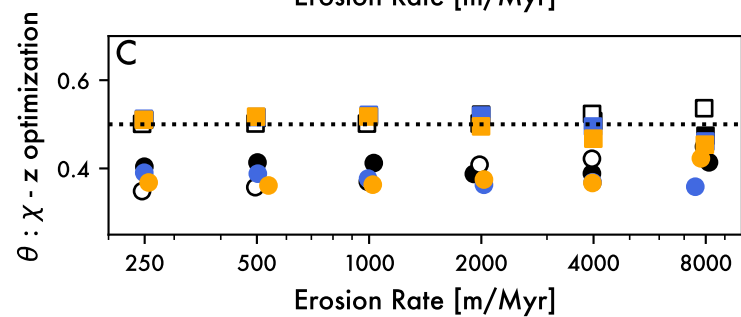
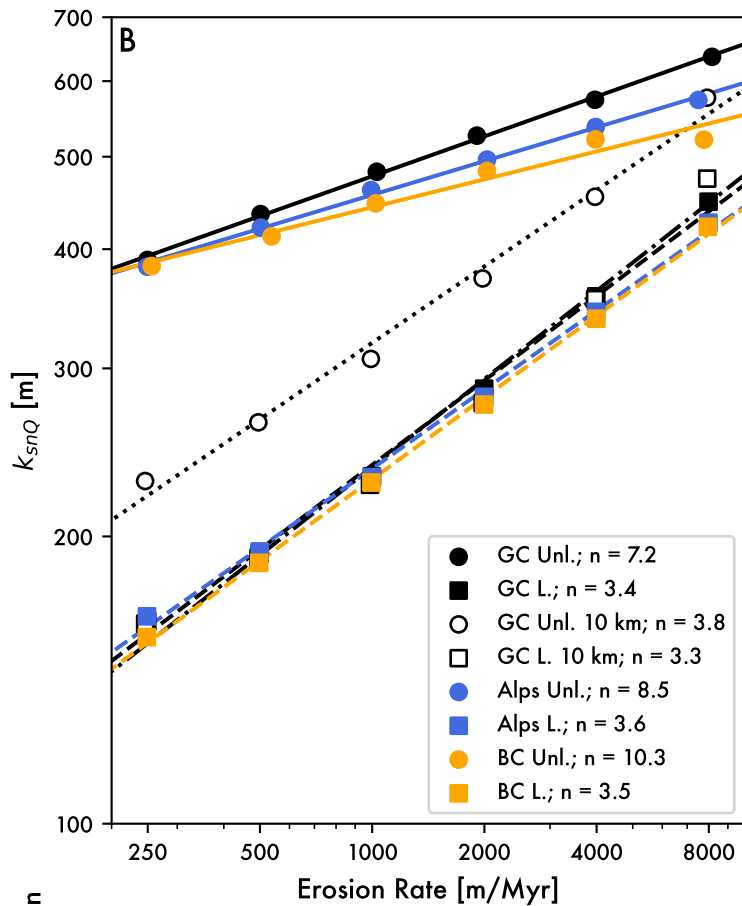
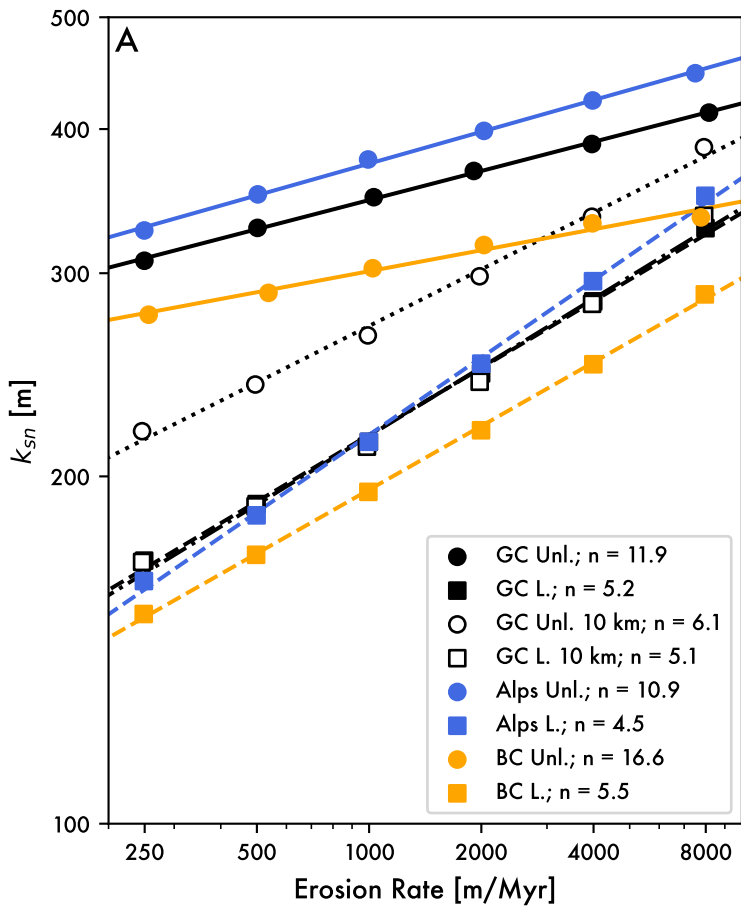


Figure 9.

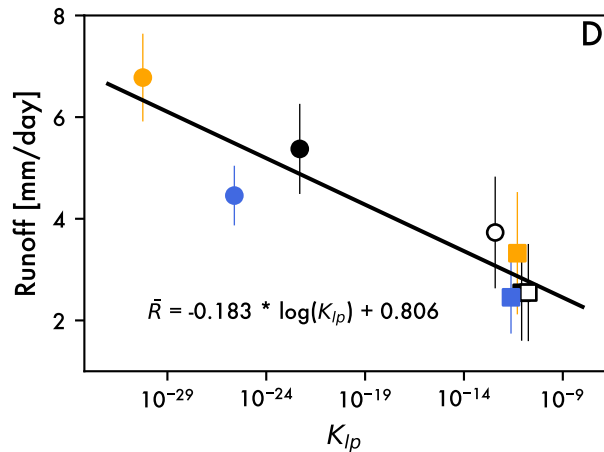
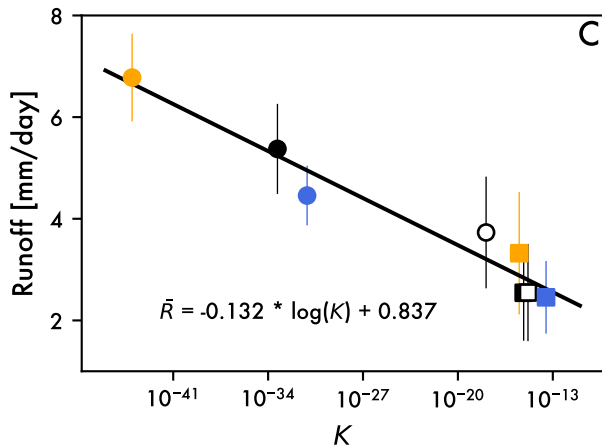
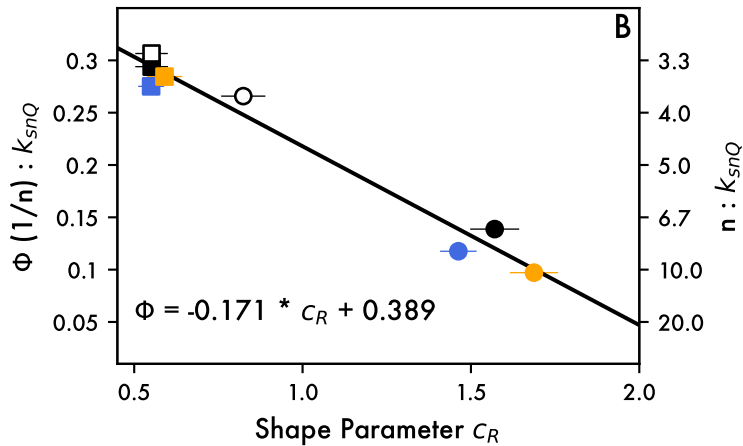
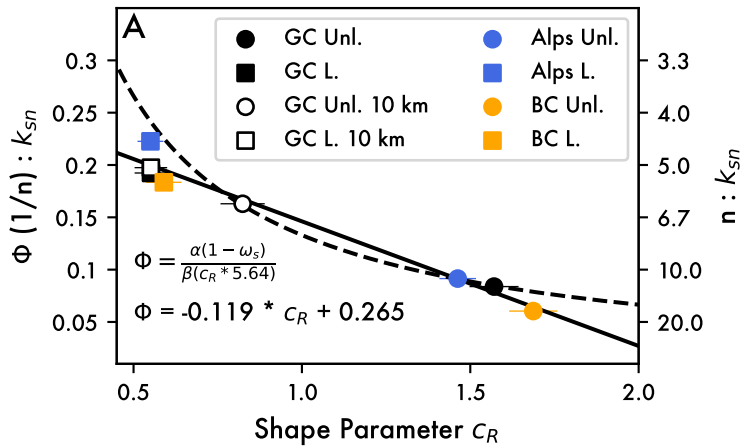
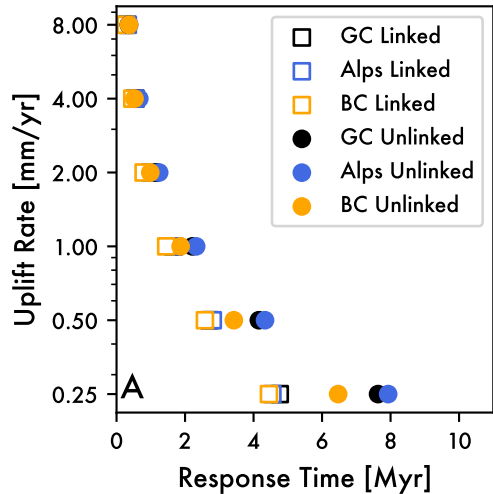
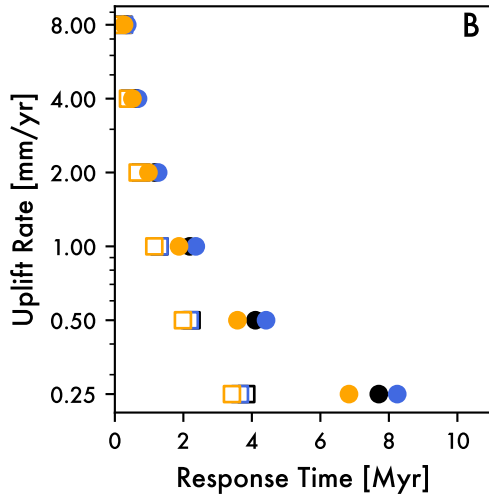


Figure 10.

$\Delta$  Maximum Elevation

Analytical Solution



Response Time

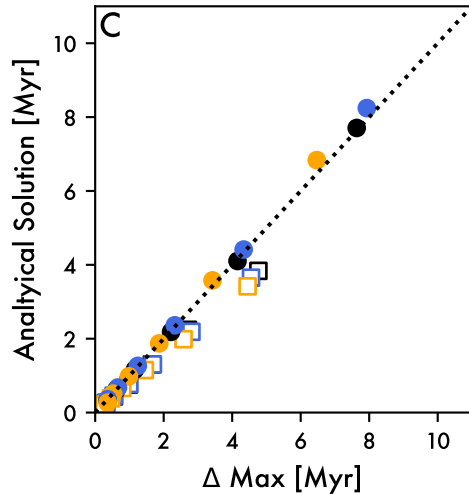


Figure 11.

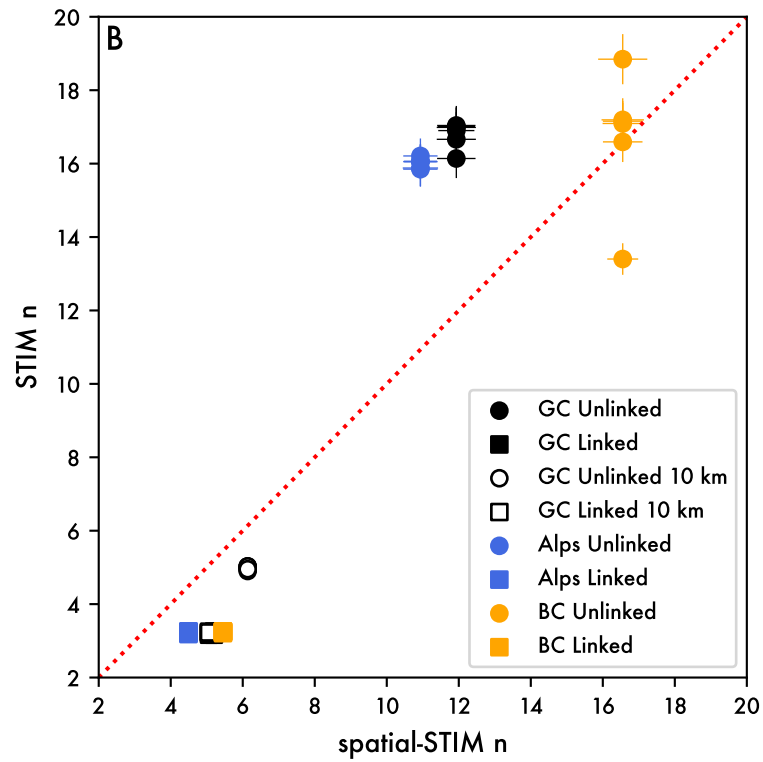
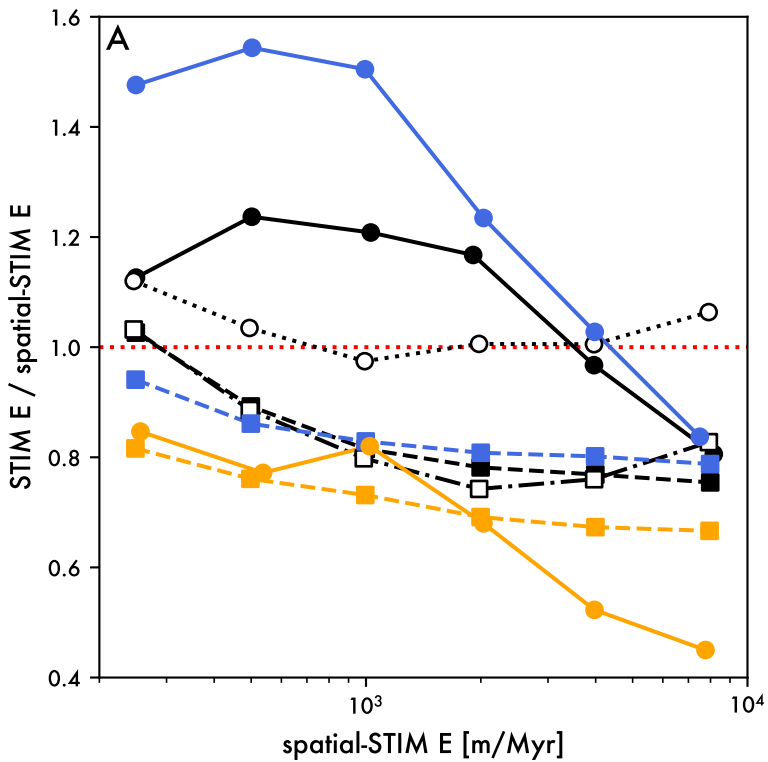
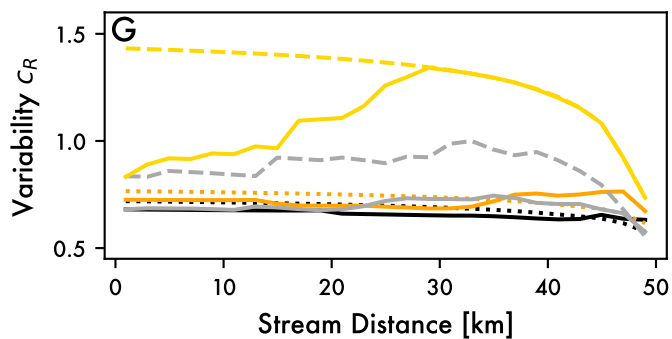
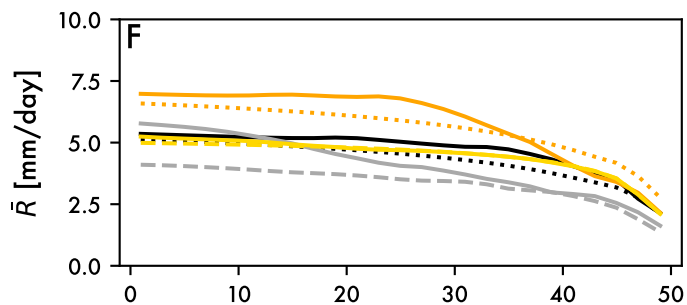
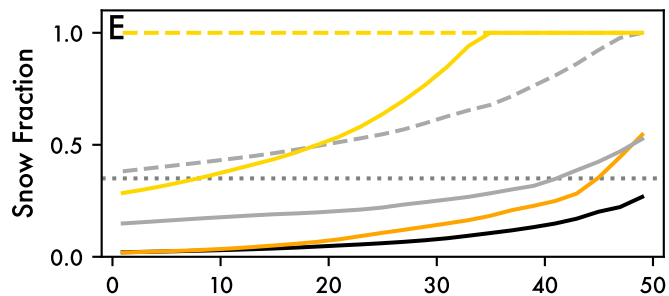
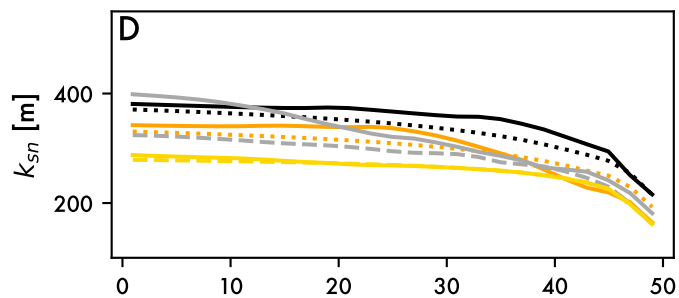
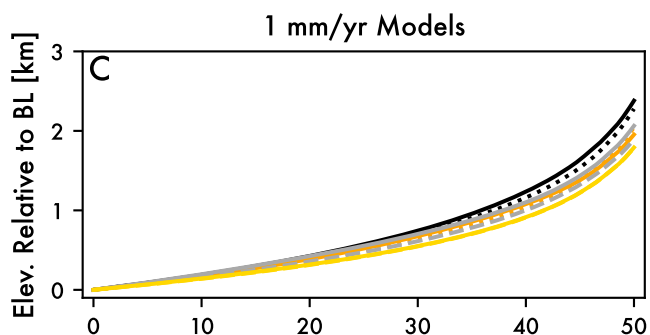
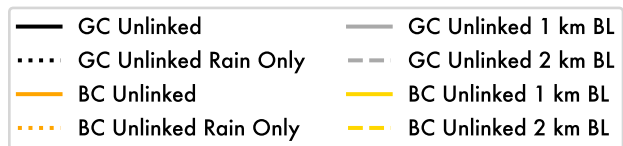
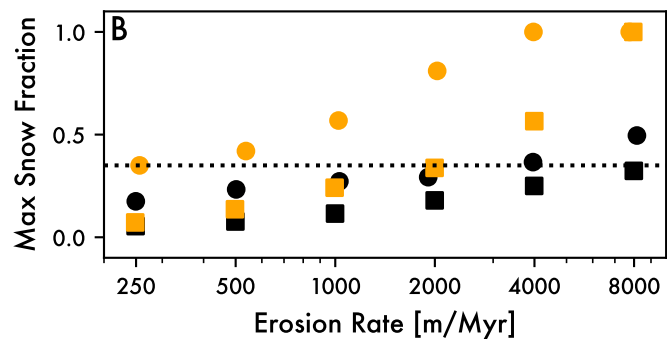
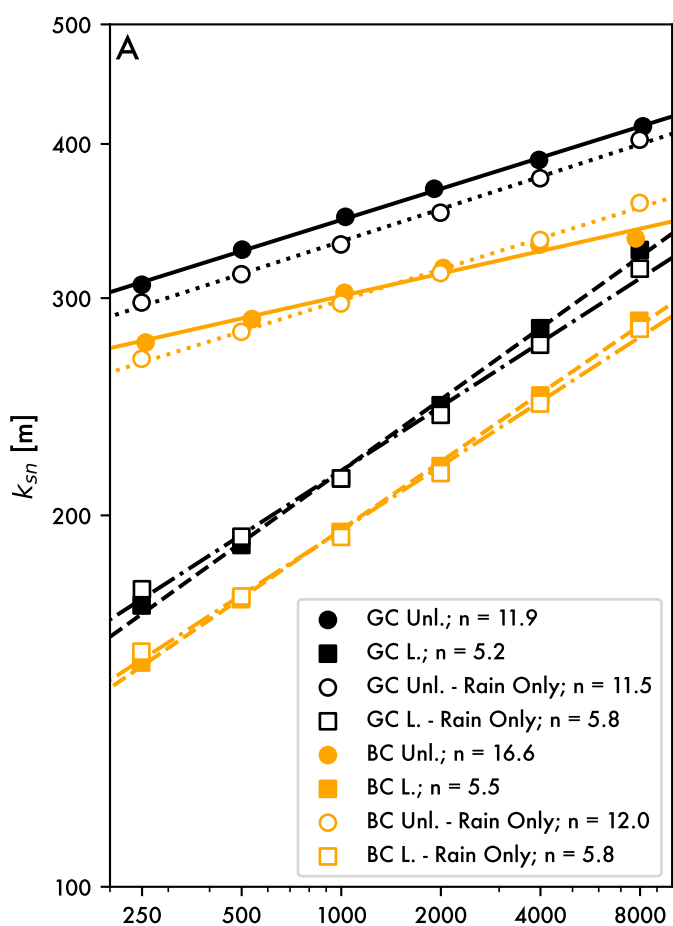


Figure 12.



Supporting Information for

**Stochastic in Space and Time: Part 2, Effects of Simulating Orographic Gradients in Daily Runoff Variability on Bedrock River Incision**

**A.M. Forte<sup>1</sup> and M.W. Rossi<sup>2</sup>**

<sup>1</sup> Department of Geology and Geophysics, Louisiana State University, Baton Rouge, Louisiana, USA.

<sup>2</sup> Earth Lab, Cooperative Institute for Research in Environmental Sciences (CIRES), University of Colorado, Boulder, Colorado, USA.

**Contents of this file**

Figures S1 to S6

Tables S1 to S2

**Introduction**

This supplemental file contains seven supplemental figures that contain additional details on model results. It also contains two tables. Table S1 are the invariant STIM parameters common to all models, whereas Table S2 highlights the values or properties that change between model runs. Table S2 is provided an Excel sheet.

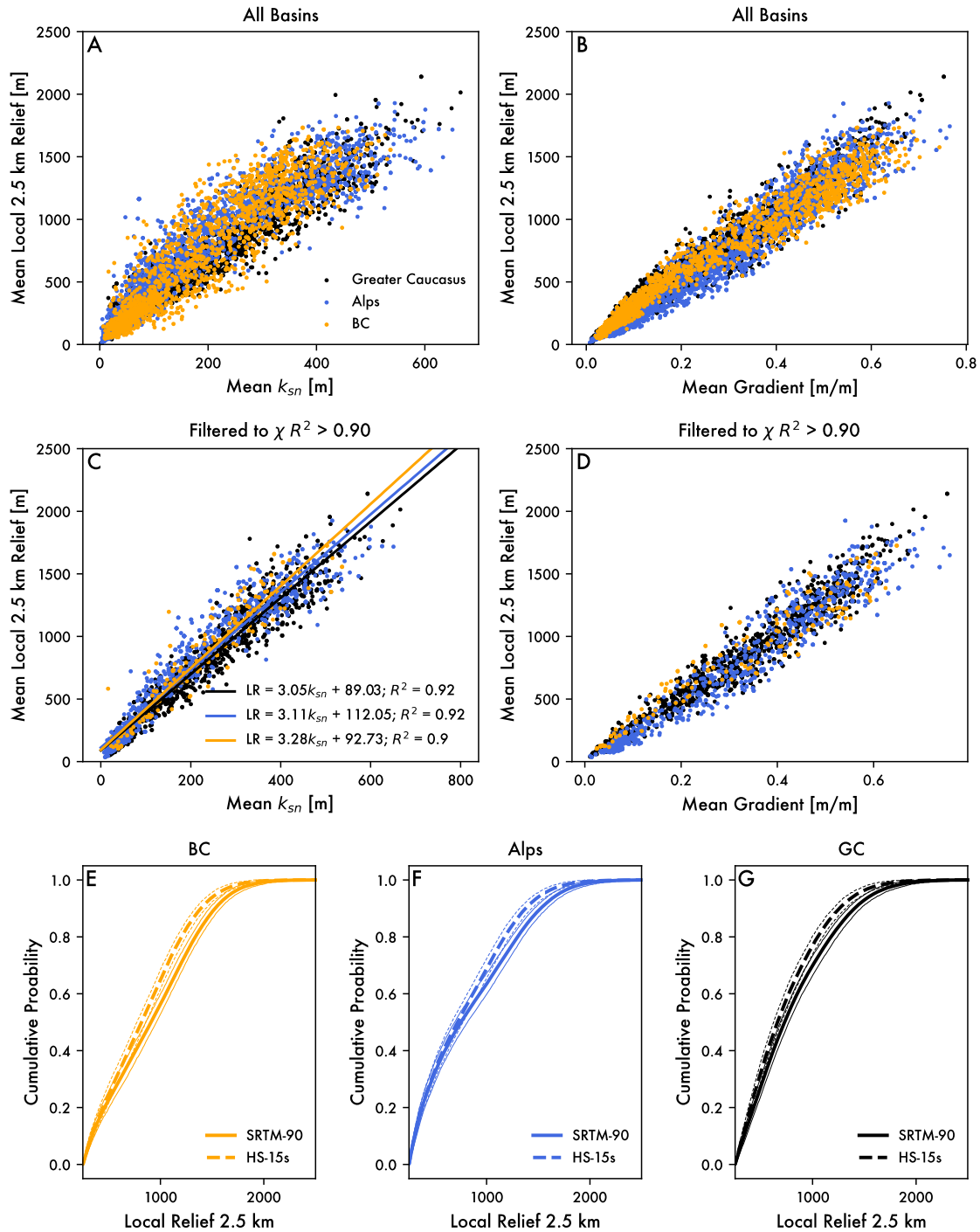


**Figure S1.** A) Mean basin  $k_{sn}$  compared to mean local 2500 m relief for randomly selected basins for the three example locations. B) Mean hillslope gradient compared to mean local 2500m relief for the same basins. C) Filtered mean basin  $k_{sn}$  compared to mean local 2500 m relief, using a cutoff of 0.9 for the  $R^2$  of the  $\chi$ -elevation relationship as a proxy for basins without major knickpoints. Also shown are linear fits between  $k_{sn}$  and relief which are used in the models. D) Same as B but for the filtered basins shown in C. E) Cumulative probability distributions for BC, F) Alps, and G) GC regions, comparing SRTM-90 and HS-15s datasets.

E) Comparison of the cumulative probability of 2500 m local relief calculated from the Hydrosheds 15 arcsecond DEM and 2500 m local relief from SRTM 90 for the British Columbia region. F) Same as E but for the Alps region. G) Same as E but for the Greater Caucasus.

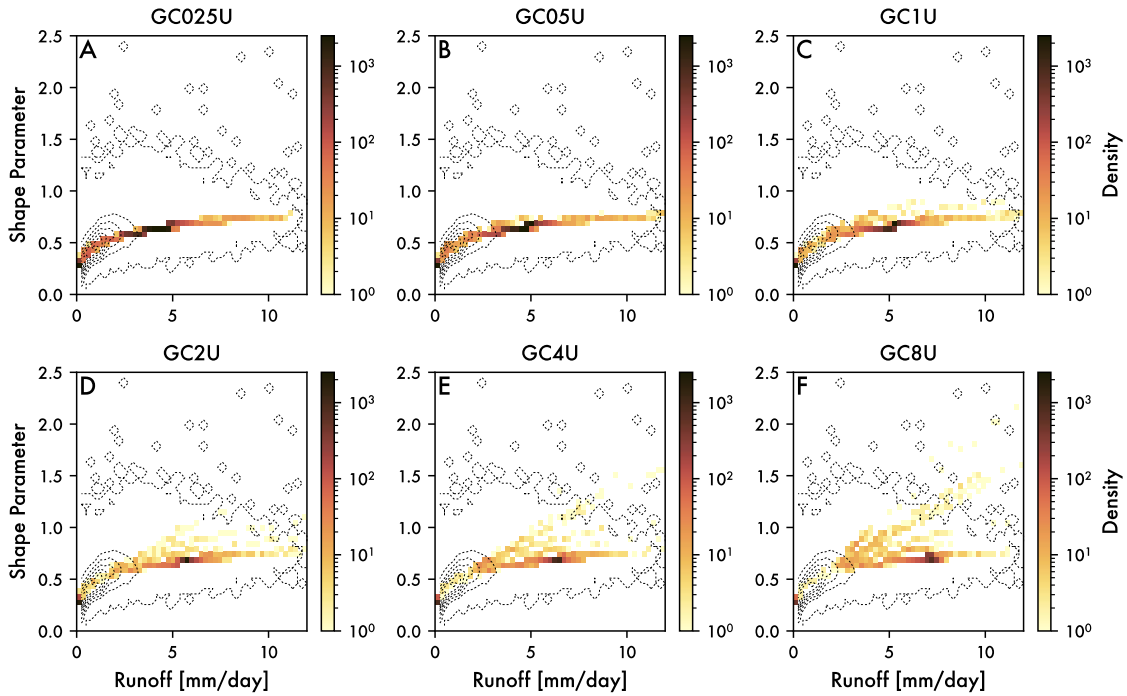


**Figure S2.** 2D density plots of individual pairs of runoff and variability within all bins across all timesteps between model initiation and achievement of steady state for the base Greater Caucasus unlinked runs. Generally, the majority of the time in the models are spent in portions of parameter space well represented in the WaterGAP3 data (e.g., Figure 2A), which are shown with the contours.

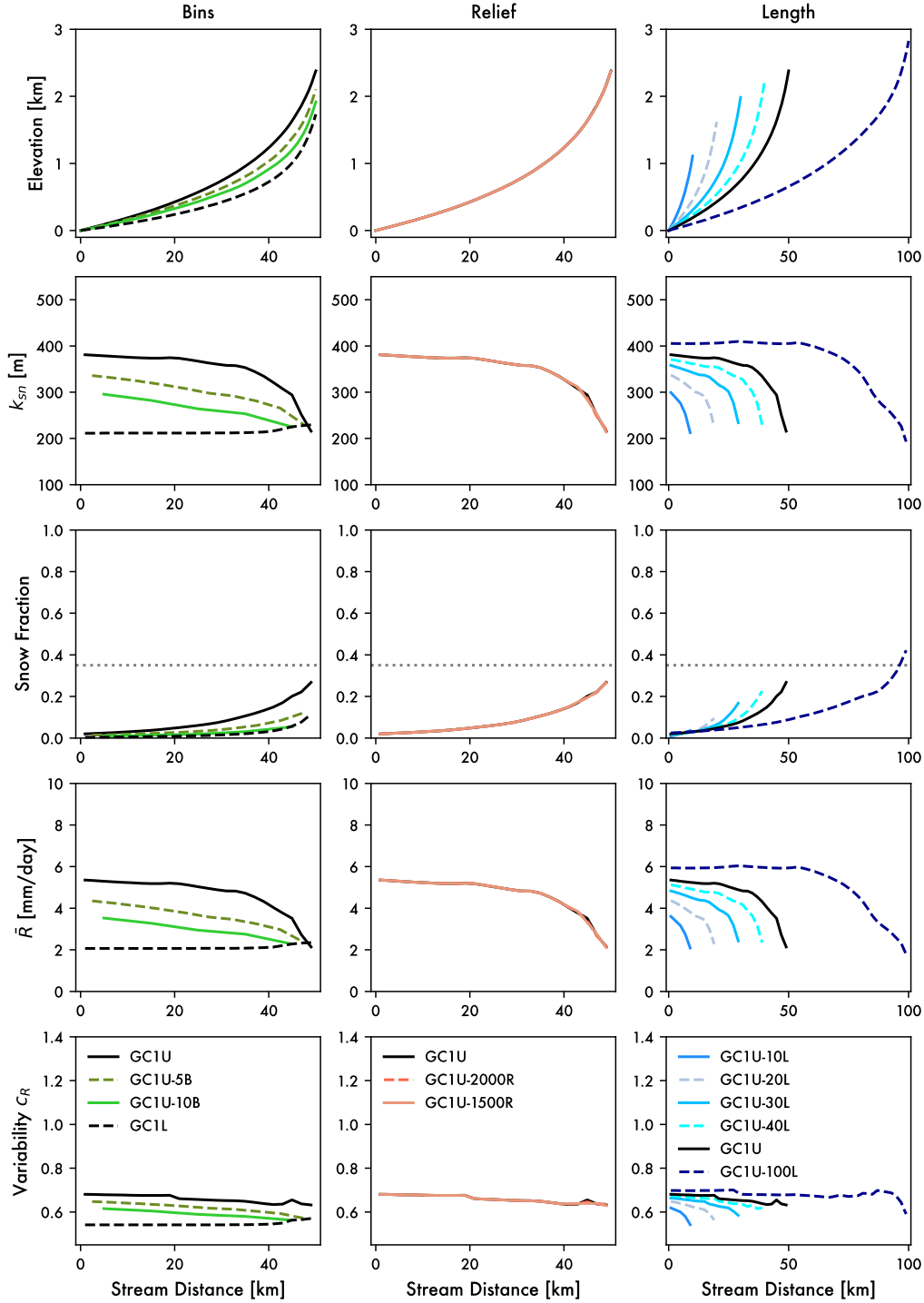


**Figure S3.** Comparison of evolution of model GC1U to the sensitivity test runs discussed in the main text. Setup of figure is identical to that of main text Figure 4. The right column considers similar models with different size runoff bins, specifically 5000 m (GC1U-5B) and 10000 m (GC1U-10B). Model GC1L is also included for reference. The center column considers models with different imposed maximum local relief, specifically 1500 m (GC1U-1500R) and 2000 m (GC1U-2000R). The right column considers models

with different stream lengths, specifically 10 km (GC1U-10L), 20 km (GC1U-20L), 30 km (GC1U-30L), 40 km (GC1U-40L), and 100 km (GC1U-100L).

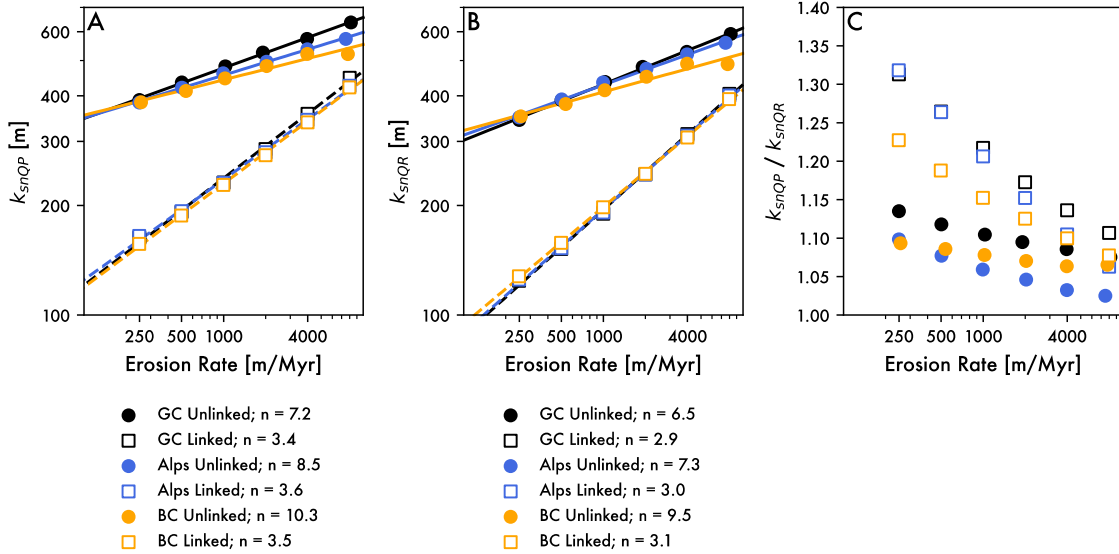


**Figure S4.** Comparison of predictions of different versions of  $k_{sNQR}$ . A) B) Relationship between erosion rate and mean  $k_{sNQR}$  along with power law fits.  $k_{sNQR}$  is calculating  $k_{sNQR}$  sensu Adams et al. (2020) but using runoff as opposed to precipitation. B) Relationship between erosion rate and mean  $k_{sNQP}$  along with power law fits.  $k_{sNQP}$  is calculating  $k_{sNQP}$  identical to Adams et al. (2020). For this, runoff is converted to precipitation using the local linear relation between runoff and precipitation from the WaterGap3 data for each area and then this precipitation value is routed along the profile as if it was runoff. This is what is displayed in Figure 8B. C) Ratio of  $k_{sNQP}$  to  $k_{sNQR}$  as a function of erosion rate.

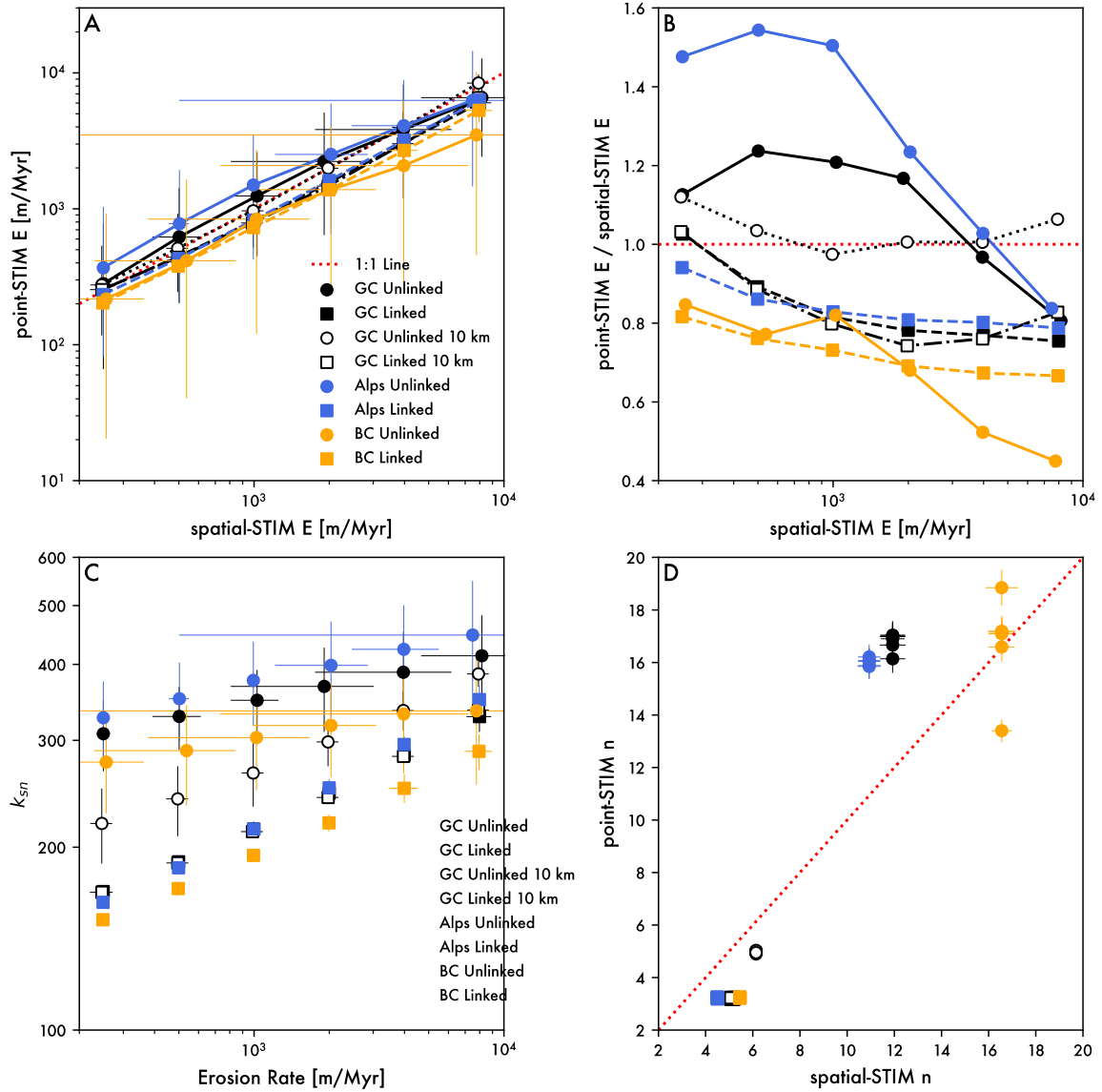


**Figure S5.** Comparison of predictions of spatialSTIM and a point based version of STIM from Lague et al., (2005) modified to use a Weibull distribution of runoff. A) Mean erosion rate of the main models as determined from spatialSTIM vs the prediction from STIM using the mean  $k_{sn}$ , mean daily runoff, and estimated variability for the steady-state of individual spatialSTIM runs. A 1:1 line is plotted for reference. B) Mean erosion rate of the main models as determined from spatialSTIM vs a ratio of the spatialSTIM erosion rate to the predicted STIM erosion rate from A. This panel appears as Figure 11A in the main text. C)  $k_{sn}$ -erosion rates for the spatialSTIM models (circles and squares) compared to predicted  $k_{sn}$ -erosion rate relationships for comparable STIM models (lines). Note because generally each model for a given hydroclimatic ruleset (e.g., GC vs Alps vs BC), linked vs unlinked, and uplift rate produces a different mean runoff and  $c_R$ , there are a suite of predicted  $k_{sn}$ -erosion rate relationships for a given family of models. E.g., GC unlinked models produce 6 different  $k_{sn}$ -erosion rate relationships, one for each of the 6

uplift rates tested. D) Approximation of the power law exponent (i.e.,  $n$  in the stream power equation) from fitting the spatialSTIM relationships compared to fitting each  $k_{sn}$ -erosion rate relationship in C as predicted by STIM. This panel appears as Figure 11B in the main text.

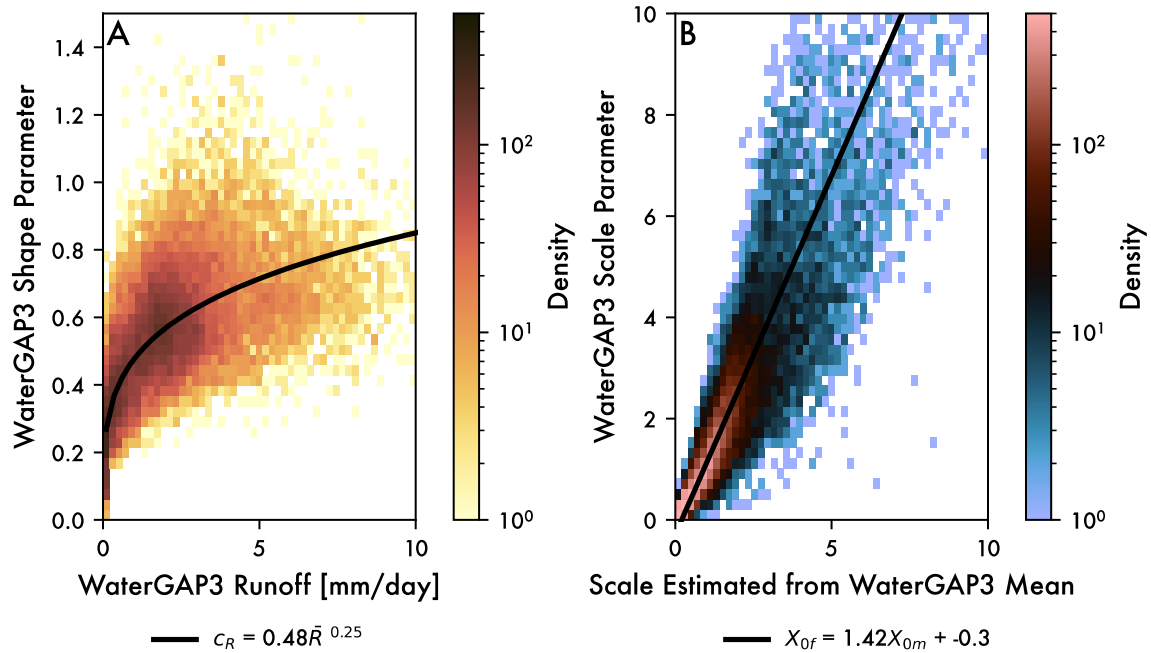


**Figure S6.** Singular relationships between A) mean runoff and shape parameter and B) scale parameter estimate from the mean runoff and the fit scale parameter for rain dominated WaterGAP3 pixels (i.e., where snowmelt fraction < 0.35). These relationships are used to parametrize the Rain Only models that are presented in main text Figure 11.

<b>Parameter</b>	<b>Value</b>	<b>Units</b>
$k_o$	$1e-11$	$m^{2.5}s^2ka^{-1.5}$
$\tau_r$	45	Pa
$k_w$	15	$m^{-0.5}s^{0.5}$
$k_t$	1000	$m^{-7/3}s^{-4/3}ka$
$\omega_n$	0.5	Dimensionless
$\omega_k$	0.25	Dimensionless
$a$	3/2	Dimensionless
$\alpha$	2/3	Dimensionless

$\beta$	2/3	Dimensionless
$dx$	100	m
$dt$	1	days

**Table S1.** STIM and other model parameters fixed for all runs. STIM parameters are similar to those used by Forte et al., (2022) for the Greater Caucasus.

**See included Excel sheet for Table S2.**

**Table S2.** Model runs and key parameters or properties that are varied between individual model runs. Columns are Model Name (how the model is referred to in the main text), Site (either GC, Alps, or BC), Length (length of the modeled river profile in km), Bin Size (size of individual bins in km, if this is empty, it implies that bin size was a constant area as opposed to a constant length), Bin Size (size of individual bins in km<sup>2</sup>, if this is empty, it implies that bin size was a constant length as opposed to a constant area), Bin Relation (either linked or unlinked), Uplift Rate (imposed uplift rate in mm/yr), Maximum Relief (the imposed maximum relief that the model is allowed to reach in m), Base Level (the base level in meters to which the profile is fixed), Snowmelt (indicating whether snowmelt was included or excluded as it was for the rain only models), and Figures (a list of main text figures and supplemental figures in which results from that model appears).

### References

Adams, B. A., Whipple, K. X., Forte, A. M., Heimsath, A. M., & Hodges, K. V. (2020). Climate controls on erosion in tectonically active landscapes. *Science Advances*, 6(42).

<https://doi.org/10.1126/sciadv.aaz3166>

Forte, A. M., Leonard, J. S., Rossi, M. W., Whipple, K. X., Heimsath, A. M., Sukhishvili, L., et al. (2022). Low variability runoff inhibits coupling of climate, tectonics, and topography in the Greater Caucasus. *Earth and Planetary Science Letters*, 584.

<https://doi.org/10.1016/j.epsl.2022.117525>

Lague, D., Hovius, N., & Davy, P. (2005). Discharge, discharge variability, and the bedrock channel profile. *Journal of Geophysical Research*, 110, F04006–F04006.  
<https://doi.org/10.1029/2004JF000259>